

2011

Molecular Dynamics Simulation of Gold Nanoparticles and Surface Stress Effect

Siming Zhang
Lehigh University

Follow this and additional works at: <http://preserve.lehigh.edu/etd>

Recommended Citation

Zhang, Siming, "Molecular Dynamics Simulation of Gold Nanoparticles and Surface Stress Effect" (2011). *Theses and Dissertations*. Paper 1257.

This Thesis is brought to you for free and open access by Lehigh Preserve. It has been accepted for inclusion in Theses and Dissertations by an authorized administrator of Lehigh Preserve. For more information, please contact preserve@lehigh.edu.

**Molecular Dynamics Simulation of Gold Nanoparticles and
Surface Stress Effect**

by

Siming Zhang

A Thesis

Presented to the Graduate and Research Committee

of Lehigh University

In Candidacy for the Degree of

Master of Science

in

Computational and Engineering Mechanics

Lehigh University

September 2011

Copyright © 2011 Siming Zhang

All Rights Reserved

This thesis is accepted and approved in partial fulfillment of the requirement for the Master of Science.

Date

Dr. Edmund B. Webb
Thesis Advisor

Dr. Gary Harlow
Department Chair

Acknowledgements

This accomplishment of this thesis would not have been possible to achieve without the help of some persons, which I would like to thank here.

First of all, I wish to thank my parents for your unfailing support. They have never ceased to encourage me during the whole time when I study in US. I would not be passionate to make my goal come true without their love and patience.

Furthermore, I'm deeply grateful to Professor Webb for giving me this opportunity to work and study in his wonderful group. His contagious enthusiasm has been an inspiration for me. I am also indebted to him for teaching me the knowledge of Molecular Dynamics and how to use LAMMPS.

Finally, I wish to express my appreciation to my colleagues in the research group for their help and support, including Baiou Shi, Haifeng Zheng, and Yibo Wang. I will never forget the fantastic experience of working together with them.

Table of Contents

Acknowledgements.....	iv
Table of Contents	v
List of Table	vii
List of Figures	viii
Abstract.....	1
Chapter 1. Introduction	3
1.1 Nanoparticles.....	3
1.2 Gold Nanoparticles.....	6
1.2.1 Brief Overview of Metallic Nanoparticles.....	6
1.2.2 Gold Nanoparticle.....	8
1.2.3 Brief overview of Structure of Gold Nanoparticle	9
1.3 Production of Gold Nanoparticle	11
1.4 Studies of Gold Nanoparticles.....	14
1.4.1 Experimental studies	14
1.4.2 Numerical Studies	16
1.5 Surface Stress	19
1.6 Motivation of the study	21
Chapter 2 Numerical Methods	24
2.1 Fundamentals of Molecular Dynamics	24
2.2 The MD Algorithm.....	32
2.2.1 Verlet's Algorithm and Velocity Verlet's Algorithm	32

2.2.2 Periodic Boundary Conditions.....	35
2.3 Embedded Atom Method.....	36
2.4 Simulation Procedure.....	38
Chapter 3 Results and Discussion.....	43
3.1 General Analyses	43
3.2 The Effect of Surface Stress and Pair Distribution Function Analysis	56
3.2.1 Surface Stress Calculation	57
3.2.2 Pair Distribution Function $G(r)$ Analyses of Gold Nanoparticles.....	62
3.2.3 Surface Effect Discussion	65
Chapter 4 Summary, Conclusion and Future Work	71
4.1 Summary and Conclusion	71
4.2 Future Work	74
Appendix A.....	76
Reference	105
Vita.....	108

List of Table

Table 3.1 Surface Stress Normal Components Calculation through the whole bulk	59
--	----

List of Figures

Figure 1.1 Calculated fraction of molecules at the surface as a function of nanoparticle size for particles of various shapes. [1] (Without permission)...	5
Figure 1.2 Rayleigh light-scattering of gold (Au) and silver (Ag) nanoparticles displaying various colors depending on the material, shape, and size. [7](Without permission).....	7
Figure 1.3 Illustration of Surface Plasmon Resonance	7
Figure 1.4 Face-centered-cubic (fcc) clusters: (a) octahedron; (b) truncated octahedron; (c) cuboctahedron. [4] (Without permission).....	10
Figure 1.5 Icosahedral clusters [4] (Without permission).....	10
Figure 1.6 Decahedral clusters: (a) regular decahedra; (b) inotruncated decahedra; (c) Marks truncated decahedra. [4] (Without permission).....	11
Figure 1.7 Electron micrograph of a gold solution reduced with sodium citrate [13] (Without permission)	12
Figure 1.8 Size distribution of Au NPs formed from a standard citrate solution [13] (Without permission, the size of nanoparticle is in Å in x-axis)	13
Figure 2.1 Schematic comparison of time- and length-scales, accessible to different types of simulation techniques (quantum simulations (QM), molecular dynamics (MD), Brownian Dynamics (BD) and hydrodynamics/fluid dynamics (HD))	31
Figure 2.2 2D representation of Periodic boundary conditions	36

Figure 2.3 R=50 Å Au Nanoparticle	40
Figure 2.4 Au Bulk (Periodic Boundary Condition).....	42
Figure 3.1 Pair Distribution Function G(r) of Au Bulk	44
Figure 3.2 Pair Distribution Function of Lennard-Jones liquid [32]	45
Figure 3.3 Radial Density Profile of $R_{NP} = 49.2$ Å Au Nanoparticle	48
Figure 3.4 Pair Distribution Function of $R_{NP} = 49.2$ Å Au Nanoparticle	48
Figure 3.5 Radial Density Profile of $R_{NP} = 19.7$ Å Au Nanoparticle	49
Figure 3.6 Pair Distribution Function of $R_{NP} = 19.7$ Å Au Nanoparticle	49
Figure 3.7 Radial Density Profile of N=600 ($R_{NP} = 13.3$ Å) Au Nanoparticle.....	50
Figure 3.8 Pair Distribution Function of N=600 ($R_{NP} = 13.3$ Å) Au Nanoparticle.....	50
Figure 3.9 Radial Density Profile of $R_{NP} = 11.1$ Å Au Nanoparticle.....	51
Figure 3.10 Pair Distribution Function of $R_{NP} = 11.1$ Å Au Nanoparticle	51
Figure 3.11 Radial Density Profile of $R_{NP} = 9.3$ Å Au Nanoparticle.....	52
Figure 3.12 Pair Distribution Function of $R_{NP} = 9.3$ Å Au Nanoparticle	52
Figure 3.13 Pair Distribution Function of Au bulk within the same range as NPs'	53
Figure 3.14 Surface Stress Configuration of <0 0 1> free-surface gold bulk.....	61
Figure 3.15 Surface Stress Configuration of <1 1 0> free-surface gold bulk.....	61
Figure 3.16 Surface Stress Configuration of <1 1 1> free-surface gold bulk.....	62
Figure 3.17 First Peaks of G(r) of Gold Bulk, $R_{NP}=9.3, 49.2$ Å NPs	63
Figure 3.18 G(r) First Peak Position of Au nanoparticles.....	63
Figure 3.19 Effective Pressure of Au nanoparticles.....	65

Figure 3.20 First Peaks of $G(r)$ of $R_{NP}=19.7$ Au nanoparticles.....	67
Figure 3.21 First Peaks of $G(r)$ of $N=450$ ($R_{NP}= 11.8 \text{ \AA}$) Au nanoparticles	67
Figure 3.22 $G(r)$ First Peak Position Data for Core Atoms and Whole NPs	68
Figure 3.23 Effective Pressure Core Atoms of Au nanoparticles	69
Figure 3.24 Number of Core Atoms versus Total Number of All Atoms in Nanoparticles	70
Figure 3.25 Number of Core Atoms versus Total Number of All Atoms in Nanoparticles ($N<1000$)	70

Abstract

In this thesis, the Molecular Dynamics (MD) method was applied to perform atomic scale simulations of bulk single crystal gold (Au), free planar crystalline surfaces of single crystal Au, and 33 Au nanoparticles (NPs) to investigate whether atomic scale bonding in NPs exhibits lattice compression for sufficiently small NPs. A pre-existing embedded atom method (EAM) potential for Au was used in all our simulations. The atomic scale pair distribution function $G(r)$ was calculated for Au bulk and all NPs simulated to evaluate changes in atomic bonding environment for nanoparticles compared to a bulk crystal.

Planar surface calculations indicate that at equilibrium state, the values of stress of surfaces in different orientations were all in the range of $1.3\sim 2.0 J/m^2$ and surface stress manifested only in those atoms within 7 to 8 Å of the free surface. $G(r)$ analysis on the NPs showed that the position of the first peak in $G(r)$ shifted to smaller r for smaller NPs. This indicated that a compressive stress was acting to compress nearest neighbor bond lengths, but the corresponding estimation of surface stress was nearly four times the values obtained from planar surface calculations.

The definition of core atoms was given based on the calculation result of surface stress contribution, and the entire analysis was applied to the core atoms of each NP. The features of $G(r)$ of core atoms were quite similar to what is computed for all atoms in the NP, but the shift of first peak in $G(r)$ was less when core atoms alone were considered. This indicated that lattice compression, as determined from core

atom analysis, was less. As a result, the surface stress prediction based on core atom lattice compression was very close to values given by the planar free surface simulations. This showed that the surface stress was some linear combination of surface stress values of different low index surfaces.

Chapter 1. Introduction

1.1 Nanoparticles

The development of nanoscience and nanotechnology has been exponentially increasing in the last twenty years. It is safe to claim that it has improved the lives of human-beings in a great amount of ways. For example, carbon nanotubes (CNT) have been widely used in gene delivery and magnetic nanoparticles are functional in targeted drug delivery [1]. R. Singh et al. reported in 2005 that three types of f-CNTs, ammonium-functionalized single-walled and multiwalled carbon nanotubes (SWNT-NH₃⁺; MWNT-NH₃⁺), and lysine-functionalized single-walled carbon nanotubes (SWNT_{Lys}-NH₃⁺) are able to condense DNA to varying degrees, indicating that both nanotube surface area and charge density are critical parameters that determine the interaction and electrostatic complex formation between f-CNTs with DNA [2]. In 2008 B. Chertok explored the possibility of utilizing iron oxide nanoparticles as a drug delivery vehicle for minimally invasive magnetic targeting of brain tumors and proved that accumulation of iron oxide nanoparticles in gliosarcomas can be significantly enhanced by magnetic targeting; thus, these nanoparticles appear to be a promising vehicle for glioma-targeted drug delivery [3]. In summary, nanotechnology involves a broad field of study of the properties of matter on the nanometer length scale, and tries to understand, control, and manipulate it [4].

In the realm of nanotechnology, a significant position is occupied by nanoparticles,

as they are considered the fundamental building blocks of the field. The term ‘nanoparticle’ refers to a particle with size in the range of 1-100 nm [1] [4]. The most significant consequence of this nanoscale is the tremendous surface area per unit volume of the object, implying that many atoms in a nanoparticle reside at or near a free surface. This high surface-area-to-volume ratio can lead to a highly significant influence of the atoms on a particle surface in determining the overall NP’s properties. It can be shown that both fraction of surface atoms and specific surface area increase with decreasing size of particle in Figure 1.1 (the characteristic size of nanoparticle is in nanometer in x-axis, for instance, for spheres, the characteristic size is the radius). Correspondingly, there is also a similar increase in specific surface area with decreasing particle size. Herein, the surface thickness was considered as the thickness of only one atomic layer, which is different from what we define in this thesis.

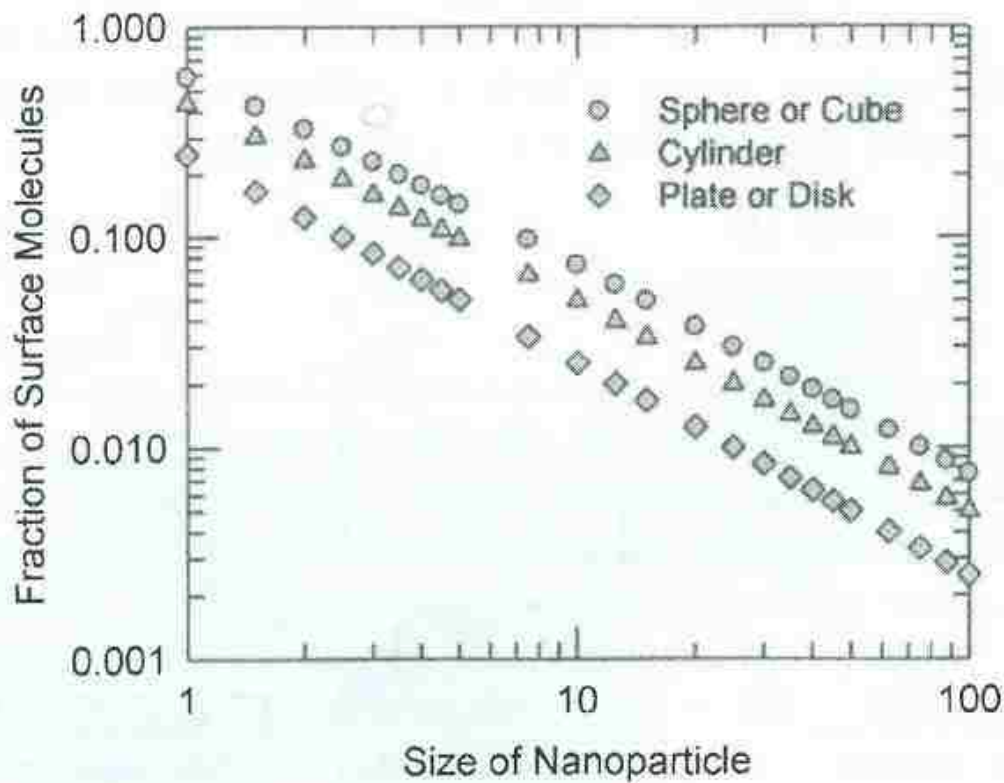


Figure 1.1 Calculated fraction of molecules at the surface as a function of nanoparticle size for particles of various shapes. [1] (Without permission)

The large surface area to volume ratio of nanoparticles can bring about unique properties, e.g. if nanoparticles have dimensions below the wavelength of incident light, quantum effects will be exhibited. As a result, transparency can be attained since specific absorption wavelengths are determined by particle size.[1][5] An overarching theme is that nanoparticles possess dramatically different physical and chemical properties from those of bulk materials and those expected from the simple extrapolation of bulk properties. This explains why scientists and researchers have paid tremendous attention to the field of nanoparticles.

1.2 Gold Nanoparticles

1.2.1 Brief Overview of Metallic Nanoparticles

Metallic nanoparticles have unique optical and electrical properties so they have earned great interest in science [4]. It is believed that these unique properties originate from their finite size. The size of metal nanoparticles is only a few or tens of nanometers by definition, so the movement of their electrons is confined in space and consequently discrete electron energy levels emerge that are dependent on particle size and shape. Thus they show quantum size effects that are predicted by Quantum Mechanics theory. [6] A quantum size effect means particles behave electronically as zero-dimensional quantum dots. As a result, the de Broglie wavelength of the valence electrons is of the same order as the size of the particle itself. The de Broglie wavelength of one particle is inversely proportional to its momentum, which is given by

$$\lambda = \frac{h}{p} \quad (1.1)$$

where h is Planck's constant and p the momentum. In this case, the electron has a very low momentum compared to macroscopic objects. In this case, the de Broglie wavelength may be large enough that the particle's wave-like nature gives observable effects. For instance, free mobile electrons confined to a nanometer scale structure show a characteristic collective oscillation frequency of the plasmon resonance, i.e. the excitation of surface electrons by light, giving rise to the so-called plasmon resonance band (PRB). [5] As shown in Figure 1.2, the color metal nanoparticles display when

scattering visible light depends on their chemistry, size, and shape, which is attributed to a phenomenon known as Surface Plasmon Resonance (SPR).

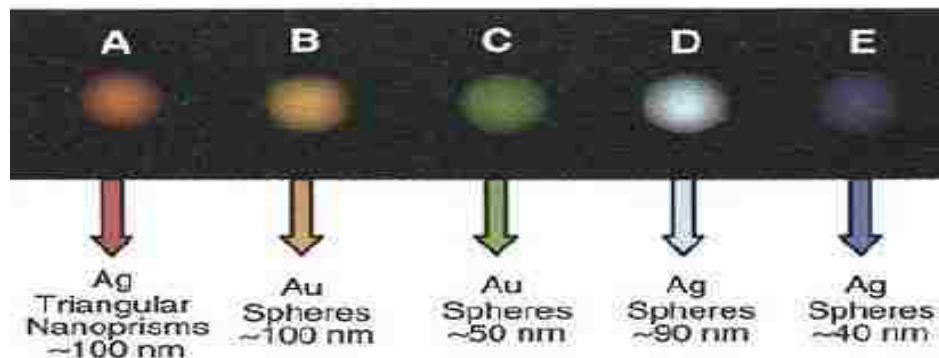


Figure 1.2 Rayleigh light-scattering of gold (Au) and silver (Ag) nanoparticles displaying various colors depending on the material, shape, and size. [7](Without permission)

Surface Plasmon Resonance (SPR) is a phenomenon where electrons on the surface of metal nanoparticles oscillate due to the interaction between light and confined electrons of the nanoparticles, which is illustrated in Figure 1.3.

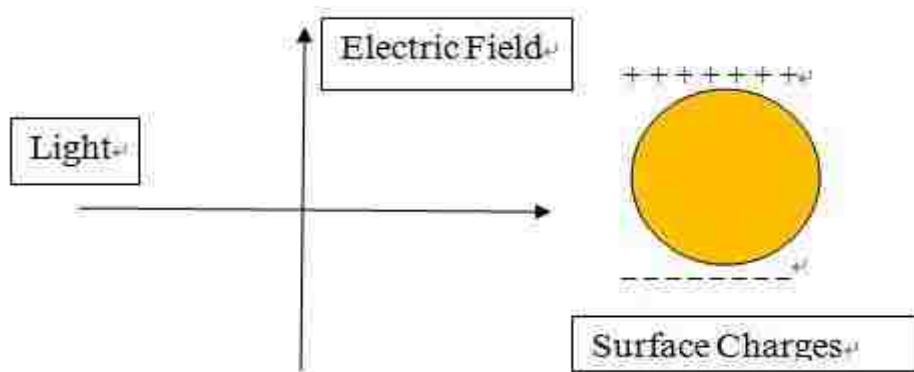


Figure 1.3 Illustration of Surface Plasmon Resonance

When it happens, light of a specific wavelength is absorbed by a metallic nanoparticle, which matches the frequency of the oscillation, and the nanoparticle displays a color. Since the frequency can be determined by the material, size, and shape of nanoparticles, as well as the environment, metal nanoparticles of different properties display different colors. [5] [7] Because molecular adsorption on NPs

changes the PRB, this property has been exploited in biosensor applications, DNA sensing for example. [5] [8]

1.2.2 Gold Nanoparticle

Among nanoparticles, gold nanoparticles (Au NPs) have been extensively studied; this is partly because gold is the subject of one of the most ancient themes of investigation in science. Au NPs are among the most stable metal nanoparticles [5] since Au is relatively chemically inert. They present fascinating aspects such as low-symmetry structures at some geometric magic numbers [9] and size-related electronic, magnetic [5, 7] and optical properties (due to quantum size effect). Moreover, their applications to catalysis, owing to the high surface-to-volume ratio, and biology are also significant. For example, conjugates of Au NPs-oligonucleotides are of great interest owing to the potential use of the programmability of DNA base-pairing to organize nanocrystals in space. This gives multiple ways of providing a signature for the detection of precise DNA sequences to develop biosensors, disease diagnosis, and gene expression, etc [5]. Besides, research is expanding on Au NP catalytic effects associated with CO oxidation, NO reduction, and the water-gas shift reaction, i.e. the chemical reaction in which carbon monoxide reacts with water vapor to form carbon dioxide and hydrogen; new Au NP based catalytic systems are now being explored. [4][5]

Applications exploiting the optical properties of Au NPs utilize functionalization of NPs with chromophores. Chromophore means the part of a molecule responsible

for its color. These have diverse applications due to a range of options for the chromophore. In 2003, K. Thomas *et al.* reported that gold nanoparticles associated with fluorophores were utilized in photocurrent generation and fluorescent display devices [10]. Furthermore, they also showed that gold nanoparticles can bind and release amino acids when linked with appropriate chromophores. All in all, it appears safe to assume that Au NPs will be a key building block for nano-science and -technology in the 21st century.

Given the many applications of Au NPs, as well as the extensive literature on them, this thesis will focus on Au NPs as a canonical metal NP system.

1.2.3 Brief overview of Structure of Gold Nanoparticle

The structure of gold nanoparticles has been perhaps the most investigated aspect about them.[4] It has been found, theoretically and experimentally that gold nanoparticles have crystallographic structures different from the bulk material.[4,11] In general, gold nanoparticles have icosahedral or decahedral motifs depending on their size while bulk gold has face-centered cubic (fcc) crystal structure [4]. These crystallographic structures are shown in Figure 1.4-1.6.

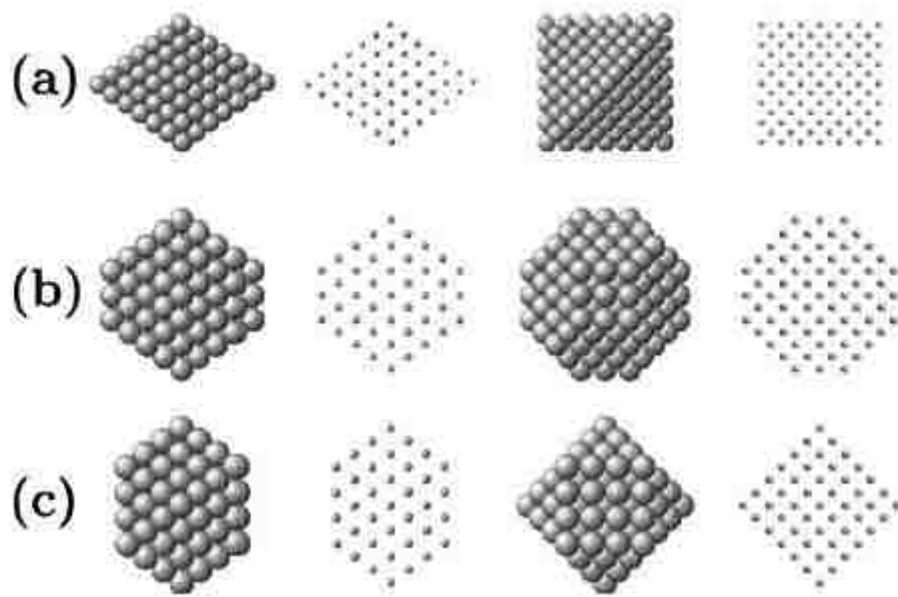


Figure 1.4 Face-centered-cubic (fcc) clusters: (a) octahedron; (b) truncated octahedron; (c) cuboctahedron. [4] (Without permission)

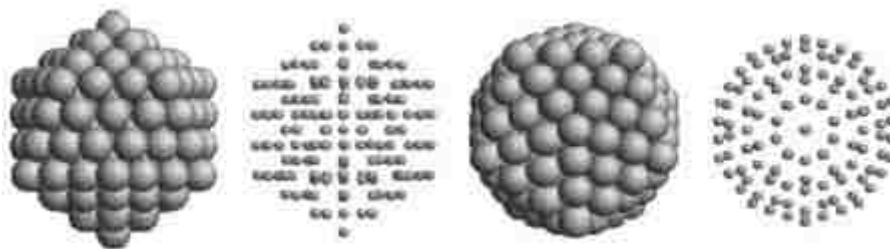


Figure 1.5 Icosahedral clusters [4] (Without permission)

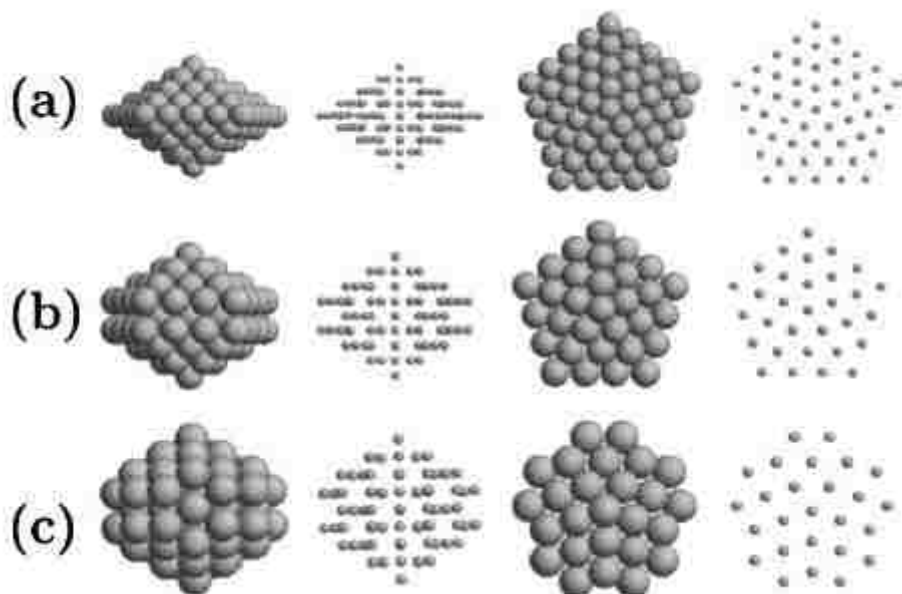


Figure 1.6 Decahedral clusters: (a) regular decahedra; (b) inotruncated decahedra; (c) Marks truncated decahedra. [4] (Without permission)

The most energetically stable structures are shown as quasispherical shapes and obtained by optimizing the surface/volume ratio as well as surface energy. For Au NPs, the icosahedral structure is considered to be the most stable structure for particles smaller than 1 nm and the truncated-decahedral structure is considered to be the optimal one for clusters of size between 1 nm and 2 nm. For Au NPs larger than 2 nm, the truncated-octahedral structure (fcc) is the dominant shape [4, 12]. It should be noted here that the size ranges are not defined very strictly. Furthermore, it is predicted that relatively small difference in energy exists between different morphologies.

1.3 Production of Gold Nanoparticle

There is a long history of the production of Gold nanoparticles. In 1857, M. Faraday reported a method for formation of colloidal gold by electrochemical

reduction of aqueous solution of chloroaurate, $AuCl_4^-$. [1] [5] Nearly one century later, Turkevich introduced a method using citrate reduction in water of tetrachloroauric acid, $HAuCl_4$, to produce spherical gold nanoparticles. In his preparation, 95 ml of chlorauric acid solution, containing 5 mg Au, were heated to the boiling point, and then were added by 5 ml 1% sodium citrate solution with stirring. A faint pink or blue color appeared after a minute and then darkened quickly for around 5 minutes, ending up with deep wine red. Colloidal particles are highly reproducible and form spherical shapes (Figure 1.7) with a mean diameter of about $200 \pm 15 \text{ \AA}$ and a root-mean-square deviation of 12.5% (Figure 1.8). [13] This method has been the most popular among conventional methods of Au NP synthesis by reduction of gold derivatives [5]; it is considered relatively simple and it results in a relatively monodisperse distribution of particle sizes [1]. A further effort by Frens in 1973 introduced greater control over average particle size by varying the trisodium citrate-to-gold ratio [1, 5].

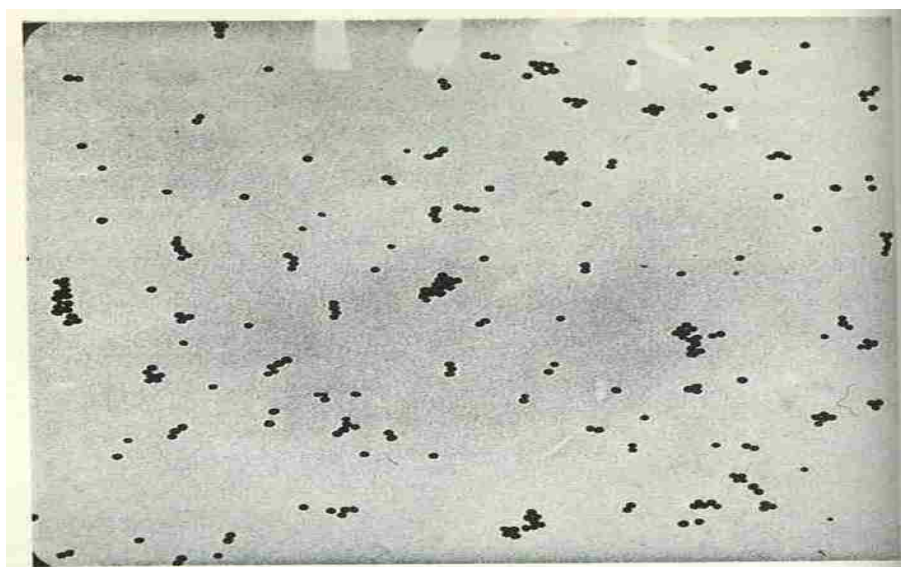


Figure 1.7 Electron micrograph of a gold solution reduced with sodium citrate [13]
(Without permission)

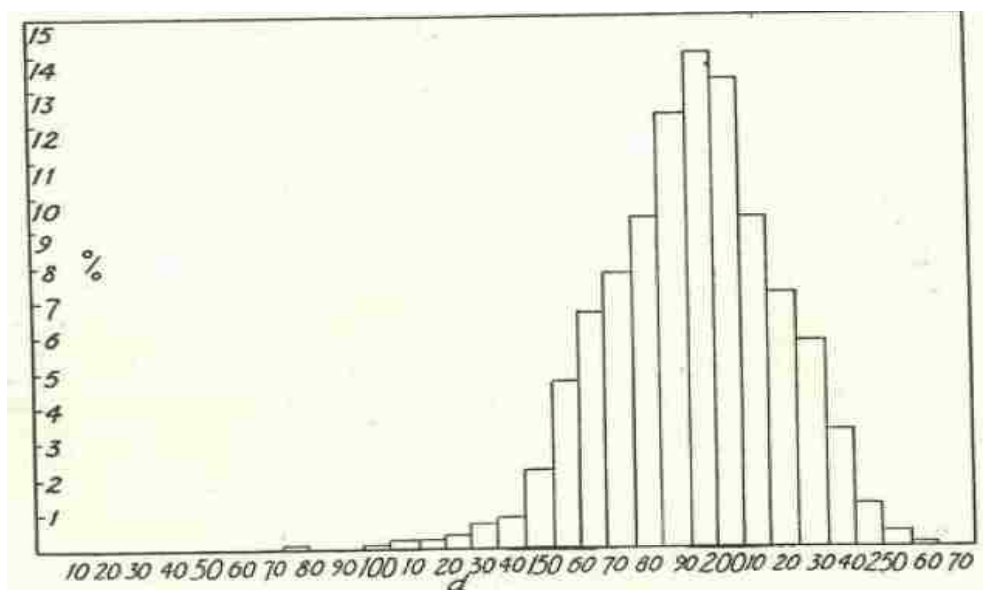


Figure 1.8 Size distribution of Au NPs formed from a standard citrate solution [13]
(Without permission, the size of nanoparticle is in Å in x-axis)

In recent decades, numerous applications of gold nanoparticle have led to the development of other approaches for making gold nanoparticles. For instance, the Brust-Schiffrin method for Au NP synthesis introduced in 1994 had considerable impact on the overall field; it offered, for the first time, the facile synthesis of thermally stable and air-stable Au NPs with reduced size dispersity and controlled average size (ranging in diameter between 1.5 and 5.2 nm) [5]. There are also other more recent approaches which have been developed. The utilization of microemulsions, copolymer micelles, reversed micelles, surfactants, and membranes has advanced two-phase systems for Au NP synthesis; these methods provide control over the growth and stabilization of the Au NPs. The procedure of seeding growth has also been improved in recent studies. Given that advance, it is possible to choose an average diameter of Au NP in the range of 5-40 nm, and control the size distribution to within 10-15% of that range. This step-by-step technique (i.e. graft to some matrix first, e.g. copolymer micelles, then Au NP extracted from metal salt) which has been

used for nearly a century is more effective than one-step method (i.e. Au NP extracted from metal salt directly) as far as avoiding secondary nucleation. [5] Despite the existence of a large number of Au NP synthesis methods, most methods depend on *in situ* reduction of gold (III) salt or acid via chemical means [1].

1.4 Studies of Gold Nanoparticles

1.4.1 Experimental studies

In general, Au NPs have been studied in two main ways, experimentally and numerically. Via Au ion implantation experiments and both ion and electron irradiation, H. G. Silva-Pereyra et al. (2010) report that elongation occurs in Au NPs; the elongation depends on a Au NP's diameter, and it only brings about geometrical change, without any interchange of material among Au NPs. This result supported the thermal spike model developed by D'Orléans et al. in 2003 which could explain the deformation of NPs. Most important, the structure of both as-prepared and Si-irradiated Au NPs show high stability and fcc bulk structure, which means that there is no lattice stress from what the authors concluded. This can be extensively helpful for the analysis and understanding of the nonlinear optical properties of nanocomposite according to the authors. [14] H. Yao et al (2007) has experimentally produced Au NPs at an air/solution interface under highly acidic conditions and protected by N-acetylglutathione (NAG). By applying Field Emission Scanning Electron Microscopy observation, it was found that Au NPs' superlattices exhibit fivefold symmetric structure, such as decahedron and icosahedrons. These are

probably developed by twinning, and their formation is dominated by the kinetics of growth. This may develop some new interesting phenomena in fivefold twinned structure of Au NP in nanoscience.[15] In 2010 N.P. Young et al. investigated structural transformations of Au NPs using variable temperature high-resolution transmission electron microscopy. They demonstrated that the decahedron structure is stable at room temperature, and a decahedral to icosahedral transition was confirmed as a route to lower energy at low temperature. Meanwhile, a co-existence of solid/liquid phase at high temperature just below melt point is observed. These results are important in a more precise understanding of the structure and action of catalytic gold nanoparticles and in the experimental verification of theoretical calculations. [16] X.N. Xie et al. (2009) have also looked into electronic behavior of passivated Au NP experimentally. They investigated the electric characteristics of the slow ionization and relaxation in ionizable alkanethiol molecules by applying experimental method and using two alkanthio, 11-mercaptoundecanoic acid (MUA,SH – (CH₂)₁₀ – COOH) and 11-mercaptoundecanol (MUO,SH – (CH₂)₁₀ – CH₂ – OH). The electric behavior of MUA-passivated Au NPs was considered to be dominated by the ionic motion. By this approach they observed the formation of hysteresis loops in *IV* curves. These results represent a novel charge conduction mechanism governed by ligands in the NP/molecule binary system and may find new applications in molecular electronics and NP-based memory and sensor devices. [17] The structure of Au nanoparticles supported on silica was analyzed using structural models fit to X-ray powder diffraction(XRD) and X-ray adsorption spectroscopy data (A. Longo et al., 2008). It is

found that gold nanoclusters supported on silica exhibit significant twin stacking faults; from this, the authors concluded that, in nanocrystalline gold, faulted compact packing of atomic layers constitutes a possible atomic arrangement. By comparison, good XRD fitting was obtained by linear combination of lognormal size-distributed f.c.c. cuboctahedral, decahedral and icosahedral contributions. Furthermore, the complementary analysis of X-ray absorption data did not confirm the presence of a noteworthy fraction of noncrystalline particles. [18]

1.4.2 Numerical Studies

Researchers studying the properties of Au NPs have also utilized numerical methods. M. McGuigan et al. (2009) applied density functional theory to computationally simulate gold nanoclusters and to describe the energy landscape in terms of the size and shape of a Au NP for well known structures such as icosahedrons, and cuboctahedrons. By tabulating the bond length and binding energy and introducing a shape parameter θ to find intermediate shapes between cuboctahedron and icosahedron, it is demonstrated that the potential energy can be calculated as a function of bond length and shape. As examples, it is illustrated that the cuboctahedral shape was lower energy than the icosahedral shape for 13 atoms and the opposite was the case for 55 and 147 atoms. At the end, the effect of the presence of Au NP on the binding energy of O_2 is computed as well showing that it leads to weaker binding which may have implications for the use of nanogold for

catalysis. [19] A.S. Barnard et al (2005) used computational calculations to check a proposed multiscale thermodynamic model based on the Gibbs free energy of an arbitrary nanoparticle as a function of size and shape. This showed that the equilibrium shape of Au NP is truncated octahedron as it optimizes the surface energy/stress and surface-to-volume ratio. Meanwhile, it is also indicated that temperature rather than size should be a decisive factor on Au NP's morphology. Since temperature is such a decisive factor, the author even concluded that it is appropriate to make a feedback loop including the temperature in the optimization. Their work also pointed out that melting is preceded by a shape transition from a truncated octahedron into a more cuboctahedral-like NP. [20]

Molecular Dynamics (MD) is an extremely suitable method to investigate the properties of NPs since its accessible time and length scales coincide with those of NP size and dynamics. MD refers to a computer simulation method to study atomic physical movements. D.-H. Seo et al. (2009) has reported that by applying MD simulation, there are two crucial factors for the diffusion behavior of Carbon Nanotube (CNT)-support Au and Pt nanoclusters: the interface, i.e. the geometry of the bottom layer of nanocluster, and the matching between diffusion pathway and the lattice of the bottom layer. As a result, Au nanoclusters diffuse in the translational direction (i.e. along a CNT's axis) and conversely Pt NPs revolve around the CNT axis and moves along the circumferential direction. Moreover, the chirality and curvature of CNT controls the diffusion pathway and diffusion rate, respectively by controlling the distribution of the low-energy pathways. A strategy such as vacancy

formation or CNT doping is proposed in order to prevent undesirable aggregation of CNT-supported clusters and improve their durability. [21] G. Grochola (2007) used MD growth simulations in conjunction with thermodynamic integration to calculate and compare the relative free energy for different structures of Au NPs. Thermodynamic integration is the process of transforming between Au EAM potential to Einstein solid. The utilization of this integration is able to compute the difference of free energy between some reference state, where the Gibbs free energy can be rigorously defined, and the state of interest. The difference is usually integrated in a designed thermodynamic cycle along some relevant paths. The internal and free energy of ideal/pristine NPs and surface disordered ones were analyzed and compared. It was concluded that the dominance of icosahedral shape growth kinetics is attributed to firstly a preference for closed, ideal hexagonal-like surfaces, secondly a thermodynamic preference for this morphology, and lastly the kinetic effect where nanoparticles grown in kinetic growth environment are constrained to surface disorder. [22]

Monte Carlo (MC) simulation is another powerful approach to investigate nanoparticles. This method can be used to calculate equilibrium results from repeated random sampling among appropriate configurations within the thermodynamic ensemble of interest. K. P. McKenna et al (2007) used the MC method to simulate thermodynamic equilibrium of Au nanocrystallites (NCs) at room temperature. Both free and MgO(100)-supported Au NCs, whose atom on the surface can diffuse and may transiently occupy low-coordinated positions on the surface, are calculated by

introducing an on-lattice model. The result demonstrates that the atoms on both unsupported and supported NCs will occupy different positions on NC surface than those predicted by a zero temperature static model. Transient configurations of surfaces at finite temperature can be very important since they may influence the optical, electronic, and chemical properties of NCs [23].

1.5 Surface Stress

Because NPs in general - and Au NPs specifically - possess significant surface area to volume ratio, their surface thermodynamic properties can be very important in determining a NP's properties. An important surface thermodynamic quantity is the surface stress. Surface stress, f , is a thermodynamic quantity that describes the amount of energy or reversible work per unit area required to elastically deform a solid surface. It differs from another fundamental thermodynamic parameter, i.e. surface free energy γ , which represents the energy needed to form a new surface by a process like cleavage.[24] In liquid, these two values are identical, as the configuration of fluid surface remains constant owing to bulk atoms or molecules moving exteriorly to the surface when a fluid surface is stretched. Put differently, a liquid cannot support a shear stress so the only way to create/eliminate new surface is by adding/removing atoms from the surface, rather than elastically deforming existing atoms at the surface. In contrast, when a solid surface is put in tension (within an elastic limit), the total number of surface atoms is conserved; therefore, the number of atoms per unit area changes and consequently, $f \neq \gamma$.

The mathematical definition of surface stress, or the relationship between surface stress and surface free energy, is shown as following [24]. In order to create new area dA , the needed amount of reversible work dw can be expressed as:

$$dw = \gamma dA \quad (1.2)$$

The total work performed to create a planar surface A , in other words, the total excess free energy of that surface should be γA . When a solid surface is stretched, the elastic deformation can be written in terms of a surface strain tensor, ε_{ij} , where $i, j=1,2$. Now consider a reversible perturbation that causes a small variation in the area through an infinitesimal elastic strain $d\varepsilon_{ij}$. The surface stress tensor f_{ij} can be defined as the work associated with the variation in γA . Thus, the variation of total excess free energy of the whole surface caused by the strain $d\varepsilon_{ij}$ is equal to

$$d(\gamma A) = A f_{ij} d\varepsilon_{ij} \quad (1.3)$$

where $i, j = 1, 2$ are dummy indices by the definition of tensor analysis.

Since

$$d(\gamma A) = \gamma dA + A d\gamma, \quad dA = A \delta_{ij} d\varepsilon_{ij} \quad (1.4)$$

where δ_{ij} is the Kronecker delta, the surface stress tensor f_{ij} can be expressed as

$$f_{ij} = \gamma \delta_{ij} + \frac{\partial \gamma}{\partial \varepsilon_{ij}} \quad (1.5)$$

For a general surface, the surface stress tensor can be referred to a set of principal axes so that all off-diagonal components are zeros. In the case of a threefold or higher rotational axis symmetry, the diagonal components are the same, so the surface stress can be written as a “scalar”:

$$f = \gamma + \frac{\partial \gamma}{\partial \varepsilon} \quad (1.6)$$

1.6 Motivation of the study

When a solid object of finite size is elastically deformed, work is performed against both volume and surface forces. [5, 24] For macroscopic solid mechanics situations, it is no doubt that the volume term is the dominant one over the surface term. However, for a small enough solid, the surface term may become dominant and induce a bulk stress of order f/t , where f is surface stress and t is the characteristic length, say the diameter of a nanoparticle. Recall, for instance, a liquid where $f = \gamma$. It can be shown that the pressure difference between the fluid inside and outside a liquid drop or bubble is $\Delta p = \frac{2\gamma}{R}$, where R is the radius of the drop. An analogous-but less straight forward-situation exists for solid particles. It is expected that this surface induced bulk stress will consequently change the lattice spacing. [24] As mentioned before, gold nanopartilces possess an extremely large surface area-to-volume ratio, so it is fair to assume that the effect of surface stress would be significant.

On the other hand, most research on gold nanoparticles by applying MD simulation focused on the influence of structures on thermodynamic properties, such as structure stability. Examples include keeping fcc bulk morphology under irradiation [14] and being stable at room temperature as decahedron [16]. Structure transformation has also been investigated. For instance, the sequence of high stability morphologies with increasing number of atoms is modified from (decahedral - icosahedral - Marks-decahedral - truncated octahedral) in vacuum to (octahedral - Marks-decahedral - truncated octahedral) under gas pressure [25]. However, there have been fewer works that focus on the role of surface stress in determining peculiar

properties of gold nanoparticle, such as internal strain and pressure, atom number density, and bond lengths different from equilibrium bulk values. Thus, the effect of surface stress on the internal pressure and bonding environment for gold nanoparticles is the focus of the current study. The impact of surface stress is essential for many physical phenomena.

For example, inhomogeneous surface stresses can give rise to a self-organization of mesoscopic structures on surfaces.[26] For submonolayer coverage of Pb on Cu surfaces, R. Plass et al pointed out that elastic interactions due to a surface-stress difference between different surface structures contribute to the stabilization of domain patterns.[27] W. Lu et al (2002) reported that anisotropy of surface stress plays an important role in surface reconstruction, and is responsible for the domain patterns on reconstructed silicon (100) surface. [28]For applications, the thermodynamics of surface stress has been utilized to develop theorems on thin films and nucleation during solidification.[29] The effect of surface stress on nanoparticles continues to fascinate the attention of researchers in science and engineering. [26]

Since Au NPs display a fairly important role among all metal nanoparticles in nanoscience, this project will study the effect of surface stress on the internal pressure, lattice constant, atom number density and specific bonding environments of atoms for Au NPs in the size range $D = 1$ to 5 nm. Specifically, this work will show the size dependence of the effect of surface stress to better elucidate factors contributing to observed behaviors. The method utilized throughout the study is classical molecular dynamics (MD) simulation. The code utilized (LAMMPS) is publicly available,

massively parallel, and open source. The interaction between simulated Au atoms is a semi-empirical potential energy function that accurately describes the surface properties of Au. Home grown (Matlab) codes were applied to analyze the data from MD simulations. More details of the computational procedure will be presented in a following section.

In Chapter 2, background knowledge of Molecular Dynamics will be introduced; in addition, specific procedures of MD simulations and data analysis used herein are presented. In Chapter 3, the results of data analysis are provided, along with discussion of results. The conclusion and interpretation of the current work is presented in Chapter 4, along with an outline of future potential work.

Chapter 2 Numerical Methods

2.1 Fundamentals of Molecular Dynamics

Computer simulation methods have been applied to solve many-body problems in physics, physical chemistry and biophysics; these methods are essentially experiments in statistical mechanics. [30] The systems which statistical mechanics addresses are composed of a large (i.e. statistical) number of particles; this branch of science allows one to relate the collective properties of interesting atoms and molecules to the macroscopic bulk (i.e. thermodynamic) properties of materials. In many cases, it is impossible to study specific aspects of how atomic interactions manifest continuum properties unless via computer simulation. Among simulation techniques, it is natural to classify them according to the length scale at which the model is resolved. For atomic scale models, there are two main families of simulation technique, Molecular Dynamics (MD) method and Monte Carlo (MC) method [31, 32].

Molecular Dynamics simulation is a computational tool used to describe how positions, velocities, and orientations of interacting particles change over time. Particles may represent atoms, groups of atoms, or even larger entities; herein, focus is on the use of MD as an atomic scale simulation technique. A set of models (i.e. mathematic functions) that describe atomic scale interaction are foundations of any MD simulation. Dynamics are governed by the system's Hamiltonian, and Hamilton's equations of motion

$$H=T+U, \dot{p}_i = -\frac{\partial H}{\partial q_i}, \dot{q}_i = -\frac{\partial H}{\partial p_i} \quad (2.1)$$

where H is the Hamiltonian, T is the kinetic energy which is a function of momenta, $T = \frac{p^2}{2m}$, and U is the potential energy which is a function of position in the atomic ensemble, $U=U(q)$. The simulation model for atomic interactions is defined by an interatomic potential energy function, or potential for brevity. [33] The potential can be represented as $U = U(\vec{r}^N)$, where \vec{r}^N is the set of location vectors of an ensemble of N atoms. For simplicity, in many simulations only pair interactions among atoms are taken into account, so the potential energy of a system of N atoms is

$$U = \frac{1}{2} \{ \sum_{i=1}^N \sum_{i \neq j} u(r_{ij}) \} \quad (2.2)$$

where $u(r_{ij})$ is a pair potential function having a known form, and r_{ij} is the absolute value of distance between atom i and j . Since the interatomic forces are derived from potential, they are all conservative, and can be related to the potential as the gradient of U , or

$$\vec{F}_i = - \frac{\partial U}{\partial \vec{r}_i} \quad (2.3)$$

In Molecular Dynamics, positions of atoms are attained by seeking the solution of Newton's equation of motion:

$$\vec{F}_i = m \vec{r}_i''(t) \quad (2.4)$$

where \vec{F}_i is the force induced by the interactions between atom i and the other $N-1$ atoms, and the double dots mean second order time derivative while m is the mass of each atom. Substitution of (2.3) into (2.4) relates the force to the potential function, which is a known input to a given MD simulation. Integration once yields the momenta of atoms, and the atomic position can be found by integrating an additional time.

Repeating the integration procedure many times will reveal the trajectories of atoms, based on which time average of some desired thermodynamic value, $\langle A \rangle$, can be computed

$$\langle A \rangle = \lim_{t \rightarrow \infty} \frac{1}{t} \int_{t_0}^{t_0+t} A(\tau) d\tau \quad (2.5)$$

When a state of equilibrium is reached, the average will be independent from the initial time t_0 . Because there are many times of integration involved to achieve equilibrium, it is of great importance that an appropriate integration scheme and a time steps to the algorithm are selected. Poor integration schemes or too large a time step will introduce systematic errors in the thermodynamic ensemble and therefore in the computed value of $\langle A \rangle$.

MD simulation can be used to realize different sorts of thermodynamic ensembles, which dictate the state thermodynamic quantities that will remain constant throughout the simulation. Once the ensemble is established, time averages may be obtained, say, for the thermodynamic state variables that are not held constant. For example, a commonly employed MD ensemble is the microcanonical, [30] where number of atoms N , volume V , and total energy E (sum of kinetic and potential energy) are held constant (i.e. NVE ensemble); in such an ensemble, one may seek, for instance, time averages of the system pressure P or temperature T . Other often employed ensembles include the canonical, i.e. constant-NVT, ensemble, and the isothermal/isobaric, i.e. constant-NPT, ensemble. In order to implement a given ensemble in a MD simulation, certain thermodynamic quantities must be held constant (either absolutely or in a time averaged sense). Various numerical algorithms have been formulated to fix the

corresponding properties to a desired value. More theoretically detailed information on ensembles can be found in [32] [33] and texts of statistical mechanics. The key point is that properly implemented MD algorithms maintain thermodynamic ensembles, from which methods of statistical mechanics reveal desired thermodynamic quantities (i.e. material properties).

In short, the mechanism of the MD simulation process can be summarized as following

1. Select the potential energy function that will be used to describe the interatomic interactions
2. Set the initial position and velocity of each atom in a system and the dimensions of the simulation space
3. Calculate all the forces on total N atoms via the governing interaction model
4. Find accelerations of each atom
5. Obtain each atom's velocity and position after a given timestep through numerical integration by a chosen algorithm
6. Update all atomic positions
7. Repeat steps 3 - 6
8. Post process, or analyze, generated thermodynamic and atomic trajectory data

MD simulation was first introduced by B. Alder and T. Wainright in 1957 to study the phase transition of hard spheres system, where particle propagation is determined by each successive binary collision, rather than an integration of the equations of motion. In 1964 a model system of liquid Argon was simulated by A. Rahman. In this

simulation not only the collision events between two particles but also interactions modeled by Lennard-Jones potential were taken into account. This was the first time that MD simulation was applied to atoms interacting through a continuous potential. During 1970s, MD method continued to mature. Rahman and Stillinger (1971) performed a simulation of 216 water molecules using an effective pair potential and Ewald summation to calculate long-ranged forces triggered by electrostatic (i.e. Coulomb) interactions. Several years later, the first protein simulation was carried out by McCammon for bovine pancreatic tyrosin inhibitor. [33] After that, MD simulations began to be operated under different conditions and ensembles and became more sophisticated. For instance, using MD to study non equilibrium processes was first advanced in 1983 by Gillan and Dixon to calculate the autocorrelation function of the microscopic heat current and hence the thermal conductivity of a liquid. The Nose-Hoover thermostat algorithm, which is used to obtain isothermal ensembles, was developed in 1984. The Car-Parrinello method to carry out ab initio quantum mechanical MD (in which quantum mechanical effects for the electronic degrees of freedom are taken into account) was developed in 1985. The progress of available computer facilities is a major factor driving the development of MD simulations. [31,32] Today MD methods are applied to a huge class of subjects, e.g. surface properties, molecular clusters, biomolecules, and properties of liquids and solids, and many different simulation codes have been developed.

Another well-developed simulation methodology is Monte Carlo (MC) method. MC simulation is a computer simulation method that explores the phase space of a

system in a time-independent and stochastic manner. It uses a sequence of random numbers to render and sample the phase space, from which diverse physical properties of the system can be extracted. The main advantage of Monte Carlo simulation over many analytical techniques is that it is a simple and straightforward method that can provide an approximate solution to the problems encountered in complex systems. Specifically, MC is able to reveal long time equilibrium properties.

The main advantage of MD method, with respect to MC method, is that MD probes equilibrium configurations as well as dynamical properties of the system; this makes MD well suited to compute time correlation functions and associated transport coefficients. MD is therefore more efficient to evaluate some thermodynamic properties like heat capacity, compressibility, and interfacial transport properties. There are also computational advantages of MD method, particularly as compared to ab initio methods. For example, the dynamic behavior of the atomic system is described empirically without having to solve Schrodinger's equation at each time step. Furthermore, it has been extensively discussed that many MD models are inherently able to be executed in parallel. On the other hand, parallel implementations of MC or ab initio based MD are highly non-trivial to realize. In this thesis, we use the open source code LAMMPS, which can be run in massively parallel environments and provide efficient simulation on metal atomic scale systems. [35]

Computing every force on each atom is a demanding part of a MD simulation. In order to limit the number of force calculations, the smallest possible system – in terms of number of atoms – should be simulated. The minimum system size necessary to

compute a given desired property is not always obvious and a common practice is to analyze how increasing system size influences obtained results. A number of algorithmic approaches exist that help minimize system size such as applying periodic boundary conditions; these will be discussed in greater detail in the following section. In addition to how large a system must be, one must determine how long a simulation must be run to obtain reliable answers (i.e. with sufficient accuracy and precision). Related to this is that the MD simulation time step should be small compared to the period associated with the highest frequency atomic event. A typical time step for MD simulations of metals is of order 1 fs (i.e. 1 E-15 s); this is roughly 1/1000 of the period for an atomic oscillation. The very small time step is the main drawback of MD method compared to other commonly used numerical simulations. Processes with time scale of order microseconds and larger are outside the reasonable realm for even highly parallel, efficient MD codes. Conversely, MC techniques cannot probe dynamics but they can probe long time equilibrium properties.

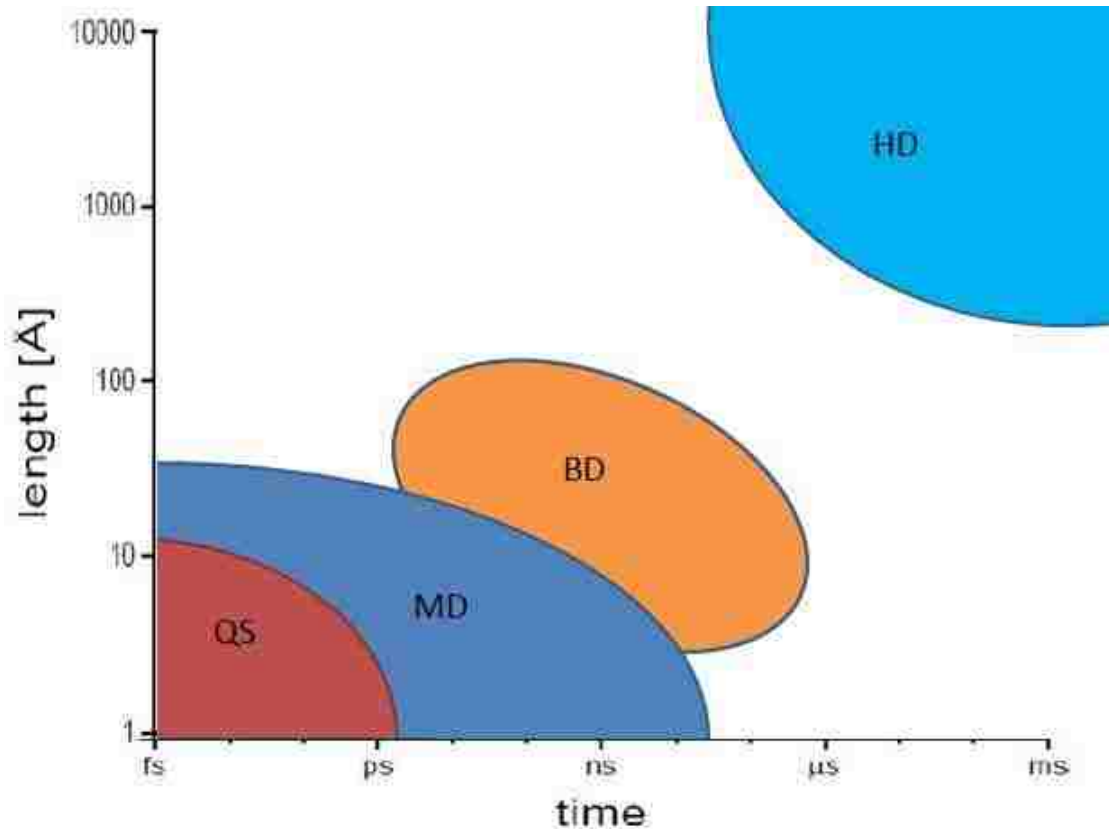


Figure 2.1 Schematic comparison of time- and length-scales, accessible to different types of simulation techniques (quantum simulations (QM), molecular dynamics (MD), Brownian Dynamics (BD) and hydrodynamics/fluid dynamics (HD))

Accessible length- and time- scales of microscopic simulation should be considered. Figure 2.1 shows a schematic representation for different types of simulations in a length-time-diagram. It is clear that the more detailed a simulation technique addresses, the smaller is the accessibility of times and length scales. Hence, quantum simulations (QS), where fast motion of electrons are considered, are located in the lower left corner of the diagram and typical length time scales are of order of Å (Å) and ps. MD method puts fixed partial charges on interaction sites or adds a dynamics model for polarization effects to simulate electronic distribution. [31] Hence, the time scale of the system is determined by the time of collision between atoms and atomic vibration frequencies. Consequently, the accessible time scale is of

order ns and corresponding accessible length scale becomes of order 10-10000 Å. Note Figure 2.1 was originally presented in 2002; accessible length scales for MD have increased dramatically. Brownian Dynamics (BD) can be applied to deal with particles in a solvent medium, where one is not interested in a detailed description of the solvent. In BD the effect of the solvent is hidden in average quantities. If one is not interested in a molecular picture but in macroscopic quantities, the concepts of hydrodynamics (HD) may be applied, where the system properties are hidden in effective numbers, like density and sound velocity. These example methods, or levels of theory, are geared towards liquids but analogous examples exist for solids.

2.2 The MD Algorithm

2.2.1 Verlet's Algorithm and Velocity Verlet's Algorithm

The governing equations of motions are all ordinary differential equations and a standard method for the solutions is the finite difference method. Of a large number of finite-difference approaches devised, the most commonly used one is the Runge-Kutta (RK) method. [33,34] The beauty of the RK method is that the order of a finite difference method can often be increased by using positions and velocities from several points in time instead of only the current time. However, if a fourth-order RK method is applied to MD simulation, four interatomic force evaluations per atom would be required per step, which will make the simulation too slow. Thus, reduction of order is desired; especially, the time expense of calculating intermolecular force

more than once per atom per step should be also avoided. However, the algorithm must be stable.

The most widely used method of integrating the equations of motions in molecular dynamics is Verlet's method or algorithm. It uses positions and velocities from previously evaluated steps to provide a direct solution of equation (2.4). In this study, the simulation code LAMMPS is used and its default algorithm is the velocity Verlet. [35] Hence, the basic idea of Verlet's algorithm, and specifically the velocity Verlet, will be presented here. Information on other integration schemes can be found in texts on atomic scale simulation. [32]

This standard, or basic, Verlet algorithm is a combination of two Taylor's expansions as following. The Taylor series for position from time t forward to $t + \Delta t$ is

$$x(t + \Delta t) = x(t) + \frac{dx(t)}{dt} \Delta t + \frac{1}{2} \frac{d^2x(t)}{dt^2} \Delta t^2 + \frac{1}{3!} \frac{d^3x(t)}{dt^3} \Delta t^3 + O(\Delta t^4) \quad (2.6)$$

And the series from t backward to $t - \Delta t$ is

$$x(t - \Delta t) = x(t) - \frac{dx(t)}{dt} \Delta t + \frac{1}{2} \frac{d^2x(t)}{dt^2} \Delta t^2 - \frac{1}{3!} \frac{d^3x(t)}{dt^3} \Delta t^3 + O(\Delta t^4) \quad (2.7)$$

Adding equations (2.6) and (2.7) with some simplifying produces

$$x(t + \Delta t) = 2x(t) - x(t - \Delta t) + \frac{d^2x(t)}{dt^2} \Delta t^2 + O(\Delta t^4) \quad (2.8)$$

This provides Verlet's algorithm for positions. The truncation error of the algorithm when evolving the system by Δt is of the order of Δt^4 . The acceleration needed in equation (2.8) is obtained from the intermolecular forces and Newton's second law. Velocities are not explicitly solved in equation (2.8), and they are calculated from first-order central difference

$$v(t) = \frac{x(t+\Delta t) - x(t-\Delta t)}{2\Delta t} \quad (2.9)$$

The error associated to this expression is of order Δt^2 rather than Δt^4 . This is a two-step method for it estimates position on next step $x(t + \Delta t)$ from current position $x(t)$ and previous position $x(t - \Delta t)$. Verlet's algorithm offers important features of exact time reversibility, good simplicity and stability for moderately large time steps.

A more commonly used, related algorithm is the velocity Verlet algorithm. The approach is similar with the standard one but starts with position and velocity expansions explicitly

$$x(t + \Delta t) = x(t) + v(t)\Delta t + \frac{1}{2}a(t)\Delta t^2 + \dots \quad (2.10)$$

$$v(t + \Delta t) = v(t) + \frac{1}{2}\Delta t(a(t) + a(t + \Delta t)) + \dots \quad (2.11)$$

The implement scheme of this algorithm is following:

1. Calculate velocities at mid-step,

$$v\left(t + \frac{\Delta t}{2}\right) = v(t) + \frac{1}{2}a(t)\Delta t \quad (2.12)$$

Calculate the positions at next step $t + \Delta t$

$$x(t + \Delta t) = x(t) + v\left(t + \frac{\Delta t}{2}\right)\Delta t + \frac{1}{2}a(t)\Delta t^2 + \dots \quad (2.13)$$

which is the same value as equation (2.10).

2. Calculate the accelerations at $t + \Delta t$, $a(t + \Delta t)$ from the interaction potential using $x(t + \Delta t)$.
3. Calculate the velocities at $t + \Delta t$

$$v(t + \Delta t) = v\left(t + \frac{\Delta t}{2}\right) + \frac{1}{2}a(t + \Delta t)\Delta t \quad (2.14)$$

The advantage of this algorithm compared to the standard one is that we never

need to simultaneously store the values at two different times for any of these quantities. The velocity Verlet algorithm gives good feature of time reversibility, simplicity and stability for even larger time steps compared to standard algorithm.

2.2.2 Periodic Boundary Conditions

In order to avoid large time consumption, the simulation must use small samples. For small sample size, surface effects are definitely nontrivial on the measured properties. For example, in a cube, if there are 1000 atoms in the system, almost half of those will be at outer faces of the cube; even if the number increases up to 10^6 , which is a fairly large number for MD simulation; the percentage of surface atoms is still around 6% in total. Thus, periodic boundary conditions should be applied to avoid surface effects. As shown in Figure 2.2, the cubic box is conceptually duplicated throughout space to model an infinite system. During the simulation, the periodic image of each atom moves in exactly the same way when each atom moves in the central box, i.e. original box. Hence, if one atom leaves its box, one of its images will move into the box through the opposite “face”. With this methodology, the topology of the system is correctly represented while the simulation can use small samples.

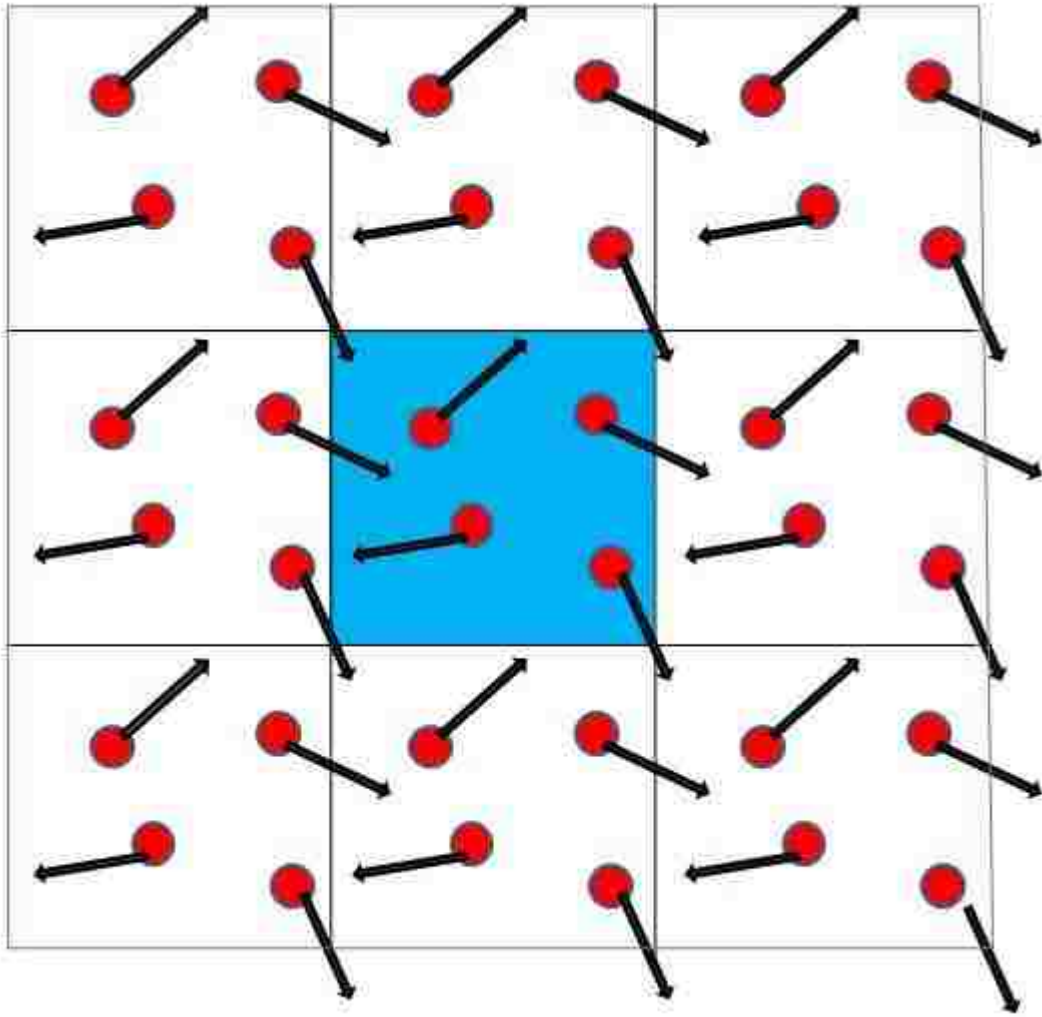


Figure 2.2 2D representation of Periodic boundary conditions

2.3 Embedded Atom Method

It is safe to claim that the hub of a MD simulation is the potential energy function, which describes the interactions between the atoms or molecules of the system; everything obtained from the study depends on the potential energy function. Therefore, the choice of an accurate potential energy function is crucial in computational MD studies. In this study, the embedded atom method (EAM) is chosen.

EAM is a semi-empirical many-body potential describing the energy of a collection atoms; it was first advanced by M. Daw in 1983 to model metallic and inter-metallic interactions. The word “semi-empirical” refers to that this method can be derived from electronic density functional theory, a more exact theory in which electronic charge density is considered as the basic variable to describe the properties of a quantum many-body system. In the scheme of the Embedded Atom Method (EAM), the total energy of a metallic system is described as a sum of pair repulsions along with the energy needed to embed the system into the electron “sea”, or density, caused by surrounding atoms. The first term is used to model repulsion and the second term models binding in a metal system. In this thesis we apply this method, rather than strictly empirical potentials, because the latter fails to describe metals properly. [36]

In a simulation, the EAM potential of atom i is written as:

$$E_i = F_\beta(\sum_{j \neq i} \rho_\alpha(r_{ij})) + \frac{1}{2} \sum_{j \neq i} \Phi_{\alpha\beta}(r_{ij}) \quad (2.15)$$

where r_{ij} is the distance between atoms i and j , $\Phi_{\alpha\beta}$ is a pair-wise potential function, ρ_α is the contribution to the electron charge density from atom j of type α at the location of atom i , and F is an embedding function that represents the energy required to place atom i of type β into the electron charge density. In principle, α and β can be the same or different; for single element models, they are obviously the same.

In studies herein, we used the EAM potential for gold (Au) created by XW Zhou et al. which has been shown to describe accurately basic material properties such as lattice constants, elastic constants, bulk moduli, vacancy formation energies, and

sublimation energies. [37] The potential was used in all our simulations with the help of multiprocessor software LAMMPS created by Plimpton [35].

2.4 Simulation Procedure

Although LAMMPS represents a properly implemented MD simulation tool, it is still necessary to construct one's desired system in a simulation space so that it can be run. Herein, the procedure for carrying out Au NP simulations is presented; sample input decks to LAMMPS for each step of the simulation have been made available as supplementary information to the thesis.

The first step in these simulations was to create an equilibrium bulk Au sample from which Au NPs could be extracted. To accomplish this, a FCC (face centered cubic) gold crystal with the [1 0 0], [0 1 0] and [0 0 1] crystallographic directions along the x -, y - and z -axes, respectively was created first using lattice generation tools in LAMMPS. The $T = 0$ lattice constant is known for the EAM model of Au used here and it agrees with predictions from *ab initio* level theory and experiment (indeed, the zero T lattice parameter was one of the properties to which the interatomic potential was fit). However, the lattice constant at room temperature, i.e. $T=300\text{K}$, was not known so it was found by running a series of 100 ps simulations in an isobaric/isothermal (NPT) ensemble. To mimic an infinite bulk Au sample, periodic boundary conditions were employed in all three directions. By computing running averages of the system volume V , it was possible to determine when the system reached equilibrium. The lattice parameter so determined was further checked in an

additional 100 ps run in an NVT ensemble; because the time average pressure P in this simulation was very close to zero, it was concluded the lattice parameter was a truly equilibrium value.

Then spherical gold nanoparticles were created out of the equilibrated bulk Au sample. The center of mass of the bulk system was determined and NPs were extracted in one of two ways. For some NPs, all atoms within a specified radial distance of the center of mass were kept and, from these atomic coordinates, a new starting condition for a simulation was created. For other NPs, a pre-set number of atoms X was chosen; the X atoms closest to the bulk system center of mass were then retained to create the starting state for a Au_X NP. Each NP so created was first run at $T=300\text{K}$ for 100ps. Technically, the simulations were run in NVT ensemble; however, this is misleading because each NP was surrounded by empty space and was contained in a simulation space with effectively no periodic boundary conditions. In other words, the simulations are isothermal but NP volume relaxation is unconstrained. To study the effect of particle size on the internal pressure, the particles have varying radii $R_{\text{NP}} = 10 - 50 \text{ \AA}$ (i.e. $R_{\text{NP}} = 1 - 5 \text{ nm}$); equivalently, the range of NP size examined was Au_X with $X = 300 - 1800$.

After the initial runs at $T = 300 \text{ K}$, each Au NP was heated to $T = 500 \text{ K}$; this was accomplished by creating a new distribution of atomic velocities corresponding to $T = 500 \text{ K}$ as the starting state for a simulation. Then, each NP was run for 20 ns in an isothermal ensemble. Following this, each NP was cooled to $T=300\text{K}$ over the duration of a 2 ns simulation (LAMMPS has capability to apply a thermostat

algorithm with varying T throughout the simulation). After cooling to $T = 300$ K, all data for analysis were gathered during a subsequent isothermal $T = 300$ K simulation for 100 ps. For all simulations, velocity distributions specified at the start of the simulation were selected to ensure that both linear and angular momenta of each particle were initially set to zero. The figure below is the simulated gold nanoparticle whose formation cut-off radius is 50 \AA .

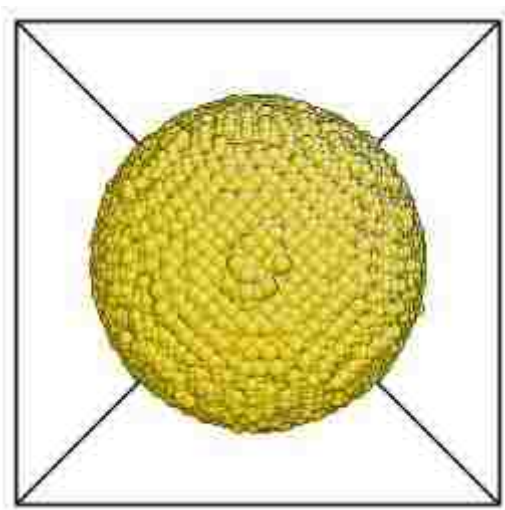


Figure 2.3 $R=50 \text{ \AA}$ Au Nanoparticle

One of the goals of this study was to determine the role of surface stress in generating lattice contraction of Au NPs. To support this, it was first necessary to compute the planar surface stress for this model of Au and for the relevant low index crystal surfaces. To do this, we created another two bulk FCC gold crystals with the $[-1 \ 1 \ 0]$, $[0 \ 0 \ 1]$, $[1 \ 1 \ 0]$, and $[1 \ 0 \ -1]$, $[-1 \ 2 \ -1]$, $[1 \ 1 \ 1]$ orientations along the x -, y - and z -axes, respectively. Along with our first bulk system (from which NPs were extracted), this provided three systems with different crystal orientations along z : $[001]$, $[110]$, and $[111]$. The two new systems were initially constructed using the $T = 300$ K lattice constant previously determined and then thermally equilibrated in NVT

ensemble at $T=300$ K for 100 ps. It was next necessary to form free planar surface systems from the three bulk Au systems. To do this, a MATLAB code (in Supplementary File, i.e. Appendix B) was utilized to find the density profile along the z direction for all three bulks. Since periodic boundary conditions were applied to these systems, one layer of atoms in each system is split across the periodic bound in z . This means that, in the generated density profile, the upper and bottom layers of atoms in z only contain about half the number of atoms that are in all other layers. Using the density profile generated by the code, we shifted atoms through the periodic bound in z to effectively move the upper “half-layer” down to the bottom (i.e. we subtracted from the z coordinates of the atoms on that upper plane the length of simulation box in z -direction). From this point forward, periodic boundary conditions were removed in z in order to create free surfaces in the z -direction for each of the $[0\ 0\ 1]$, $[1\ 1\ 0]$, $[1\ 1\ 1]$ (now surface) systems. Note for each system, this creates two free surfaces in z : one each at the top and bottom of the lattice.

To permit isothermal surface relaxation, the new planar surface models were submitted to NVT simulations at $T = 300$ K for 200 ps. Following this, surface stress data were obtained in an additional 100 ps isothermal simulation (again, because free surfaces exist in z , this is not strictly NVT). The total number of atoms in the three planar surface Au models are $N = 62500$ for the $\langle 0\ 0\ 1 \rangle$ surface system, $N = 64800$ for $\langle 1\ 1\ 0 \rangle$, and $N = 60480$ for $\langle 1\ 1\ 1 \rangle$. Figure 3.2 is an example of gold crystal with a $\langle 1\ 1\ 0 \rangle$ free surface in z .

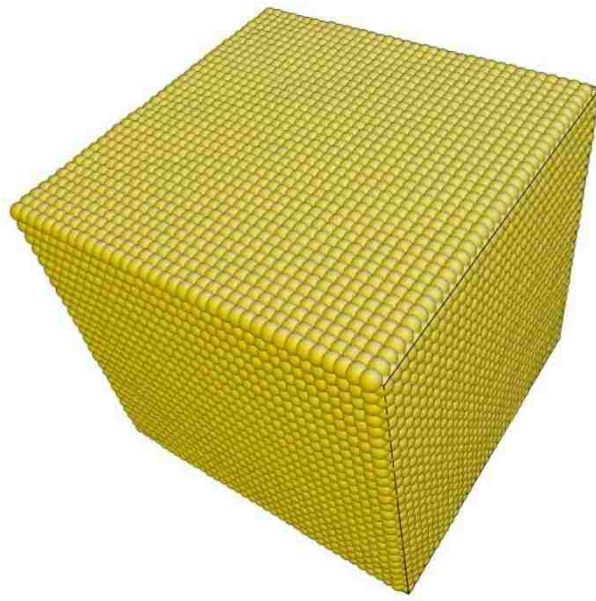


Figure 2.4 Au Bulk (Periodic Boundary Condition)

Chapter 3 Results and Discussion

3.1 General Analyses

In order to demonstrate the structural features of simulated Au nanoparticles (NP), the pair distribution functions (PDF), $G(r)$, are calculated. The function provides the probability of finding a pair of atoms apart from each other at a distance r , relative to the probability expected for a completely random distribution at the same density. The pair distribution function of atomic pair distance r is given by

$$G(r) = 4\pi r(\rho(r) - \rho_0) \quad (3.1)$$

where $\rho(r) = \frac{1}{4\pi r^2 N dr} \sum_{i=1}^N \sum_{j \neq i} \delta(r - r_{ij})$ is the density at distance r , ρ_0 the average number density, N the number of atoms in system and $\delta(x)$ the Dirac delta function, dr is the thickness of volume sphere shell. Note in numerical simulations, the data of atoms' radial position with respect to the center of mass are calculated into histograms which represent sphere shells of identical thickness, dr , i.e. the data are discretized. Hence, to obtain the density, the summation of delta functions should be normalized by the sphere shell volume, $4\pi r^2 \cdot dr$, rather than sphere shell area only, $4\pi r^2$. This is why the thickness dr is introduced. Since gold is fcc crystal, there are four atoms in one lattice unit cell; from the MD simulations, the lattice constant at $T=300\text{K}$ is found as 4.101 \AA . These lead to the value of ρ_0

$$\rho_0 = \frac{n}{a^3} = \frac{4}{4.101^3} = 0.058(\text{Angstorm}^{-3}) \quad (3.2)$$

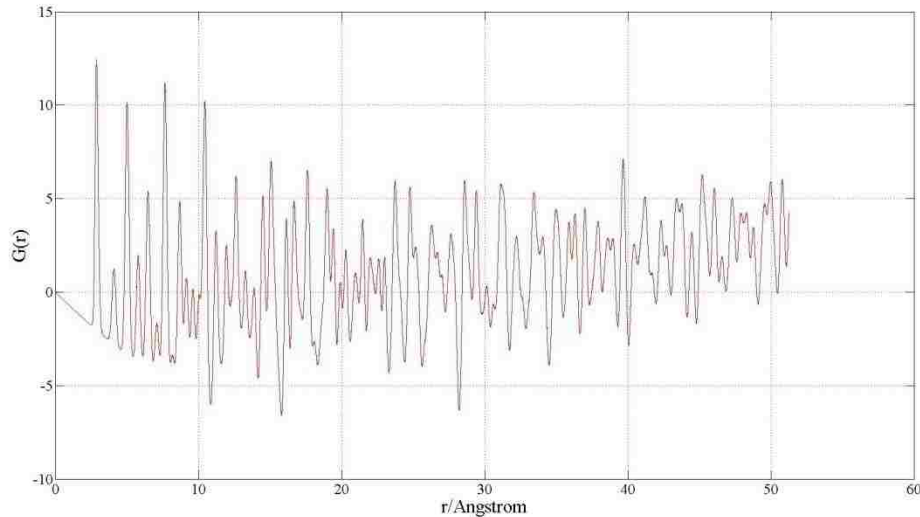


Figure 3.1 Pair Distribution Function $G(r)$ of Au Bulk

Figure 3.1 shows the $G(r)$ of gold bulk, which is created in a 3-D periodic simulation region with the length of 100 Å. From the picture it can be seen that the peaks of the function are easily distinguished, which means that the probability of finding pairs of atoms at some specific distances is extremely higher than the chance for other distances. This indicates that the structure of Au bulk is of high level of symmetry, which means the global structure remains when atoms alter position in some defined ways (e.g. four fold rotation). In this case, when there is a high probability of finding atom pairs separated by a set of well defined distances, which is illustrated by well defined peaks in $G(r)$, it implies atoms are distributed with a relatively high degree of symmetry around a given central atom. The $G(r)$ of liquid, which is shown in Figure 3.2 [32], is relatively much smoother compared with the plot above; this means the level of structural symmetry of a liquid is rather low. Note in Figure 3.2 interatomic distance (r) has been scaled by the pre-defined length scale in a Lennard-Jones. Thus, the $G(r)$ can be used as a tool to analyze the structures of different objects.

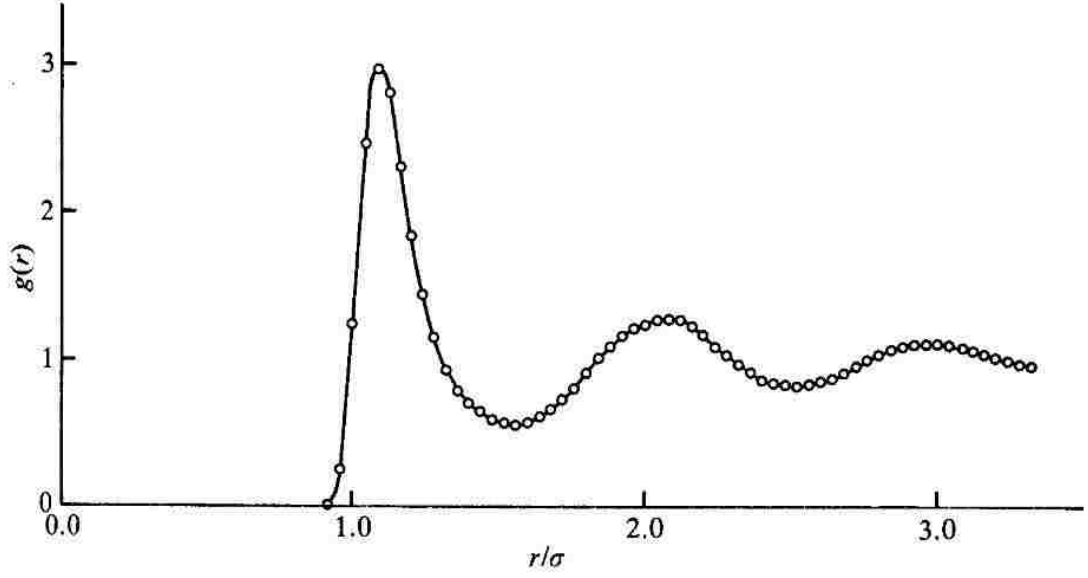


Figure 3.2 Pair Distribution Function of Lennard-Jones liquid [32]

At the atomic scale, a bulk crystal sample is essentially infinite in dimension; however, the size of nanoparticles is finite, i.e. the contribution to $\rho(r)$ of all atomic pair $\{i, j\}$ within a nanoparticle is limited to the range $0 < r_{ij} < 2R_{NP}$, where R_{NP} is the NP's radius. This means that the subtraction of ρ_0 in Equation 3.1 introduces a sloping baseline to a NP's $G(r)$ data. In fact, it is obvious that, for $r > R$, $\rho(r)$ goes to zero such that subtraction of ρ_0 is suspect. Thus, a rigorous approach to redefine the pair distribution function of a single nanoparticle with respect to its size is crucial for this analysis. In this thesis, as was done in Ref. [38], an envelope function is utilized to mathematically account for the limited spatial extent of a nanoparticle, relative to a bulk crystal. The envelope function and the corresponding pair distribution function $G(r, d)$ are given by

$$f_e(r, d) = \left[1 - \frac{3r}{2d} + \frac{1}{2} \left(\frac{r}{d} \right)^3 \right] \Theta(d - r) \quad (3.2)$$

$$G(r, d) = 4\pi r [\rho(r) - f_e(r, d)\rho_0] \quad (3.3)$$

where $d=2R_{NP}$ is the nanoparticle diameter and $\Theta(x) = 0(1)$ for negative (positive)

x is the Heaviside step function. [38][39]

Inspection of the equation (3.2) and (3.3) indicates that calculation of nanoparticle diameter d is necessary. As described above, most of the nanoparticles are cut from a bulk of gold crystal at some specific value of radius. These cut-out radii, however, are inappropriate to calculate the PDFs because at the time the NPs are created, their energy state is relatively high. This means surface relaxation occurs, typically in the form of faceting; this, in turn, means the NP radii are not stable. During the simulations, the radii of nanoparticles change in order to achieve stable configurations of atoms among the NPs. Thus, it is of great significance to define the diameter of the NPs d after they have adopted a relaxed, relatively low energy state.

We define d in equations (3.2) and (3.3) as follows. From the data generated from the MD simulations, the center of mass of each nanoparticle is calculated. Based on that value, the number density profile of a given NP can be generated with respect to the radial distance R away from the NP's center of mass ($\rho(R)$). Note this is different from $\rho(r)$ in Equations 3.1 and 3.3; the former ($\rho(R)$) denotes number density as a function of radial distance from *a given NP's center of mass* whereas the latter ($\rho(r)$) denotes pair density as a function of radial distance away from *a specific atomic position*. In this sense, $\rho(R)$ can be considered a structural characterization of the entire NP whereas $G(r)$ characterizes local atomic bonding within a given NP. The NP radial density profile $\rho(R)$ is normalized by the volume of corresponding spherical shell, $dV = 4\pi R \times dR$, where R is the radius of the shell position and dR is the increment, or thickness of each shell in the calculation. By this normalization, we are

able to compare the radial density of the NPs with the known density of the Au bulk.

Figure 3.3 shows the radial density profile for the Au nanoparticle whose initial (cut) radius was 50 Å; note, this was the largest NP simulated. From this figure, it can be seen that significant noise exists in the data for small R; for instance, significant peaks in $\rho(R)$ exist at small R. This is partly an artifact of the analysis performed: rigorously defining density in a classical atomic scale model requires a certain minimum volume. Consider that atoms in classical MD simulations are assumed to occupy point positions; this means an arbitrarily small volume element can be constructed around any atom, resulting in arbitrarily high density. As the radius of the spherical shell volume element gets larger, the density decreases accordingly. A similar situation exists here in that spherical shell volume elements, for small radius, have small total volume, skewing densities artificially high. This is further evidenced by Fig. 3.3 because, for $R > 15$ Å, fluctuations in density are significantly reduced, with a running average very near the bulk value ($\rho_0 = 0.058 \text{ \AA}^{-3}$). Indeed, for $25 \text{ \AA} < R < 47 \text{ \AA}$, density data for the NP are very similar to what is obtained for bulk behavior. For large enough R, density data go to zero, reflecting the spatial extent of the NP; this guides calculation of NP radius. We define the radius of a nanoparticle as the distance where the density profile – as it decreases to zero for the final time – crosses half the average density of the bulk; d for the NP is two times this value. For the NP shown in Fig. 3.3, $d = 98.4 \text{ \AA}$. While the difference between this and the nominal value obtained from the cut-out diameter is small (1.6%), it becomes more significant for smaller NPs.

With a rigorous definition of d in hand, it was possible to perform $G(r)$ analysis, employing the proper envelope function as described above. Figure 3.4 illustrates $G(r)$ for the largest NP simulated ($d=49.2 \text{ \AA}$).

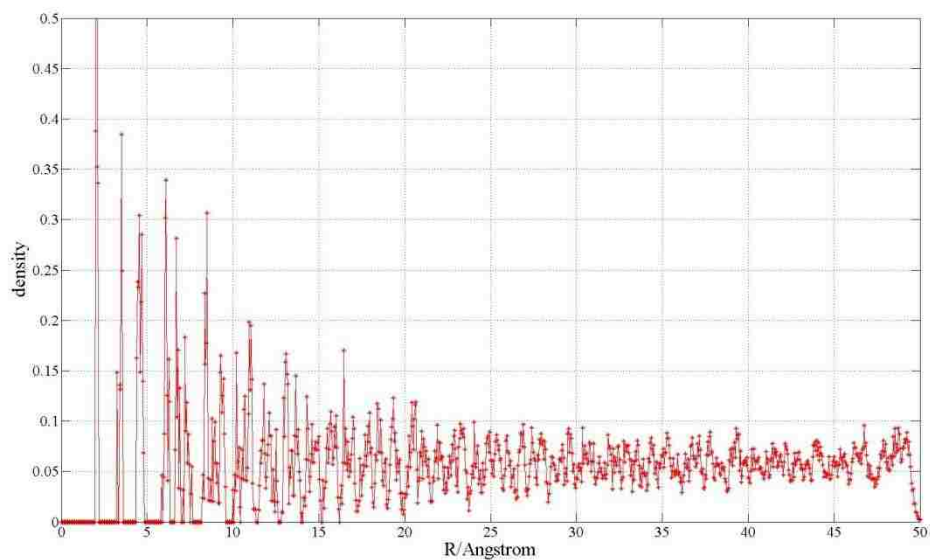


Figure 3.3 Radial Density Profile of $R_{NP} = 49.2 \text{ \AA}$ Au Nanoparticle

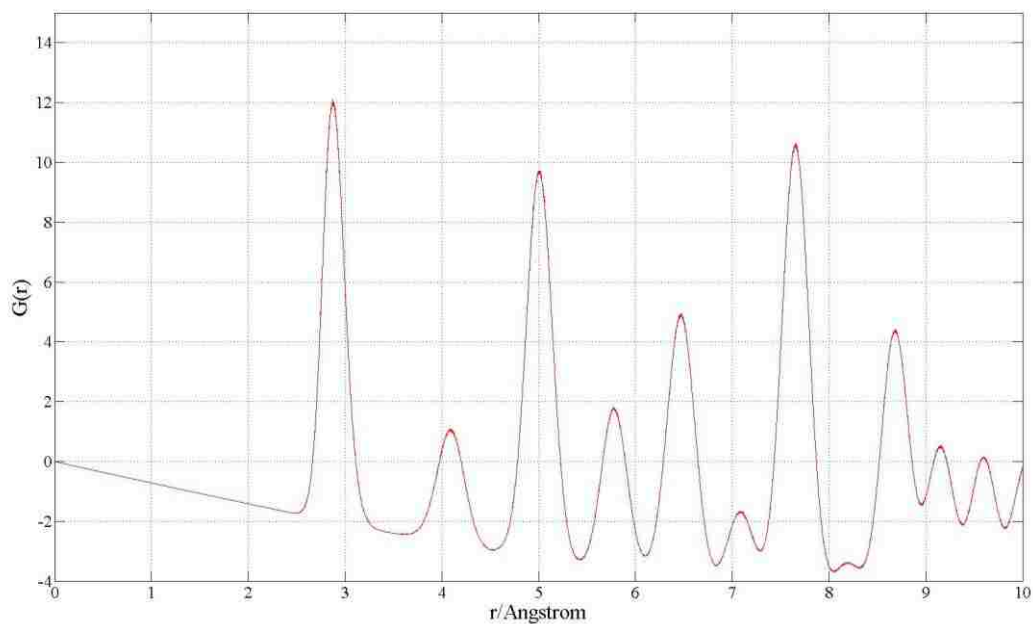


Figure 3.4 Pair Distribution Function of $R_{NP} = 49.2 \text{ \AA}$ Au Nanoparticle

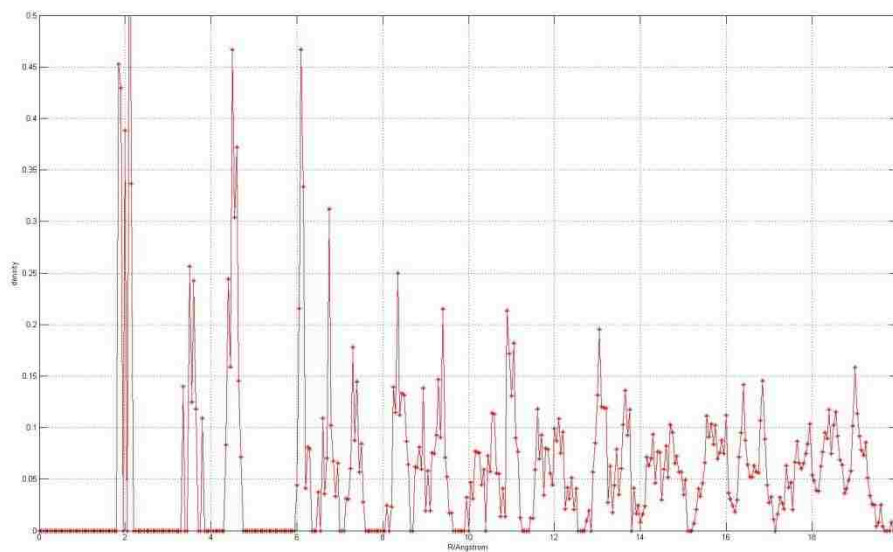


Figure 3.5 Radial Density Profile of $R_{NP} = 19.7$ Å Au Nanoparticle

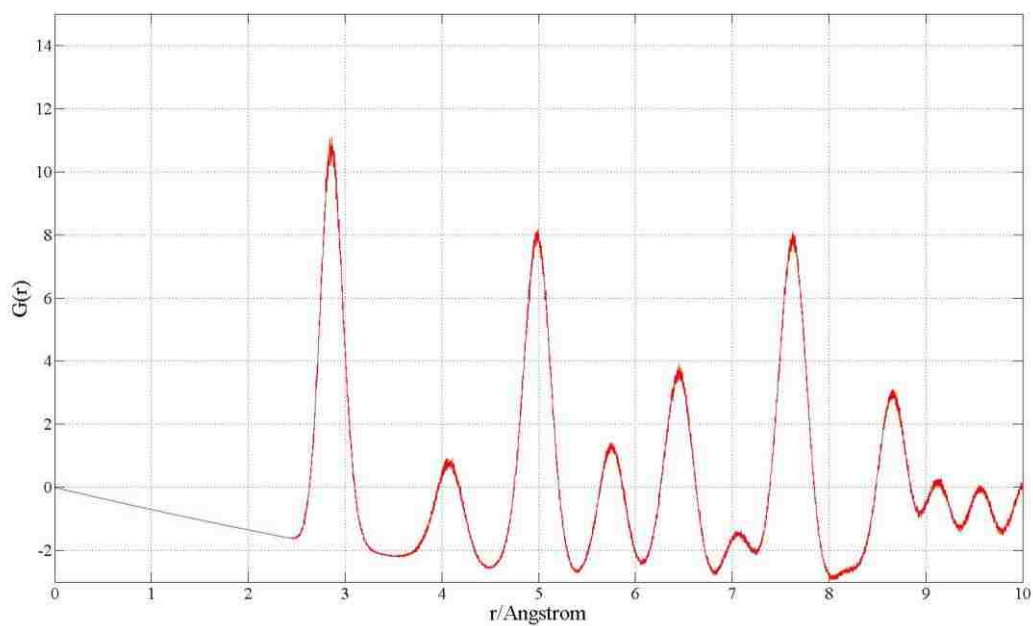


Figure 3.6 Pair Distribution Function of $R_{NP} = 19.7$ Å Au Nanoparticle

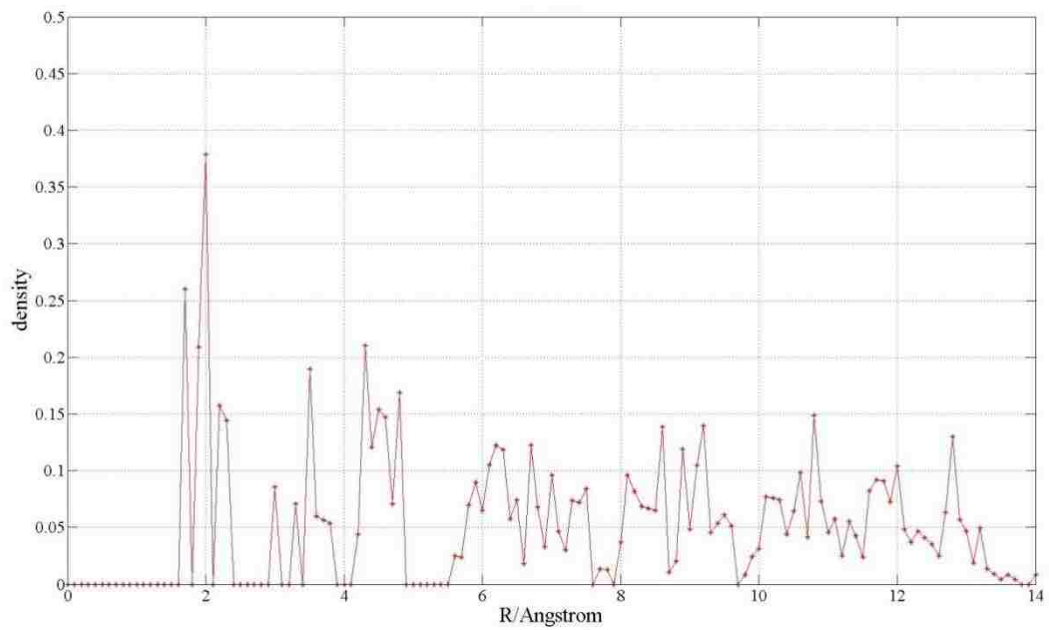


Figure 3.7 Radial Density Profile of $N=600$ ($R_{NP} = 13.3 \text{ \AA}$) Au Nanoparticle

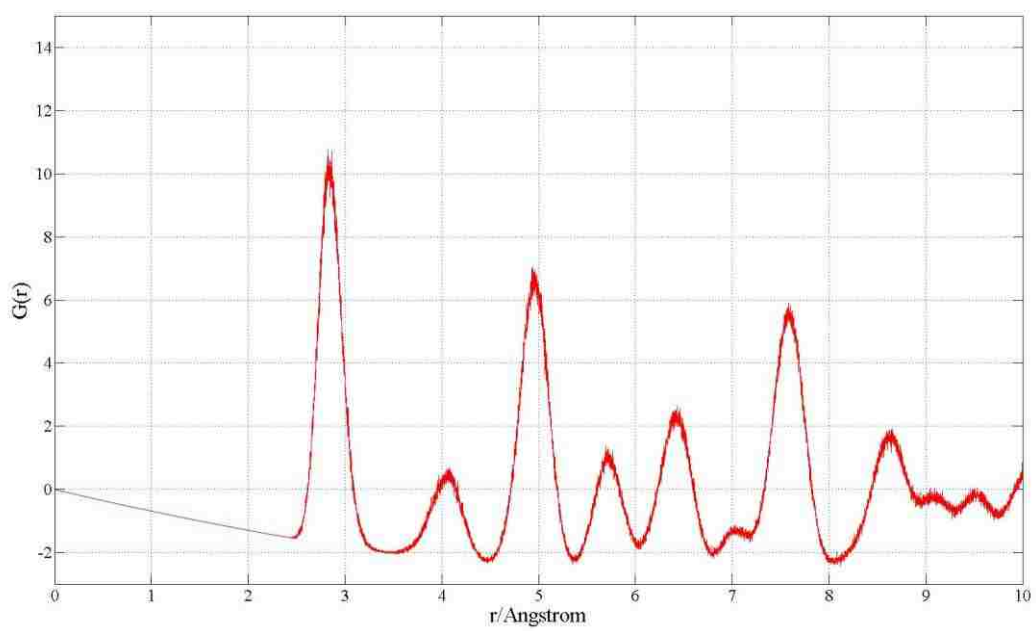


Figure 3.8 Pair Distribution Function of $N=600$ ($R_{NP} = 13.3 \text{ \AA}$) Au Nanoparticle

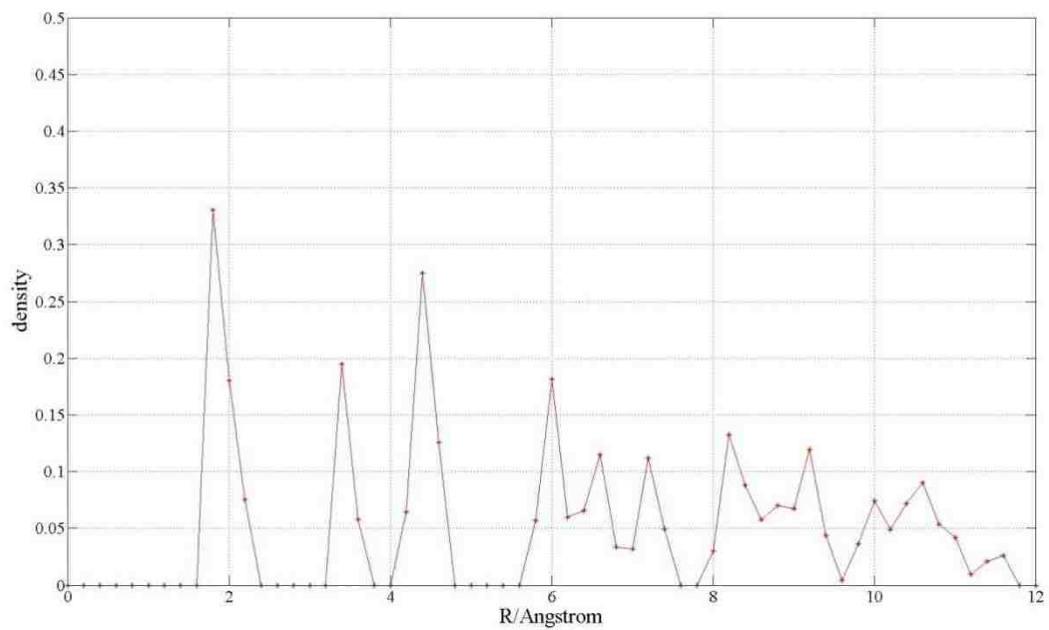


Figure 3.9 Radial Density Profile of $R_{NP} = 11.1 \text{ \AA}$ Au Nanoparticle

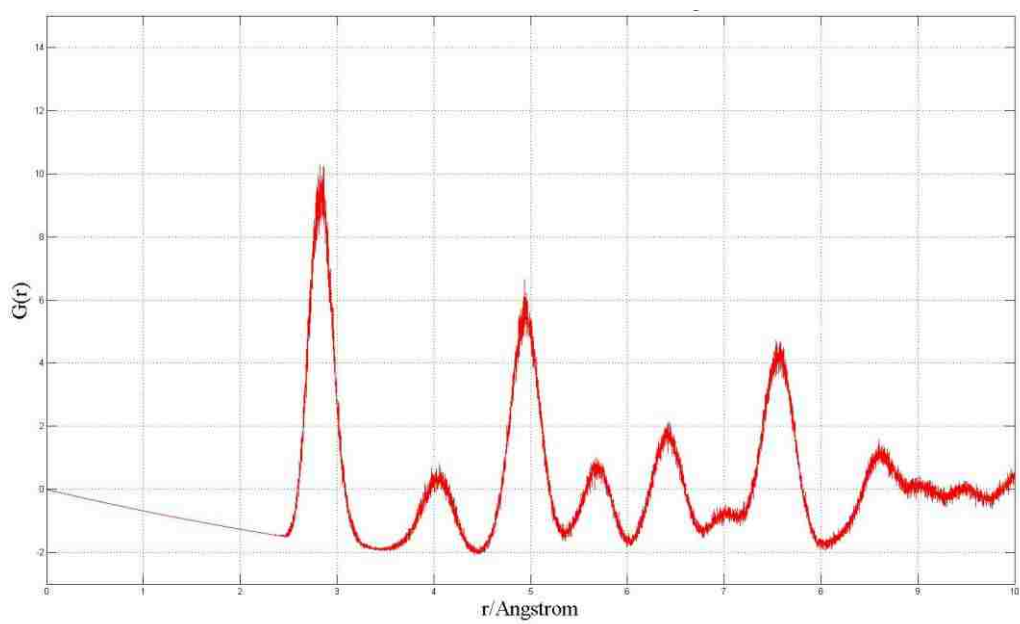


Figure 3.10 Pair Distribution Function of $R_{NP} = 11.1 \text{ \AA}$ Au Nanoparticle

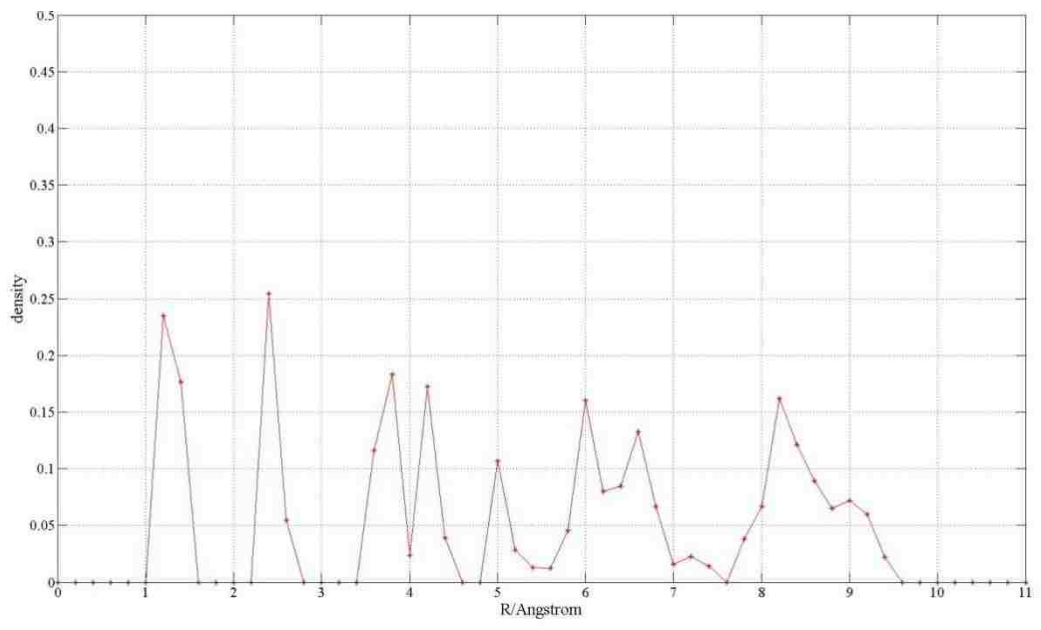


Figure 3.11 Radial Density Profile of $R_{NP} = 9.3 \text{ \AA}$ Au Nanoparticle

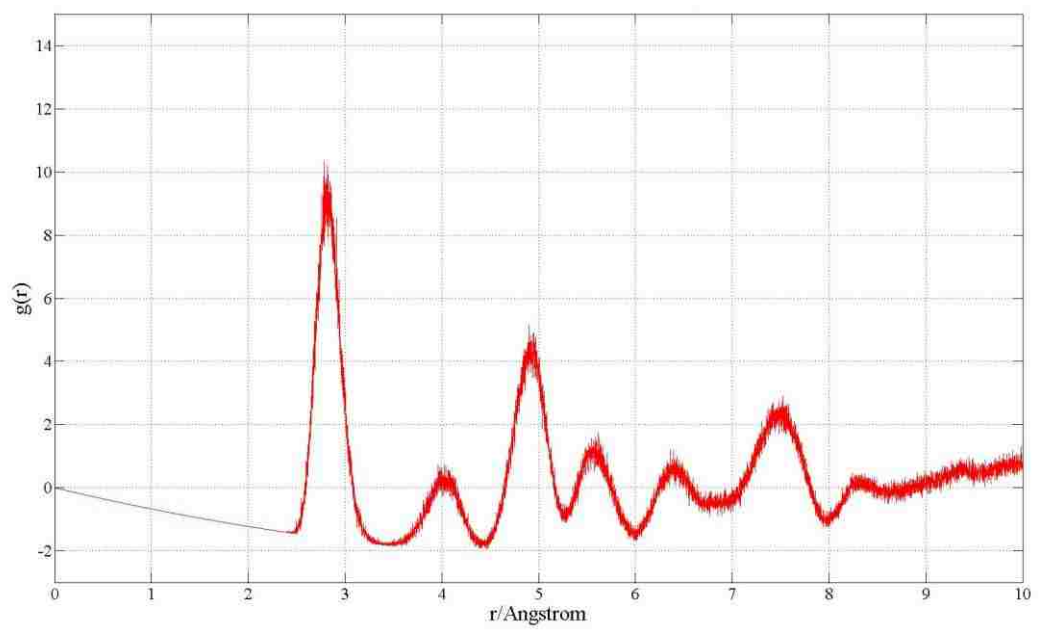


Figure 3.12 Pair Distribution Function of $R_{NP} = 9.3 \text{ \AA}$ Au Nanoparticle

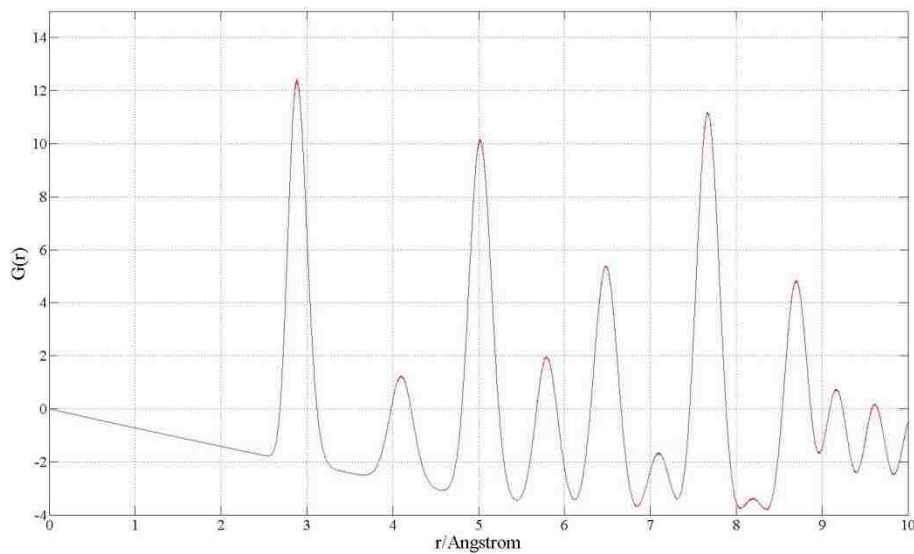


Figure 3.13 Pair Distribution Function of Au bulk within the same range as NPs'

In addition, Figures 3.5 to Figure 3.12 provides four additional sets of radial density profiles and pair distribution functions for four nanoparticles with radii decreasing as 19.7, 13.3, 11.1, and 9.3 Å, respectively. The truncated peaks in Figure 3.3 and Figure 3.5 have magnitudes of $\sim 1.1 \text{ \AA}^{-3}$ and $\sim 0.7 \text{ \AA}^{-3}$, respectively. In total we have simulated 33 Au nanoparticles with different sizes and all $\rho(R)$ and $G(r)$ data for other NPs which are not illustrated here are put in Appendix A. The examples contained here were chosen because they represent well relevant features observed in all obtained NP data. For the purpose of comparison, the $G(r)$ of bulk is extracted within the same ranges of coordinates in Figure 3.13.

It is observed that as the size of nanoparticles decreases, the number density profiles lose any resemblance to the relatively smooth profiles seen for large NPs and the bulk (Fig. 3.3). Above, for the $R_{\text{NP}}=49.2 \text{ \AA}$ NP, it was discussed that there exists large noise in $\rho(R)$ for $R < 15 \text{ \AA}$, therefore it is expected that noisy behavior would dominate $\rho(R)$ for small NPs. Indeed, the smallest NPs simulated show peaks

throughout their $\rho(R)$ profile. There are two main factors that may cause this phenomenon. First, the number of atoms decreases cubically compared with the NP radius. There are 30427 atoms in $d=100$ Å nanoparticle but only 236 in $d=20$ Å NP. During the calculation for those small particles ($N < 500$, or $R_{NP} < 12.7$ Å) the limited number of sample is anticipated to introduce large statistical variations, which causes the profiles of small NPs to manifest distinct peaks. Second, while the statistics of sampling small volumes should be taken into account, the peaks in number density profiles actually indicate the existence of atoms layering with respect to the center of mass. For small nanoparticles, this layering may persist through the whole particles. It is also found that the first peak in $\rho(R)$ figures becomes smaller as R_{NP} decreases, which demonstrates that the number of atoms in the first layer gets fewer. It provides evidence that the small NPs are less structurally ordered than the relatively big ones. Meanwhile, in all 33 plots, the first peak positions in $\rho(R)$ are all 2 Å away from center of mass. In other words, for all NPs simulated, there is no atom sitting directly at the center of mass. This lends strong evidence that atomic layering with no atom at the center of mass is the stable structure of small NPs at equilibrium.

While analysis of $\rho(R)$ provides some characterization of the NP as a whole, data are too noisy to conclude whether lattice compression can be observed for small NPs. In fact, as discussed above, density peaks at small R decrease in magnitude for smaller NPs; however, this is misleading because it is a reflection of atomic ordering, rather than actual particle density. To detect lattice compression, we instead analyze atomic bond distances: a compressed lattice will exhibit nearest neighbor atomic

spacings smaller than the equilibrium, or bulk crystal, value. Thus, more detailed considerations and analysis need to be applied on the atomic structural property of those nanoparticles, which can be found from the pair distribution function $G(r)$. With a rigorous definition of d in hand, it was possible to perform $G(r)$ analysis, employing the envelope function as described above. Figure 3.4 illustrates $G(r)$ for the largest NP simulated ($d=49.2 \text{ \AA}$) and results for smaller NPs are shown in Figs. 3.6, 3.8, 3.10, and 3.12.

As mentioned above, $G(r)$ yields information on the local structure, i.e. the mutual arrangement of the atoms at short distances. In this thesis, the positions of first peak of $G(r)$ of nanoparticles with varying size are analyzed. $G(r)$ is the probability to find a pair of atoms apart away for r , so the position of first peak of $G(r)$ actually gives the value of the nearest interatomic length within the corresponding nanoparticle. According to the structural configuration of fcc crystal, this length is the effective lattice constant multiplied by $\frac{\sqrt{2}}{2}$. Thus, in this way, the compression of the nanoparticle from being created to equilibrium state can be found. Prior to considering lattice contraction, however, some general observations of NP $G(r)$ are made here.

From the above figures of $G(r)$ for different NPs, it can be seen that peaks in $G(r)$ become broader as the size of NPs decrease. As mentioned above, $G(r)$ gives the statistical probability to find a pair of atoms apart away for r and therefore reflects the degree of symmetry around a given central atom. Thus, the sharper the peaks are, the more well-defined are the separation distances of pairs of atoms; consequently, this

indicates a higher level of structural symmetry the local structure is. Hence, this inspection can be considered as evidence that Au NPs exhibit less symmetry as the radii decreases. Besides, in the range $8 \text{ \AA} < R < 10 \text{ \AA}$, there are clear peaks in the $G(r)$ figures of gold bulk and large NPs ($d=100, 40 \text{ \AA}$), while peaks in that range in $d=27 \text{ \AA}$ NP become difficult to distinguish. If the size of NP gets even smaller, those peaks almost vanish. This phenomenon also indicates that the degree of symmetry of NP's structure tends to be lower as the radius becomes small. At last, the position of the first peak of $G(r)$ shifts to small values for small NPs. This will be discussed in detail below.

3.2 The Effect of Surface Stress and Pair Distribution Function Analysis

The focus of the thesis is to use atomic scale simulations to examine if the isostatic pressure due to surface stress can be detected as lattice compression via $G(r)$ analysis. It is well known that for a liquid drop, surface induced pressure is $P = 2\gamma/R_D$, where γ is surface energy and R_D is drop radius. An analogous situation is expected for solids but with γ replaced by surface stress f . For an isotropic surface, such as for a liquid drop, f has one value; however, for crystal surfaces, f is anisotropic within a surface (i.e. it is represented as a 2×2 tensor). Furthermore, f varies from one crystallographic surface to another. As mentioned previously, the NPs simulated herein undergo surface relaxation during their

equilibration stage. This relaxation is in the form of faceting; specifically, as best as a given NP is able to do so, it forms surface facets of either [001], [010], or [111] orientation. These are the lowest energy surface terminations for face centered cubic (fcc) Au. Note that faceting is not always complete (i.e. structurally frustrated regions exist where some facets meet). Nonetheless, the majority of the surface area for all NPs simulated here was comprised of the three low index crystal surfaces above. As such, it was necessary to compute the surface stress for those three crystallographic surface orientations.

3.2.1 Surface Stress Calculation

In this section, the calculation of surface stress will be shown in two aspects, calculation for the whole system of gold surface and computation on each atom. The former will provide the thermodynamic surface stress for different orientations, i.e. $\langle 0 0 1 \rangle$, $\langle 1 1 0 \rangle$, and $\langle 1 1 1 \rangle$; the latter approach will permit analysis of the effect of surface stress on atoms that are successively farther from the planar crystal free surface.

As mentioned in Chapter 2.4, the planar surface stress calculations were done using systems of gold crystal lattices with periodic boundary conditions in x and y but not in z, so as to form free surfaces in z. There were three surface simulation systems formed in this fashion, one each for the three orientations, i.e. $\langle 0 0 1 \rangle$, $\langle 1 1 0 \rangle$, $\langle 1 1 1 \rangle$ to be studied. In LAMMPS, a symmetric pressure tensor, stored as a 6-element

vector, is calculated by the following equation:

$$P_{ij} = \frac{\sum_k^N m_k v_{ki} v_{kj}}{V} + \frac{\sum_k^N r_{ki} f_{kj}}{V} \quad (3.4)$$

where i, j denote $x, y,$ and z, V is the volume. The numerators of the first and second terms are components of the kinetic energy tensor and components of the virial tensor, respectively. [35] For a bulk (3D periodic) system at equilibrium, all $\langle P_{ij} \rangle$ components are zero. Upon removing periodic boundary conditions in z and forming free surfaces, the in-plane P_{ij} terms (P_{xx} and P_{yy}) become finite, indicating the presence of surface stress. Equation 3.4 shows division by the system volume. However, we only wanted to normalize by the cross section area to obtain the stress. Thus, the output results were multiplied by the respective simulation box dimension in z . Lastly, since there are two free surfaces in each simulation system, we also need to yield the stress value by dividing the result by 2. The calculation result of shear component of pressure tensor P_{xy} is relatively small compared with normal stresses P_{xx} and P_{yy} , $P_{xy} \sim 10^{-3} P_{xx}$ or P_{yy} , and P_{xx} and P_{yy} are in the magnitude of 10^3 bars. In other words, it is safe to assume that P_{xy} is statistically zero in these simulations and this is a result of high symmetry in the low index fcc surfaces. Therefore, we only consider the normal components of surface stress in this thesis.

The pressures tensor is calculated via LAMMPS directly in each output simulation time step. The average value of P_{xx} and P_{yy} are generated by MATLAB codes then converted into stress values by the method described above. The result of the surface stress values are shown in Table 3.1, under two different dimensions, J/m^2 and $eV/\text{\AA}^2$.

Stress	f_{xx}		f_{yy}	
	J/m^2	$eV/\text{\AA}^2$	J/m^2	$eV/\text{\AA}^2$
Surface <0 0 1>	1.80	0.112	1.81	0.113
Surface <1 1 0>	1.91	0.119	1.35	0.084
Surface <1 1 1>	2.05	0.128	2.05	0.128

Table 3.1 Surface Stress Normal Components Calculation through the whole bulk

From the table above, it can be seen that all the values are positive, which yields the stress is tensile in nature. [35] This means the surface would relax to smaller plane area if unconstrained by the crystal structure below it. We can also observe that the values of surface stress in x- and y-direction are statistically identical except for <1 1 0> free surface. This indicates that surface deformation in the x- and y-directions for <0 0 1> and <1 1 1> are energetically equivalent. This situation, however, is not the case for the <1 1 0> surface, so the values of stress components in different directions differ from each other. Put differently, equivalent deformations in the x and y directions on the <1 1 0> surface have different energy changes associated with them. This anisotropy is a result of atomic structure on the <1 1 0> surface. On the <1 1 0> surface, the configurations of atoms along the line of x-axis ([$-1\ 1\ 0$]) and y-axis ([$0\ 0\ 1$]) are different so if the deformations along these two directions are equivalent, the corresponding changes of stress, or energy are not identical. The situation does not happen on either <0 0 1> or <1 1 1> surfaces, as the arrangements of atoms along the x-axis ([$1\ 0\ 0$]) and y-axis ([$0\ 1\ 0$]) of <0 0 1> surface are exactly same while the atomic configurations along the x-axis ([$1\ 0\ -1$]) and y-axis ([$-1\ 2\ -1$]) of <1 1 1>

surface are also identical.

By the command “compute stress/atom” in LAMMPS, stress components of each atom can be calculated and written into dump files at user-specified intervals; this information can be output along with each atom’s position. As such, it is possible to identify how atomic scale stress varies as a function of distance from a free planar crystal surface. With the atomic coordinates, it is possible for us to assign each atom to a crystallographic layer in the free surface systems. Subsequently, the average value of stress in each layer was found. Consequently, the effect of surface stress can be seen by observing the configuration of stress versus z , i.e. the depth perpendicular to the free surface. Figure 3.14 to 3.16 show the surface stress configuration on $\langle 0\ 0\ 1 \rangle$, $\langle 1\ 1\ 0 \rangle$, and $\langle 1\ 1\ 1 \rangle$ free-surface gold bulk, respectively. We can observe that the stress values are in energy units because in LAMMPS the value of stress on a per atom basis is output without being divided by any volume term. As such, the y-axis label on Figures 3.14-3.16 should be stress multiplied by volume. In fact the value can be normalized by the bulk equilibrium value of atomic volume to make those values have the proper dimension of stress but this is not necessarily the correct volume value for surface atoms. Nonetheless, since we simply focus on how far the surface stress effect goes to zero from the surface, it is not necessary to take the specific magnitude of stress into account in this analysis.

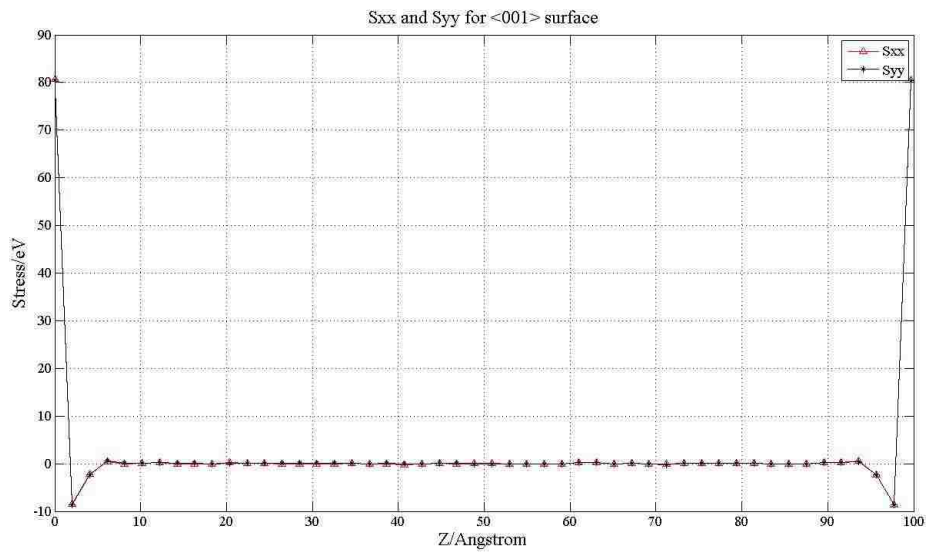


Figure 3.14 Surface Stress Configuration of <0 0 1> free-surface gold bulk

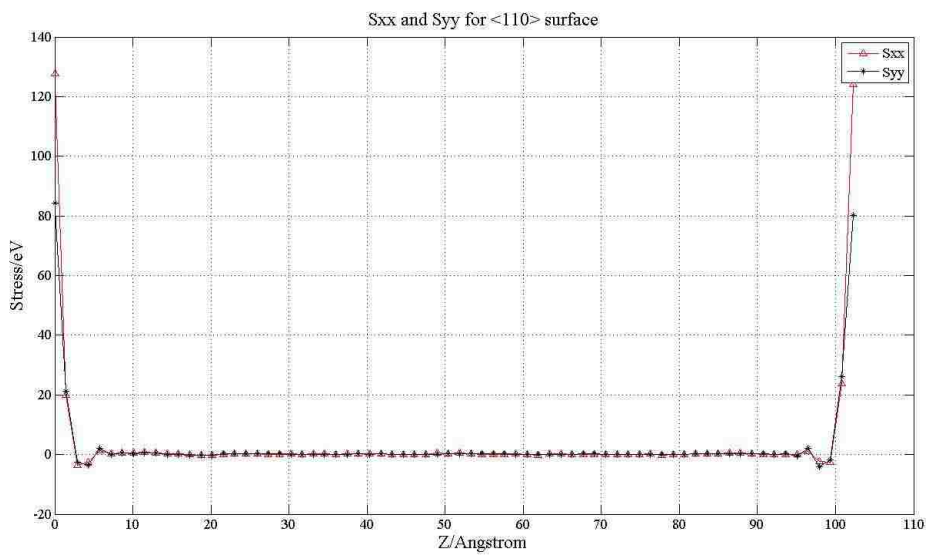


Figure 3.15 Surface Stress Configuration of <1 1 0> free-surface gold bulk

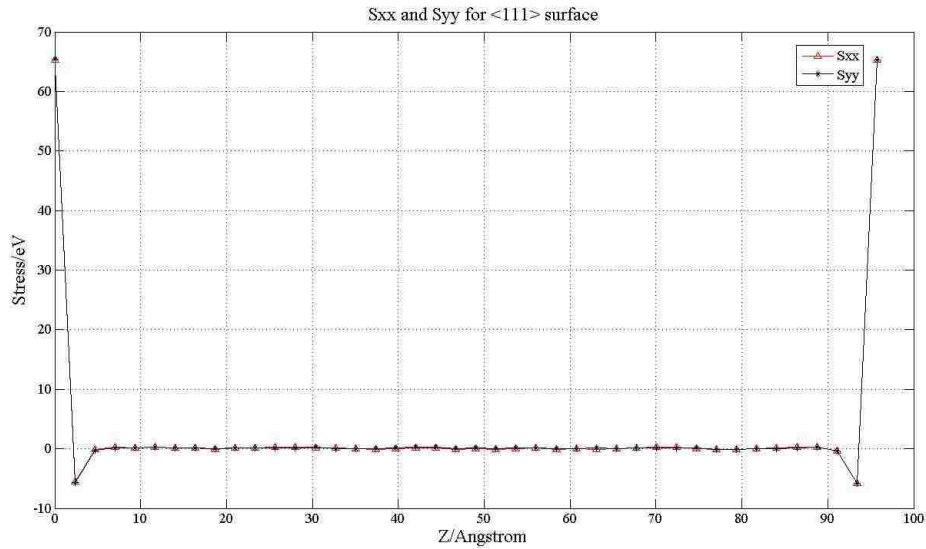


Figure 3.16 Surface Stress Configuration of <1 1 1> free-surface gold bulk

From those figures it can be seen that only several outer layers have non-zero stress and the depth into the crystal of effective stress region is only about 7-8 Å. This depth of surface stress effect is of significance to evaluate the surface effect on Au nanoparticles.

3.2.2 Pair Distribution Function $G(r)$ Analyses of Gold Nanoparticles

As mentioned above, the first peaks in $G(r)$ give the nearest neighbor distance of atoms, which is further related to the effective lattice constant of NPs. Figure 3.17 shows three sets of the first peak of $G(r)$, including the bulk's, the largest NP's ($R_{NP}=49.2$ Å), and the smallest NP's ($R_{NP}=9.3$ Å). It can be easily seen that the first peak position shifts to smaller value for smaller NPs. Note that it is difficult to distinguish the first peak curves of bulk and $R_{NP}=49.2$ Å NP, for the value of peak position of that NP is only subtly smaller than bulk's.

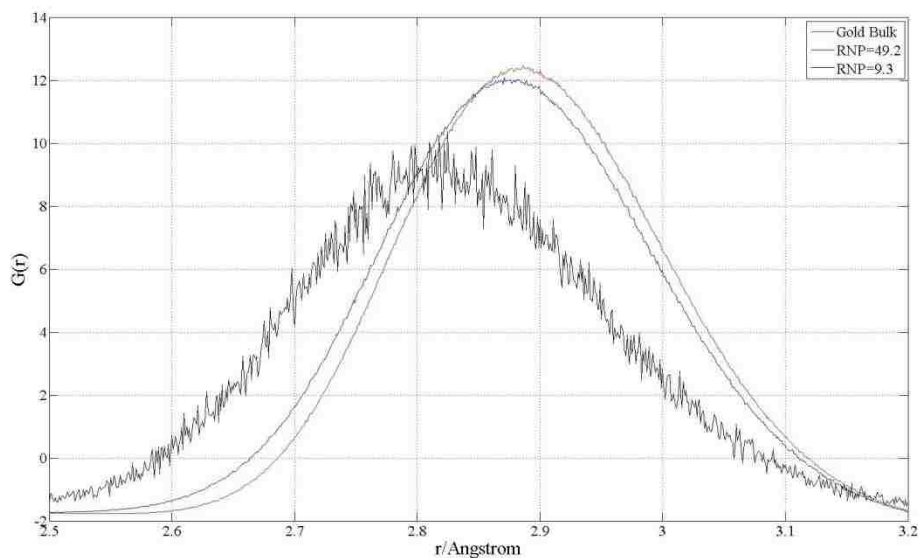


Figure 3.17 First Peaks of $G(r)$ of Gold Bulk, $R_{NP}=9.3, 49.2 \text{ \AA}$ NPs

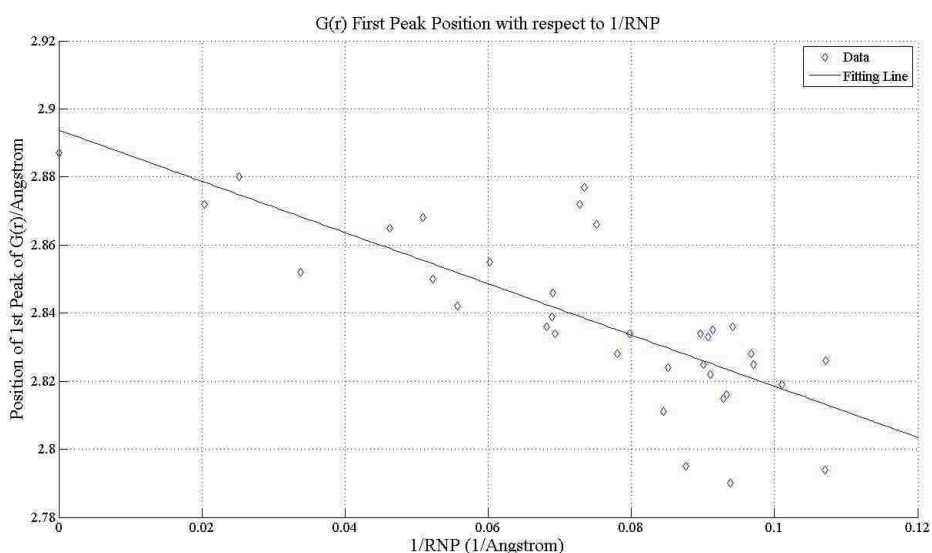


Figure 3.18 $G(r)$ First Peak Position of Au nanoparticles

In Figure 3.18, we plot the first peak position in $G(r)$ for each of the nanoparticles simulated versus $1/R_{NP}$. Since the fcc lattice constant is directly related to the nearest neighbor atomic spacing, Figure 3.18 shows that the effective lattice constant decreases as the size of NP becomes smaller. We fitted the data with a line, which is expressed as $y = -0.753 \left(\frac{1}{R_{NP}} \right) + 2.89$, where y is the position of $G(r)$ first peak,

and the dimension of y and R_{NP} is \AA . It should be noticed that there exists significant scatter in Figure 3.18. This is mainly due to the limited number of sample atoms in each NP system which leads to unfavorable statistics, and the way we determine the first peak position. As described above, the number of atoms in system drops dramatically as the size of NP decreases. By comparing the $G(r)$ curves in Figure 3.17, we can see clearly that there are much more significant variations in $R_{NP}=9.3$ curve than the one of $R_{NP}=49.2$, which is caused by the small number of atoms. $G(r)$ curve was calculated as a histogram in MATLAB. We determine the first peak position as the position occupied by the highest column of $G(r)$ histogram. For bulk and large NPs, the first peak position found in this way is in great agreement with the ideal one. However, the data variation gives rise to larger deviations in the calculated position. As a result, the first peaks of small NPs are less rigorously defined in a statistical sense. With y intercept fixed, the slope needed to have 90% of the data points below a line is -0.60 \AA^2 ; furthermore, -0.99 \AA^2 is the one needed to make 90% of the data points above it. These two values provide the error bounds of this line fitting.

Using lattice constants obtained from the initial fit decided above, several bulk Au simulation samples were created and run in MD under 3-D periodic boundary conditions and subjected to NVT ensemble at $T=300\text{K}$; from these simulations, the dependence of pressure on lattice constant was obtained. This, in turn, allows us to connect the first peak position in $G(r)$ for each NP to a corresponding bulk pressure. Results are shown in Figure 3.19, including a linear fit of the data points $P = 1.59 \times 10^6 \left(\frac{1}{R_{NP}}\right) - 1.75 \times 10^3$. All the dimension is the default of LAMMPS, i.e. pressure in

bar and $1/R_{NP}$ in \AA^{-1} .

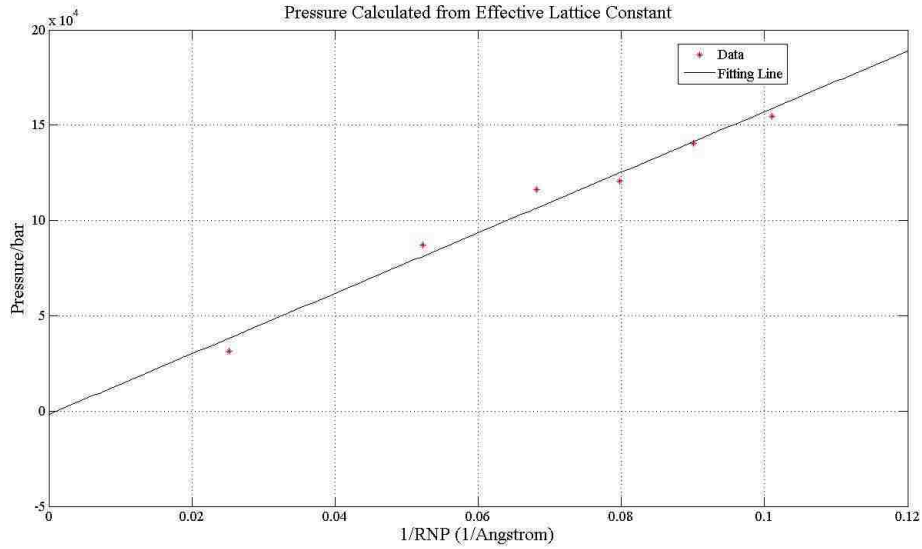


Figure 3.19 Effective Pressure of Au nanoparticles

We assume that pressure difference inside Au NPs is given by $\Delta p = \frac{2f}{R_{NP}}$, where f is an average surface stress. Comparison between this equation and the formula of the fitting line indicates that the slope of the fitting line provides the value of two times the surface stress, which yields that $f = \frac{1.59 \times 10^6}{2} \text{ bar} \cdot \text{\AA} = 7.94 \text{ J/m}^2$; this value is much higher than the values in Table 3.1. Note from the error estimate given previously for the first $G(r)$ peak position as a function of $1/R_{NP}$, we can compute a range of predicted surface stress as $6.3\text{-}10.6 \text{ J/m}^2$. This result seems to demonstrate that surface stress is relatively much larger in NPs than in bulk material, *even for the minimum estimate value*. However, we investigate this further below.

3.2.3 Surface Effect Discussion

Figure 3.14 to 3.16 illustrate that the surface stress influences atoms to a depth of

about 7 to 8 Å below a planar crystal surface. Hence, it is reasonable to distinguish those atoms among each nanoparticle that are located within a sphere whose radius is ($R_{\text{NP}} - 7 \text{ Å}$); these are core atoms. Correspondingly, atoms in a NP but outside this inner (core) sphere can be thought of as surface atoms. If the influence of surface stress is typically constrained to atoms within $\sim 7 \text{ Å}$ of the free surface, then it is reasonable to conclude that atoms in the surface region collectively exert pressure on atoms in the core region. The mechanical analog is that of an elastic skin which is under tension and an elastic core in compression. With this concept, we can repeat the entire analysis above but only using core atoms in the analysis (i.e. $G(r)$ calculation, first peak position analysis, and fitting for stress value). By comparing the result of core atoms only and of all atoms, the surface pressure effect can be shown more clearly.

Figure 3.20 and 3.21 are examples of comparisons between the first peaks in $G(r)$ computed for core atoms only and $G(r)$ computed using all atoms in the nanoparticle (the examples shown are for $R_{\text{NP}} = 19.7 \text{ Å}$ NP and $N = 450$ NP ($R_{\text{NP}} = 11.8 \text{ Å}$)). It can be seen for the larger NP that the first peak for $G(r)$ of the core atoms is fairly similar to $G(r)$ computed for all atoms in the NP. For the smaller NP, the difference between the first $G(r)$ peak computed using only core atoms versus all atoms is greater. More specifically, the shift to smaller distance for the peak position is *less* when only core atoms are considered. This is also true for the larger NP data in Fig. 3.20, but to a lesser degree. This means that, on average surface atoms adopt shorter bond lengths than core atoms do. This is because compared with core atoms, surface atoms have fewer bonding neighbor atoms so they shift to positions closer to their remaining

neighbors. As R_{NP} decreases, the surface-to-volume ratio becomes larger, since it is proportional to $1/R_{NP}$. Note however that this does not account for the assumption made herein that the surface region has finite (and non-trivial) thickness. Thus, the percentage of surface atoms among the whole atoms of NP increases. Hence, the first peak position of $G(r)$ shifts to smaller value for smaller NPs; however some part of the overall observed shift is caused by surface bond contraction, which is more significant on average than core bond compression.

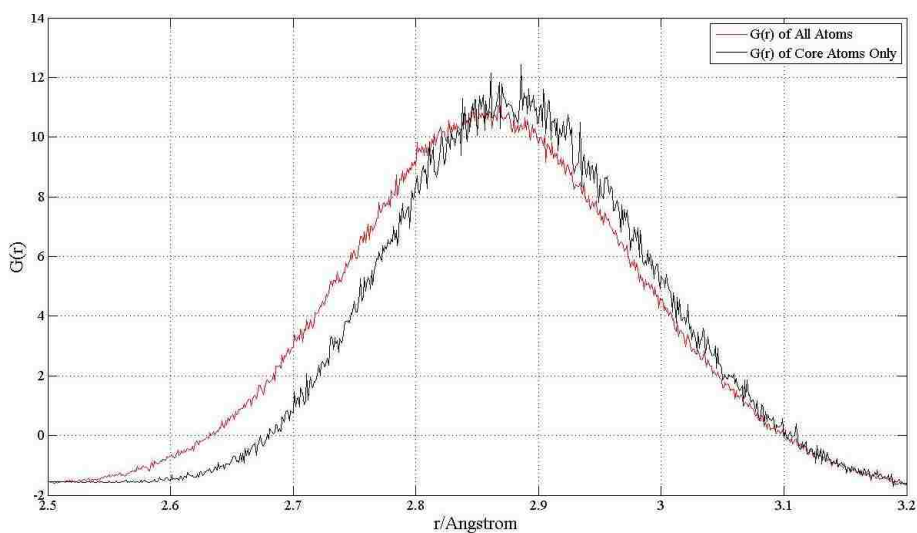


Figure 3.20 First Peaks of $G(r)$ of $R_{NP}=19.7$ Au nanoparticles

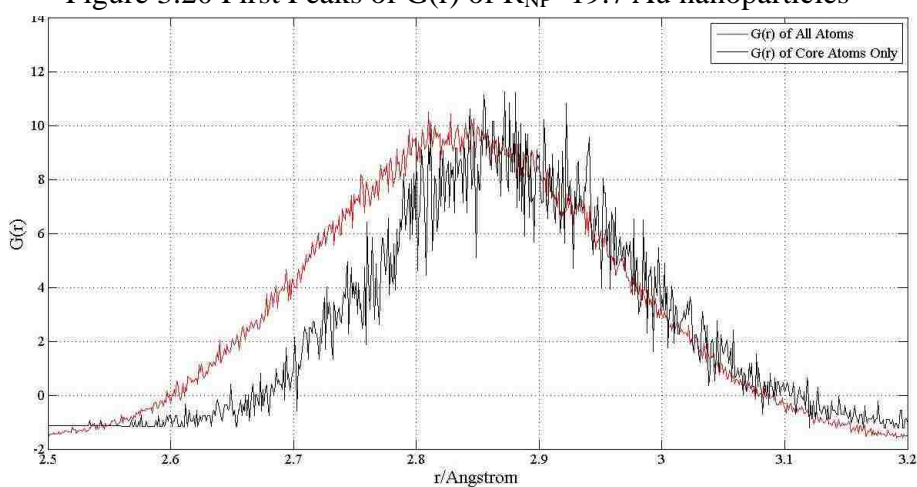


Figure 3.21 First Peaks of $G(r)$ of $N=450$ ($R_{NP}= 11.8 \text{ \AA}$) Au nanoparticles

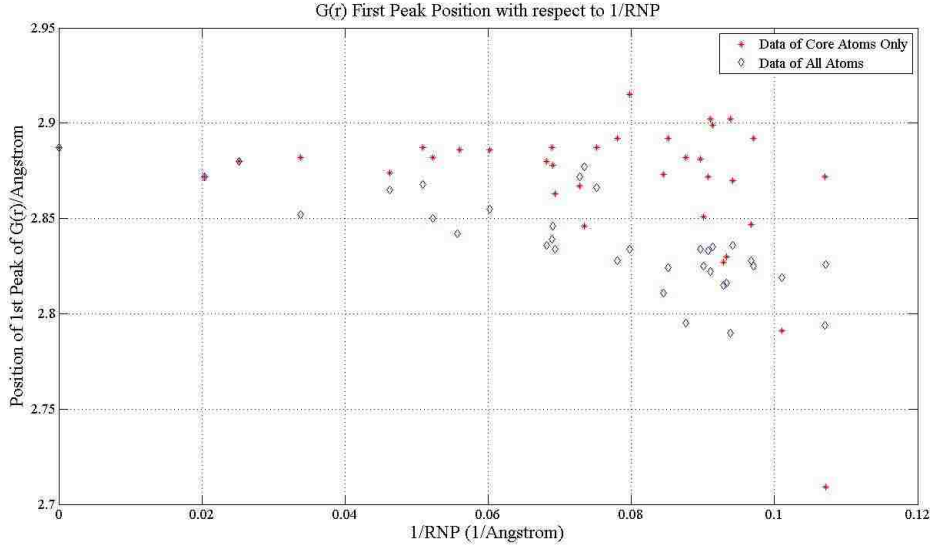


Figure 3.22 G(r) First Peak Position Data for Core Atoms and Whole NPs

The first peak position analysis was performed for G(r) obtained from core atoms only. From Figure 3.22 it can be seen that the first peak position for G(r) computed from only core atoms depends much less significantly on R_{NP} . The fitting of the core data yields $y = -0.255 \left(\frac{1}{R_{NP}} \right) + 2.89$, where y is the position of G(r) first peak. This gives a relationship between the effective lattice constant of core atoms and R_{NP} . Note there is significant noise in the first peak positions of G(r) as computed for core atoms only. Statistical variation is more significant for smaller NPs; the same was true for the first G(r) peak position computed for all atoms. This is caused by the small sample statistics of small NPs and the way we determine the first peak position as mentioned above. Herein, the error bounds (i.e. the slope needed to have 90% of the data points below and above a line with y intercept fixed) are given as -0.01 and -0.52 \AA^2 . Given the initial fit, the pressure calculation based on the effective lattice constant can be found as $P = 4.44 \times 10^5 \left(\frac{1}{R_{NP}} \right) + 7.59 \times 10^3$, which gives that the stress $f = \frac{4.44 \times 10^6}{2} \text{bar} \cdot \text{\AA} = 2.22 \text{J}/\text{m}^2$. The error bounds provide the minimum and maximum

predictions of the stress value as $0.2 J/m^2$ and $4.4 J/m^2$, respectively. While this is a wide range of predicted surface stress, it forms bounds around the values listed in Table 3.1 for the planar free surfaces. Recall this was not the case for the surface stress range predicted using all atoms in the NPs. This gives evidence that, even for small NPs, the surface stress is some roughly linear combination of surface stress values of different low index surfaces, corresponding to different facets on the NP surface. However, the very significant error makes it impossible for us to identify whether the thermodynamic surface stress values change for small enough NPs.

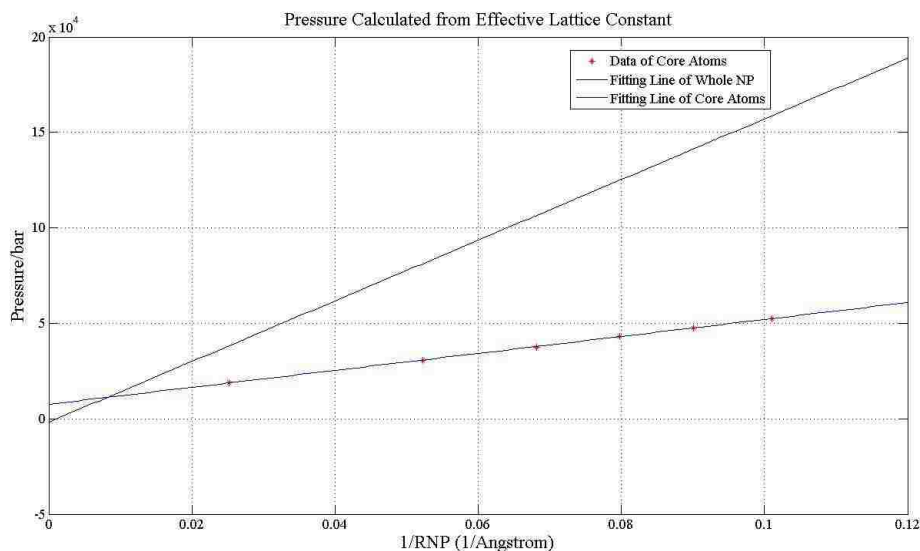


Figure 3.23 Effective Pressure Core Atoms of Au nanoparticles

Further discussion to illustrate statistical challenges to our analysis comes from considering the number of core atoms versus R_{NP} . Figure 3.24 and 3.25 show the number of core atoms versus the number of atoms in the entire nanoparticle. As expected from geometries consideration, when the total number is larger than 1000, the relationship between these two numbers is basically linear; however, for $N < 1000$ atoms, the relationship becomes quasi-stepped which is shown in Figure 3.25. This

analysis shows that, for sufficiently small NPs (i.e. $N < 250$), it is no longer reasonable to define a core – that is, every atom in the NP is a surface atom, indicating its bonding environment is distinctly altered from what is expected from bulk behavior. This may indicate a size regime where, for instance, catalytic properties of Au NPs may shift as atomic bonding throughout the NP becomes highly strained.

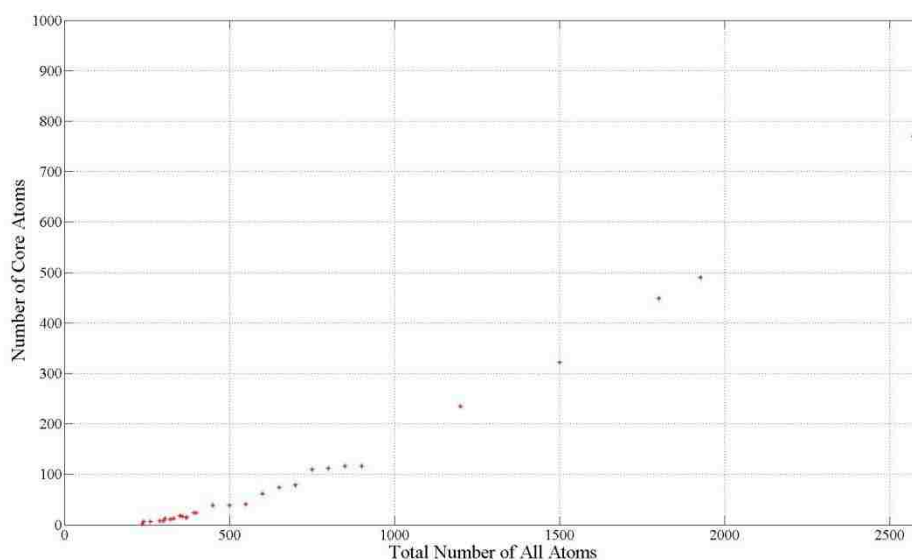


Figure 3.24 Number of Core Atoms versus Total Number of All Atoms in Nanoparticles

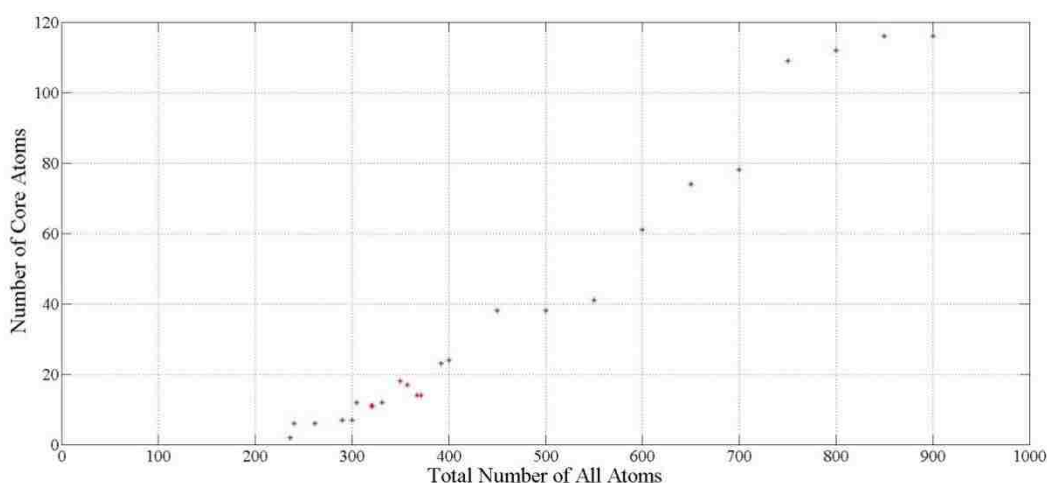


Figure 3.25 Number of Core Atoms versus Total Number of All Atoms in Nanoparticles ($N < 1000$)

Chapter 4 Summary, Conclusion and Future Work

4.1 Summary and Conclusion

In this thesis, the Molecular Dynamics (MD) method was applied to perform atomic scale simulations of bulk (i.e. ideal) single crystal gold (Au), free planar crystalline surfaces of single crystal Au, as well as 33 Au nanoparticles (NPs). The goal of the study was to determine if atomic scale bonding in NPs exhibits lattice compression for sufficiently small NPs. It is expected that surface stress acting on NPs with very high surface area to volume ratio may elastically distort the inner lattice of the NP. For instance, for fluid droplets, it is well accepted that the pressure difference between the inside and outside of the drop is $\Delta P = \frac{2\gamma}{R}$, where γ is the interfacial energy between the fluids and R is the radius of the drop. Thus, very small drops have very large pressure differences. For a solid, an analogous situation is expected, however, γ is replaced by f , the surface stress, which for solids is distinct from the surface energy. Surface stress measures the energy change associated with elastically deforming the solid surface (i.e. no addition/subtraction of atoms at the surface) while surface energy measures the energy change associated with the creation/annihilation of undeformed free surface (i.e. by adding/subtracting atoms at the surface). Despite this difference, an analogous situation is anticipated where a pressure difference exists between the inside and outside of a solid spherical particle. The goal of this study was to see if atomic bonding, as revealed by MD simulation, correlates properly with a pressure change as predicted by $P = 2 f / R_{NP}$.

When modeling at the atomic scale, it is of great importance to choose an appropriate description of the system potential energy, that is, an appropriate model of the interaction energy between atoms of the system. Since studies here focused on a single metal, i.e. gold, the embedded atom method (EAM) style of interaction was adopted. The EAM is widely used to describe the interaction between metallic atoms and we used a pre-existing EAM potential for Au in all our simulations.

From the planar crystalline surface simulations, the surface stress of three low index crystal surfaces was determined for the model of Au utilized. Surface stresses were analyzed in two ways: by computing the thermodynamic quantity using all atoms in the simulation and by considering contributions from individual atoms as a function of the atom's distance from the free surface. Using results from the bulk crystalline simulation, we calculated the atomic scale pair distribution function $G(r)$ for an ideal Au lattice. To evaluate changes in atomic bonding environment for nanoparticles compared to a bulk crystal, $G(r)$ was also computed for all NPs simulated.

In the surface calculations, we derive an important conclusion that at equilibrium state, the values of surface stress for three different orientations are all in the range of $1.3\sim 2.0 J/m^2$. Moreover, analysis of stress contributions on a per atom basis showed that surface stress manifests only in those atoms within 7 to 8 Å of the free surface. $G(r)$ analysis on the NPs showed that the position of the first peak in $G(r)$ shifted to smaller r for smaller NPs. This was taken as evidence that a compressive stress was acting to compress nearest neighbor bond lengths. This bond compression was

interpreted as lattice compression and separate simulations of bulk Au at varying lattice constant revealed the corresponding internal pressure. However, when this computation of internal pressure was plotted versus $1/R_{NP}$, the resulting prediction of surface stress f was nearly four times the values obtained from planar surface calculations.

With the notion that the surface stress influences atoms to a depth of about 7 to 8 Å below a planar crystal surface, we could define the atoms located within a sphere whose radius is $(R_{NP}-7 \text{ Å})$ as the core atoms of a NP. In order to show surface effect more clearly, the entire analysis procedure was applied to only the core atoms of each NP, including $G(r)$ calculation, first peak position analysis, and fitting for stress value. The features of $G(r)$ of core atoms were quite similar to what was computed for all atoms in the NP, including the first peak shift. However, it was found that the magnitude of the first $G(r)$ peak shift was less when core atoms alone were considered. This phenomenon was attributed to the fact that surface atoms have less bonding neighbors than core atoms; as a result, they contract their nearest neighbor bond lengths. It is known that the proportion of surface atoms increases as R_{NP} gets smaller, so the first peak position of $G(r)$ tends to smaller value as the size of NP decreases partly due to surface atom bond contraction and partly due to core atom bond compression. Furthermore, the prediction of surface stress using only core atoms in the analysis yielded a result very close to the values given by the planar free surface simulation. This gives evidence that the surface stress was some linear combination of surface stress values of different low index surfaces. Nonetheless, statistical variations

were large enough to prevent us from concluding whether or not the thermodynamic surface stress values change for small enough NPs. Lastly, we also considered the number of core atoms versus R_{NP} , which showed that for sufficiently small NPs, the definition of core atoms is questionable.

4.2 Future Work

Since there are many options in the MD simulation setting, other promising ways to simulate the system can be chosen for this project. For instance, it's possible to alter the thermal equilibration stage as it can be interesting to see whether the results are sensitive to the initial condition of the system or not. We have operated additional simulations in which there is no initial 100ps NVT simulation for several small nanoparticles. It is found in most cases that the radial density profile and the $G(r)$ remain the same. However, more work should be done to clarify the relationship. Meanwhile, some further efforts should be made to establish a more rigorous approach to determine the first peak position to avoid or diminish the significant scatter of those line fitting data, i.e. reduce statistical variation. Besides, NPs formed by some other metal materials like copper (Cu) and platinum (Pt) may be analyzed by the methods developed in this thesis to investigate their structural properties. This is also true for NPs composed of some non-metal material like silicon.

Moreover, some other property associated with surface effect can be computed and analyzed. Vibrational density of states (VDOS) is an appropriate option for this

purpose. Inside nanoparticle, VDOS can be considered as that of the corresponding bulk compressed by capillary pressure. R. Meyer et al. (2003) have found that the VDOS shows a significant enhancement at low energies on the surface of nanoparticles and even exhibits a similar structure to that of bulk surface. [40] It is also derived that the VDOS of nanoparticles is controlled by the high percentage of surface atom and the existence of homogeneous capillary pressure. By this simulation and analysis, the effect of surface stress might be able to be understood and demonstrated more deeply.

Appendix A

The following are the radial density profiles and the plots of pair distribution function $G(r)$ for all the nanoparticles which are not illustrated in Chapter 3

There are 28 sets of figures illustrated here, which correspond to 28 gold nanoparticles.

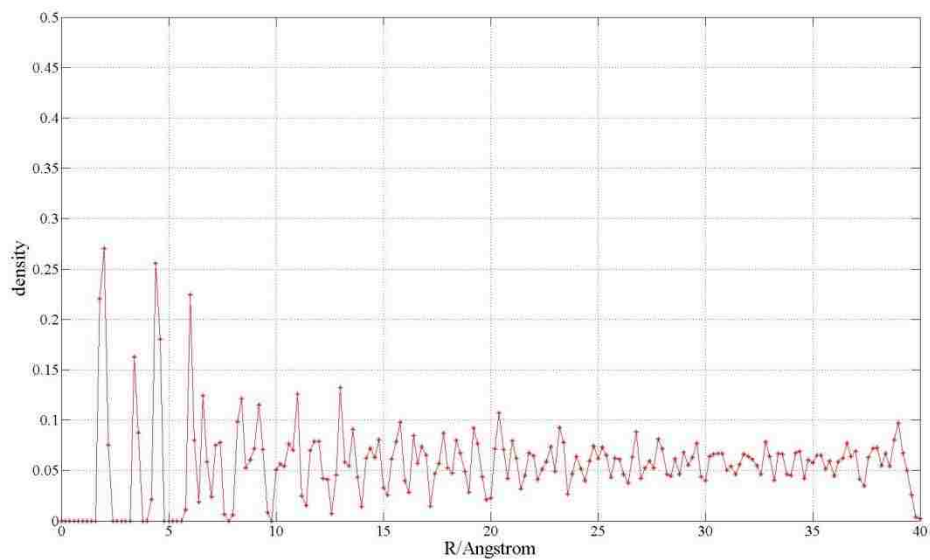


Figure AA.1 Radial Density Profile of $R_{NP}=39.6 \text{ \AA}$ Au Nanoparticle

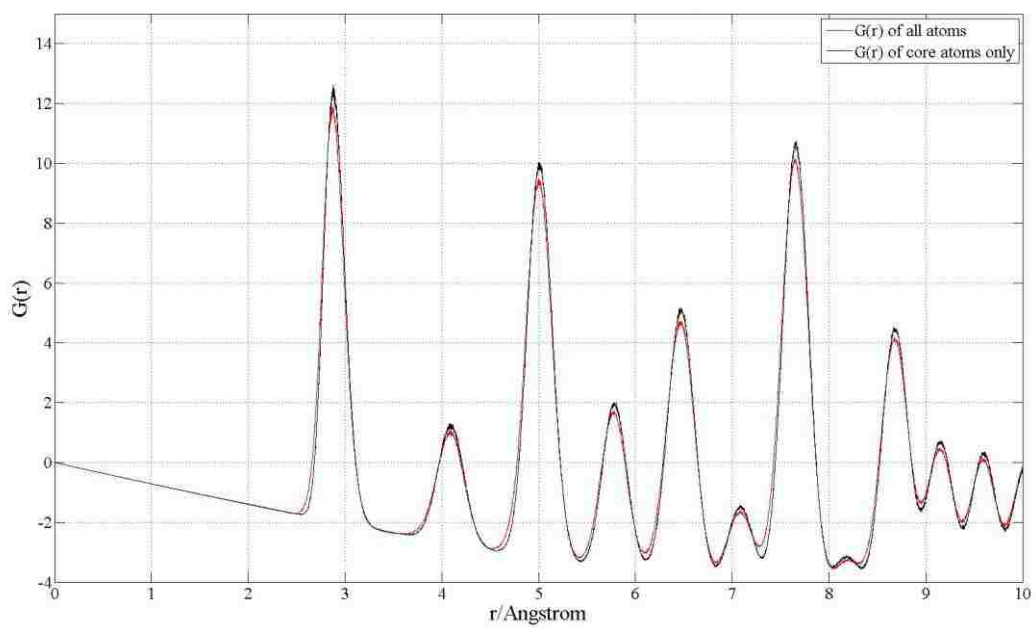


Figure AA.2 Pair Distribution Function of $R_{NP}=39.6 \text{ \AA}$ Au Nanoparticle

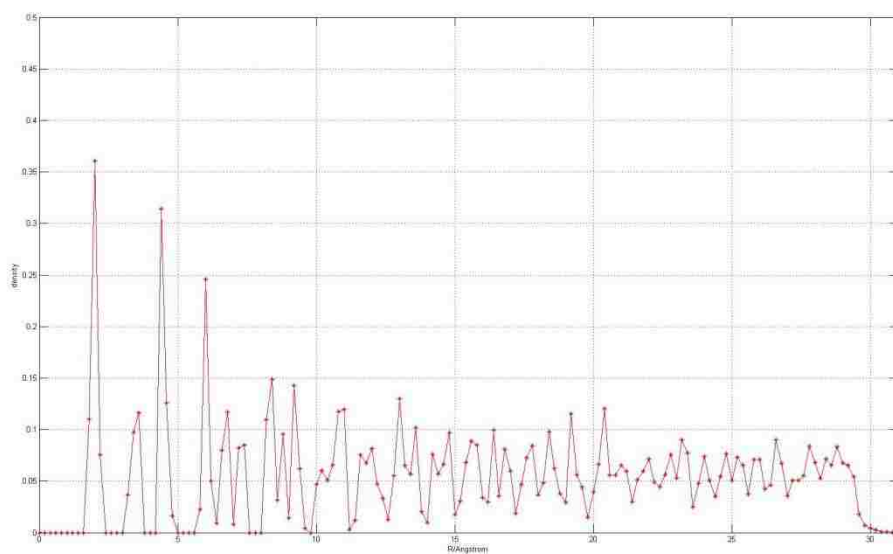


Figure AA.3 Radial Density Profile of $R_{NP}=29.6 \text{ \AA}$ Au Nanoparticle

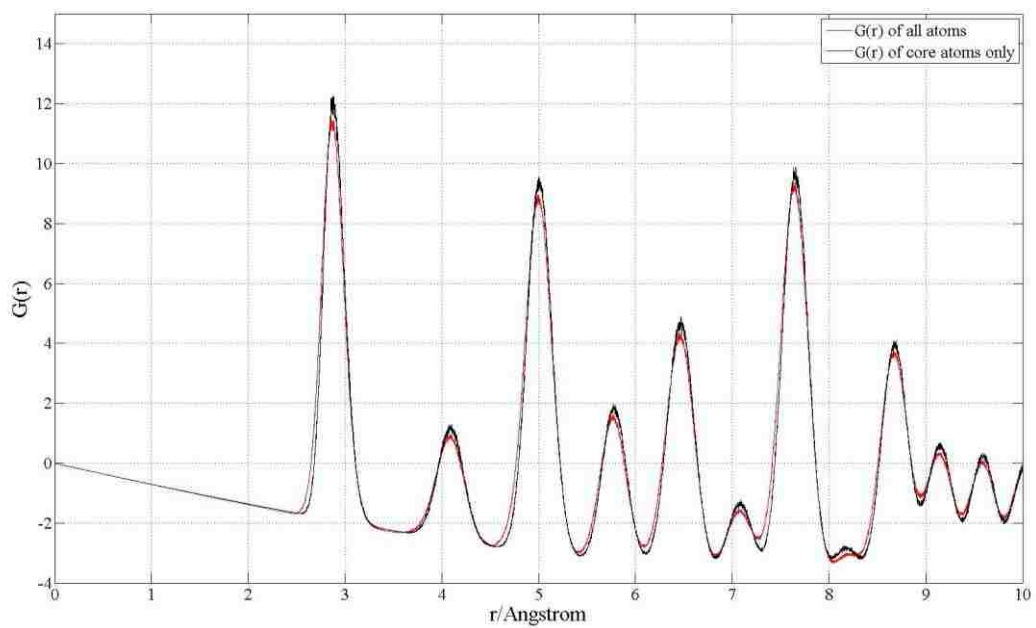


Figure AA.4 Pair Distribution Function of $R_{NP}=29.6 \text{ \AA}$ Au Nanoparticle

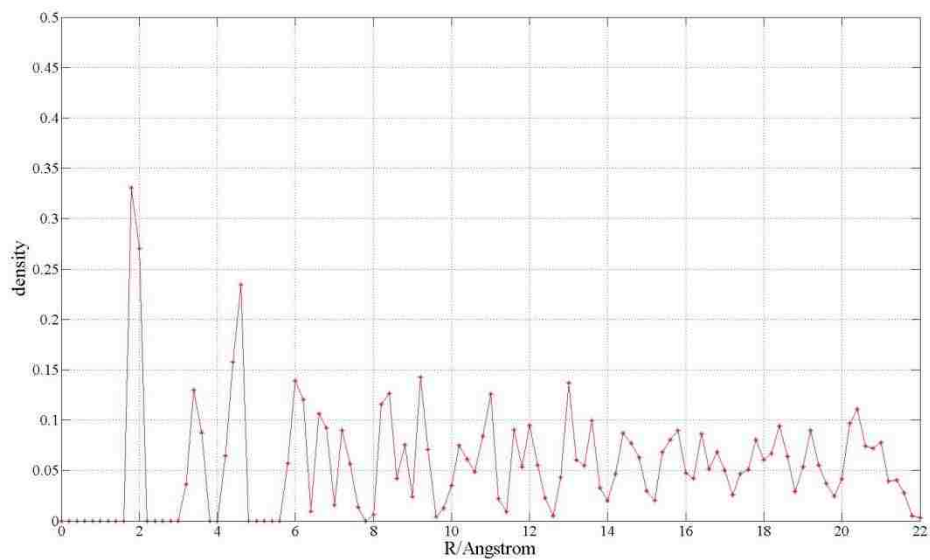


Figure AA.5 Radial Density Profile of $R_{NP}=21.6 \text{ \AA}$ Au Nanoparticle

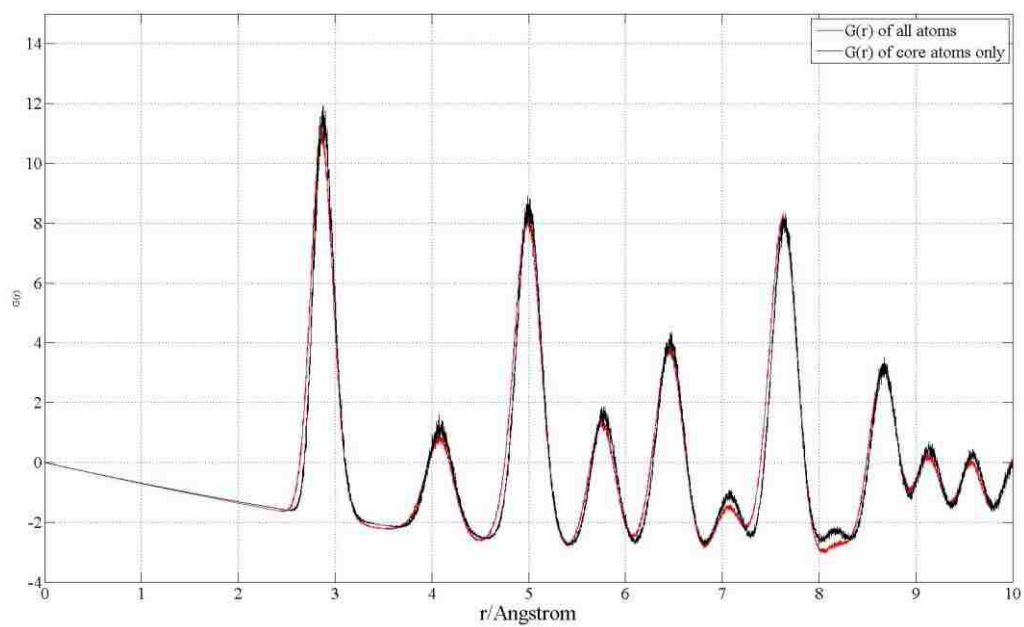


Figure AA.6 Pair Distribution Function of $R_{NP}=21.6 \text{ \AA}$ Au Nanoparticle

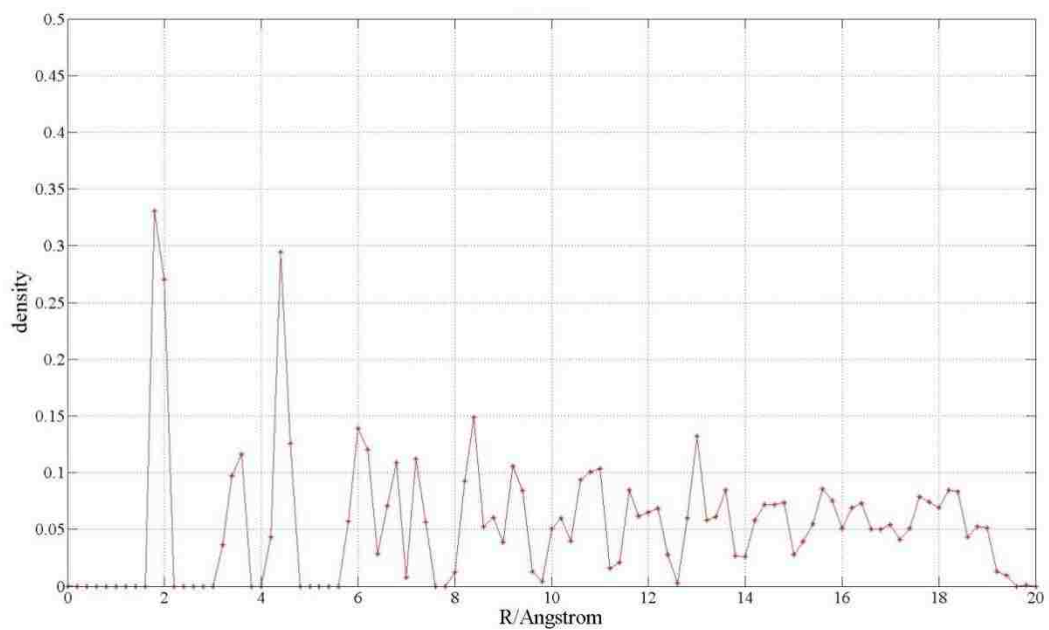


Figure AA.7 Radial Density Profile of N=1800 ($R_{NP}=19.1 \text{ \AA}$) Au Nanoparticle

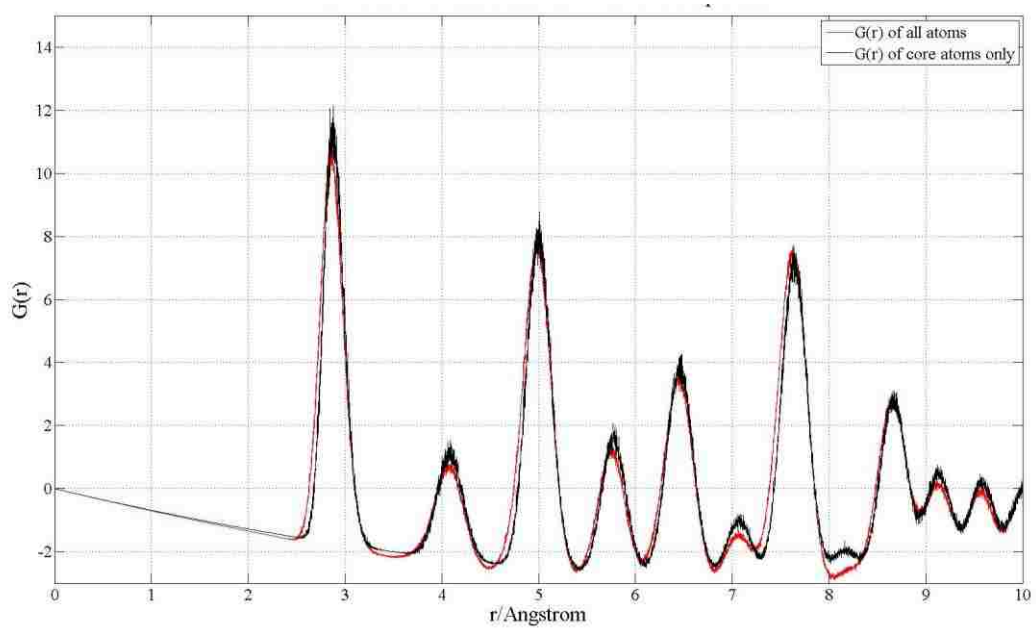


Figure AA.8 Pair Distribution Function of N=1800 ($R_{NP}=19.1 \text{ \AA}$) Au Nanoparticle

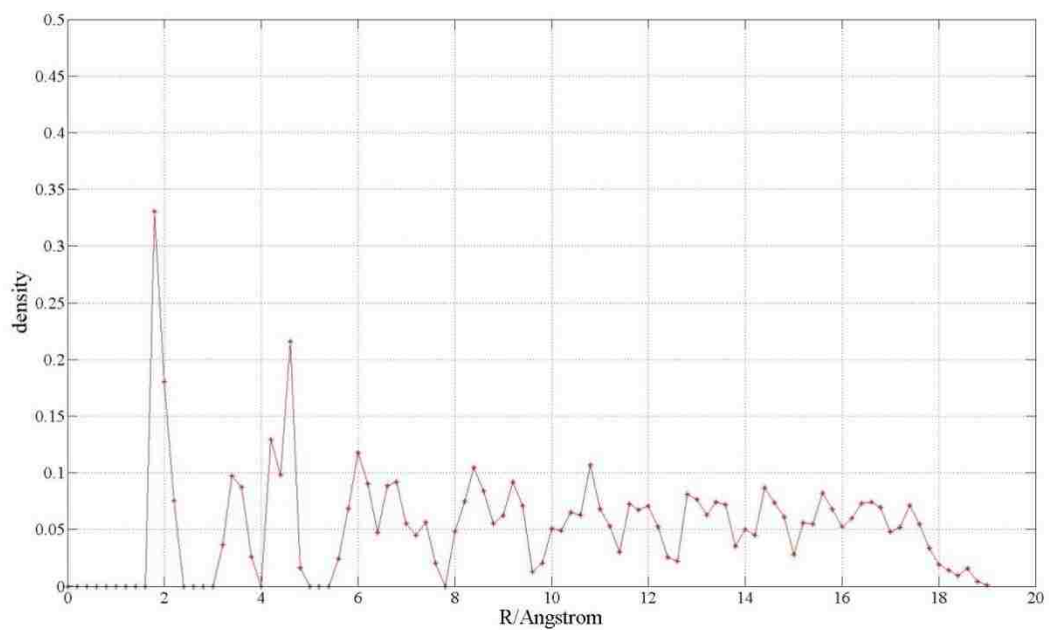


Figure AA.9 Radial Density Profile of N=1500 ($R_{NP}=17.9 \text{ \AA}$) Au Nanoparticle

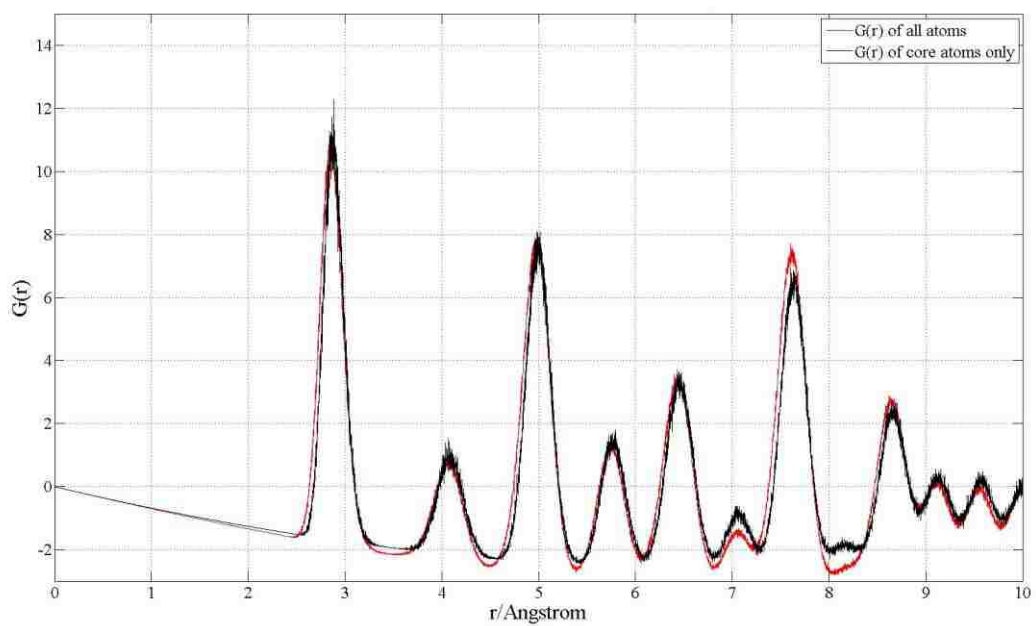


Figure AA.10 Pair Distribution Function of N=1500 ($R_{NP}=17.9 \text{ \AA}$) Au Nanoparticle

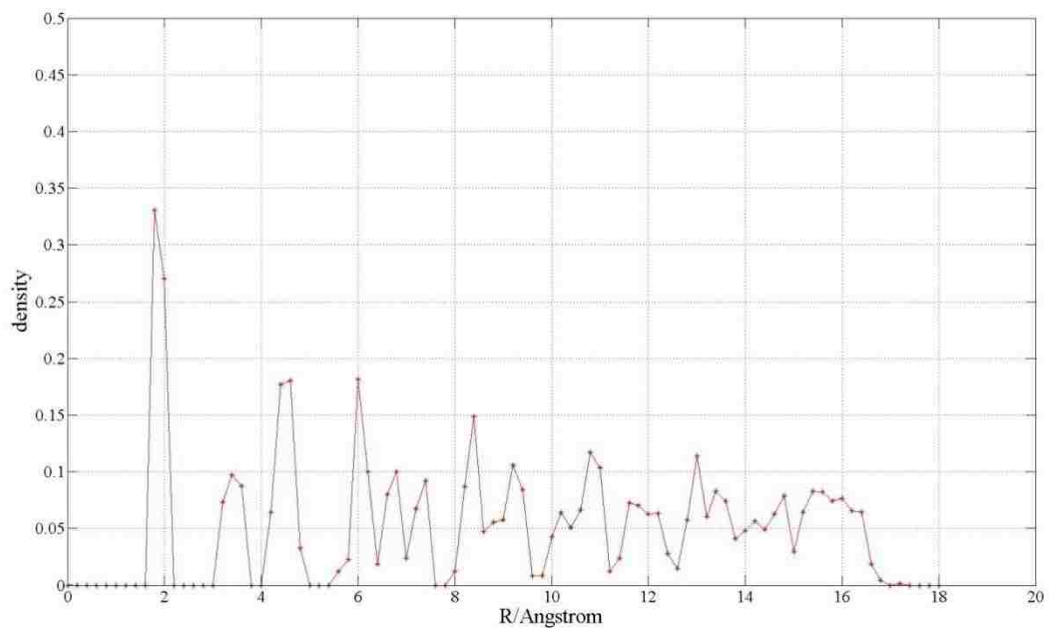


Figure AA.11 Radial Density Profile of N=1200 ($R_{NP}=16.6 \text{ \AA}$) Au Nanoparticle

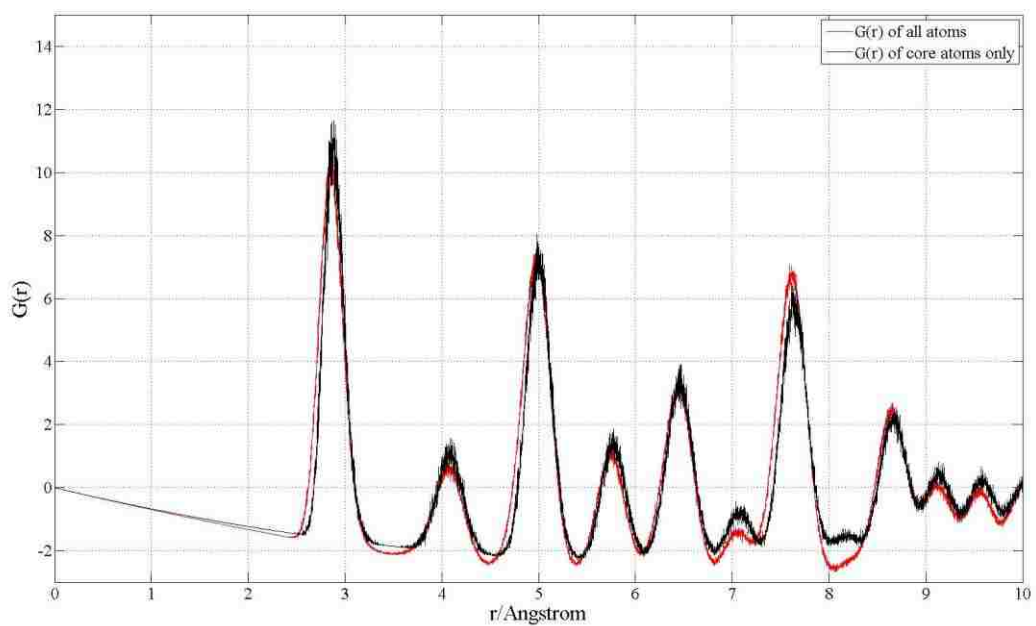


Figure AA.12 Pair Distribution Function of N=1200 ($R_{NP}=16.6 \text{ \AA}$) Au Nanoparticle

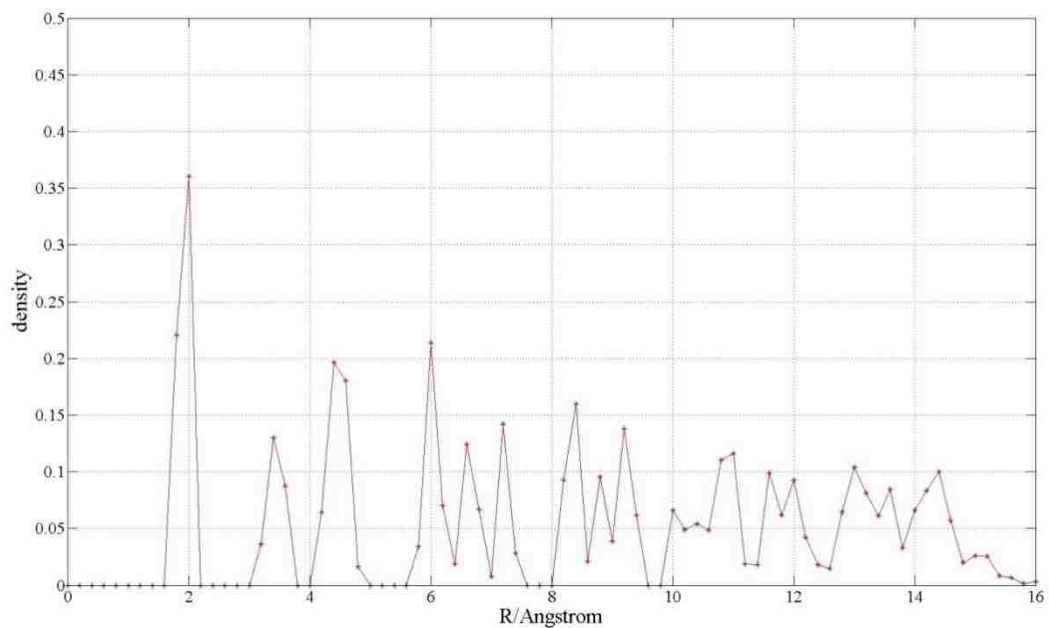


Figure AA.13 Radial Density Profile of N=900 ($R_{NP}=14.8 \text{ \AA}$) Au Nanoparticle

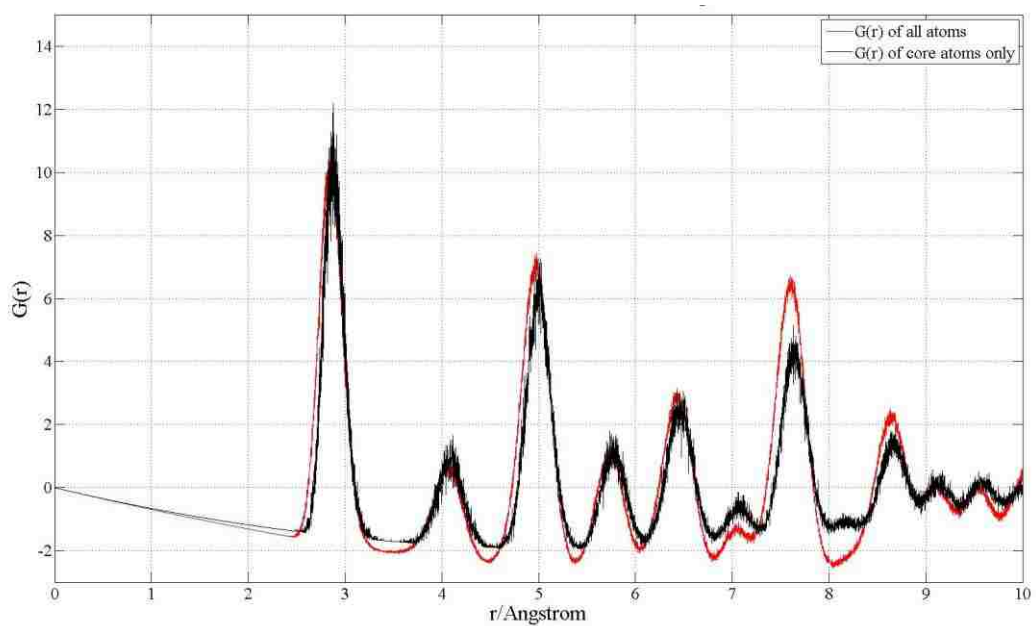


Figure AA.14 Pair Distribution Function of N=900 ($R_{NP}=14.8 \text{ \AA}$) Au Nanoparticle

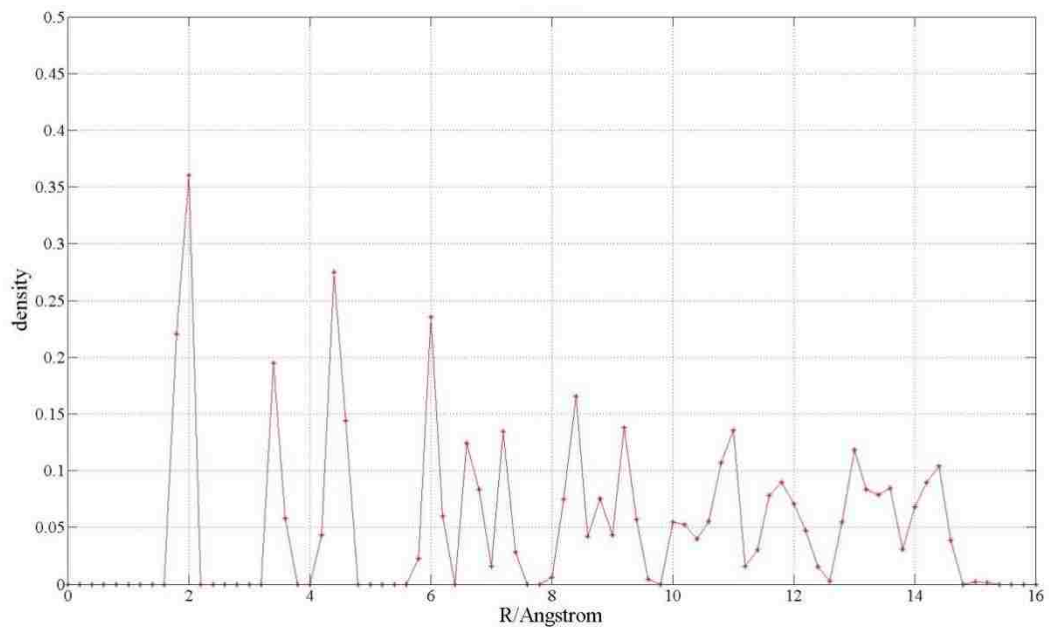


Figure AA.15 Radial Density Profile of N=850 ($R_{NP}=14.7 \text{ \AA}$) Au Nanoparticle

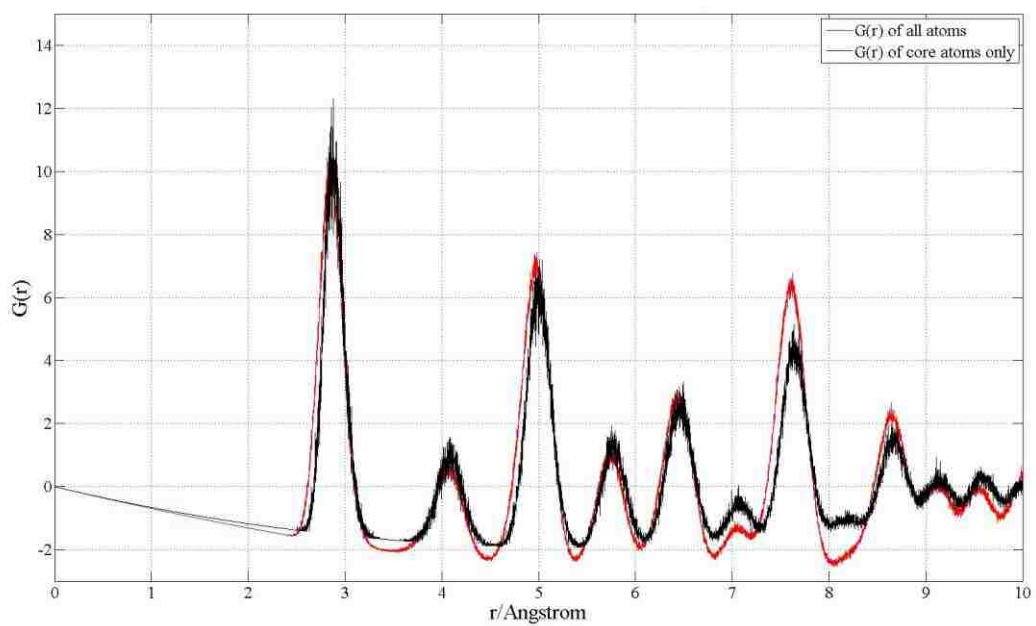


Figure AA.16 Pair Distribution Function of N=850 ($R_{NP}=14.7 \text{ \AA}$) Au Nanoparticle

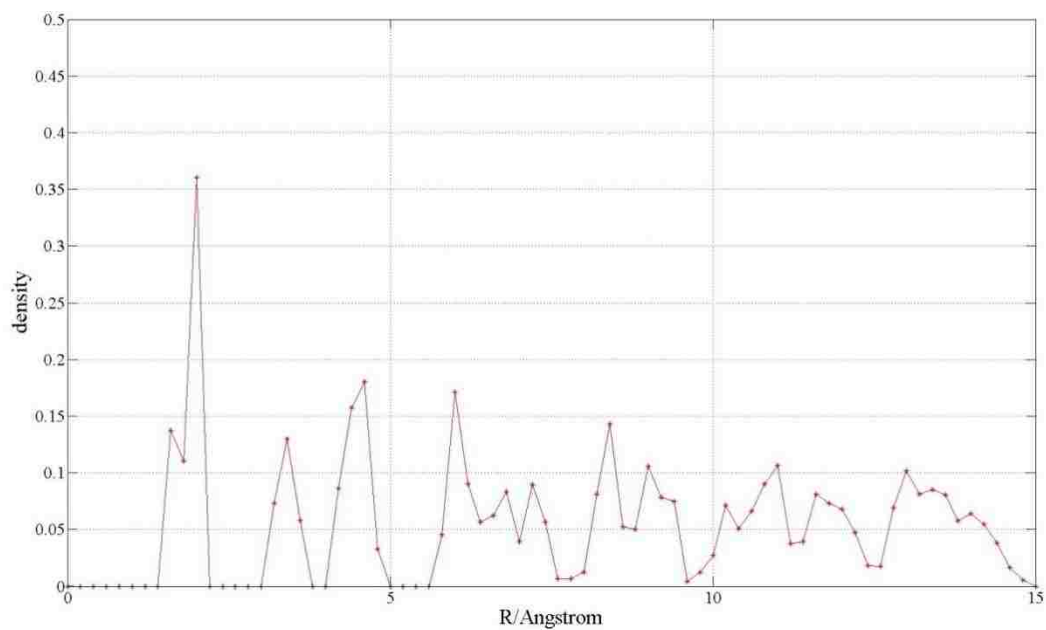


Figure AA.17 Radial Density Profile of N=800 ($R_{NP}=14.5 \text{ \AA}$) Au Nanoparticle

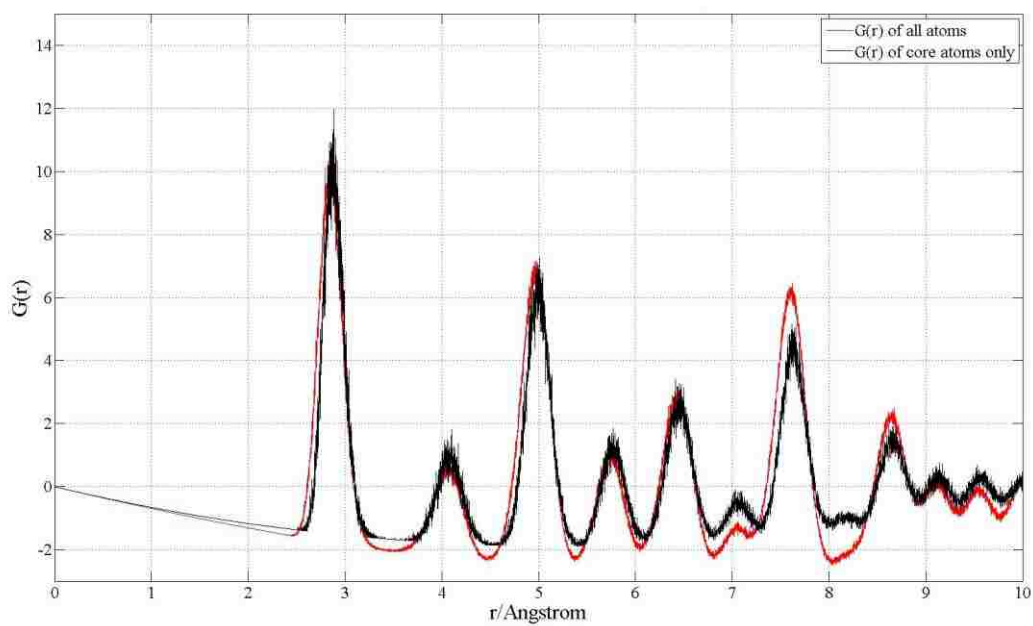


Figure AA.18 Pair Distribution Function of N=800 ($R_{NP}=14.5 \text{ \AA}$) Au Nanoparticle

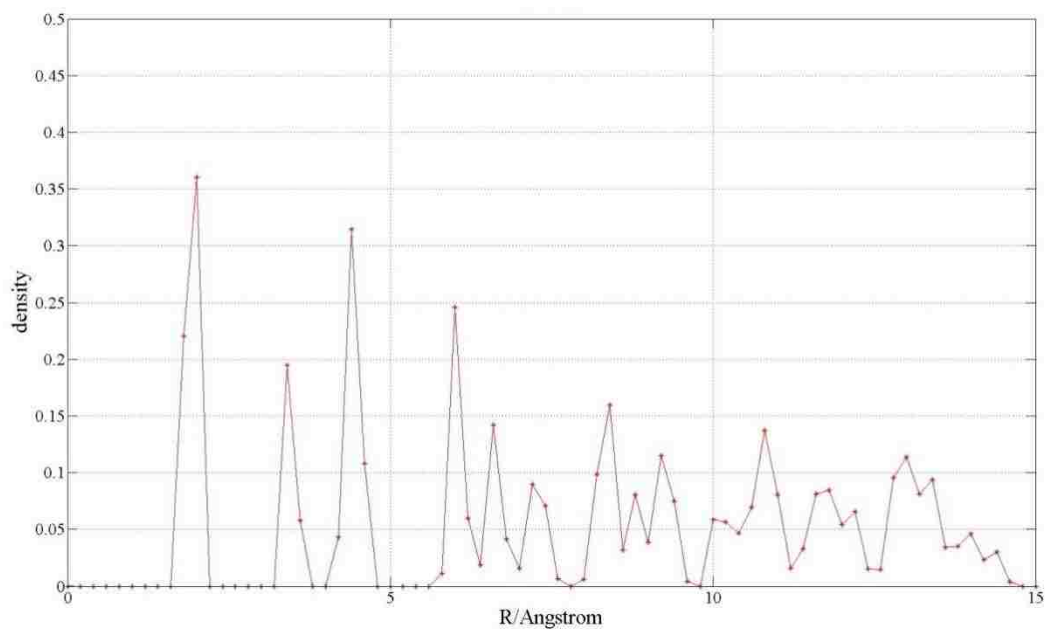


Figure AA.19 Radial Density Profile of N=750 ($R_{NP}=14.4 \text{ \AA}$) Au Nanoparticle

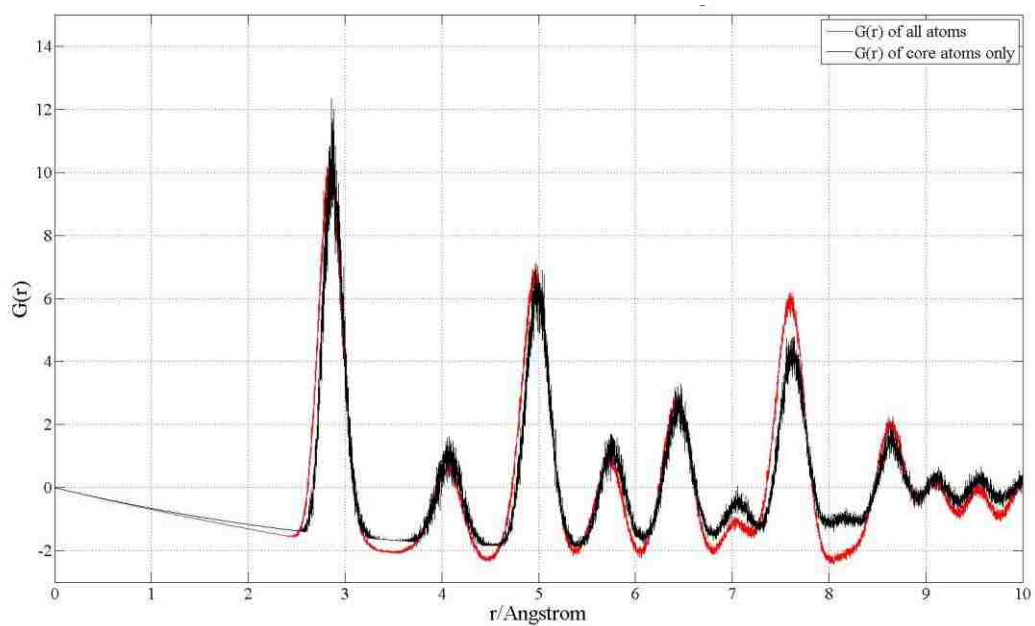


Figure AA.20 Pair Distribution Function of N=750 ($R_{NP}=14.4 \text{ \AA}$) Au Nanoparticle

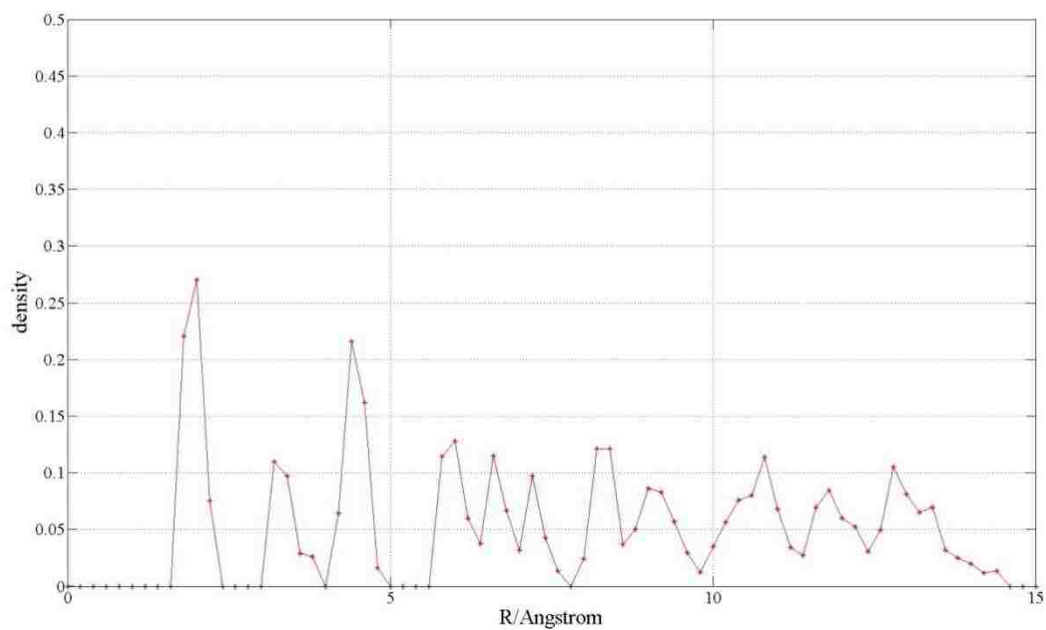


Figure AA.21 Radial Density Profile of N=700 ($R_{NP}=13.7 \text{ \AA}$) Au Nanoparticle

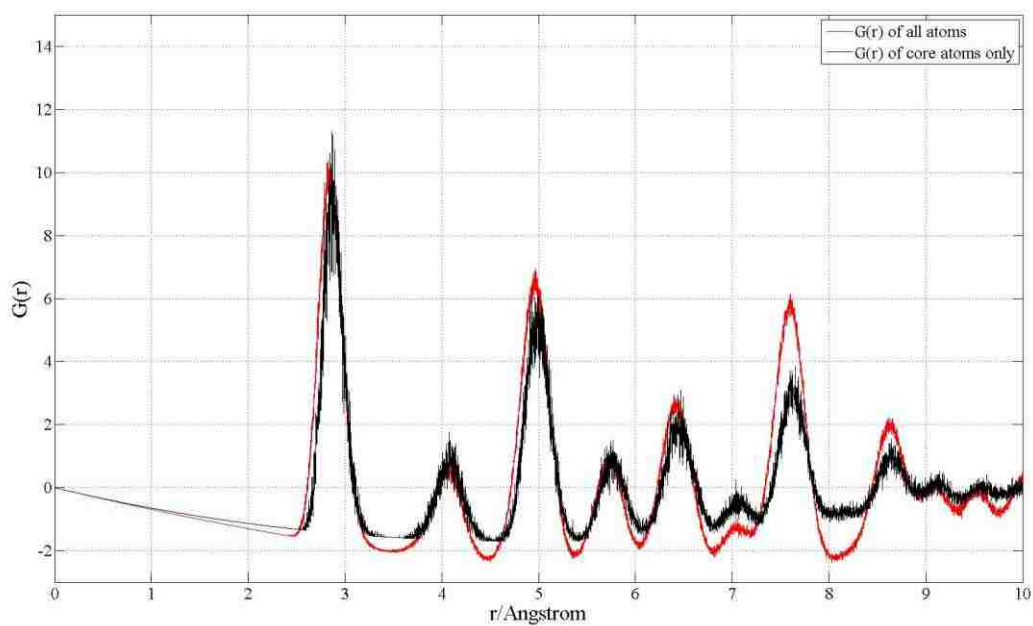


Figure AA.22 Pair Distribution Function of N=700 ($R_{NP}=13.7 \text{ \AA}$) Au Nanoparticle

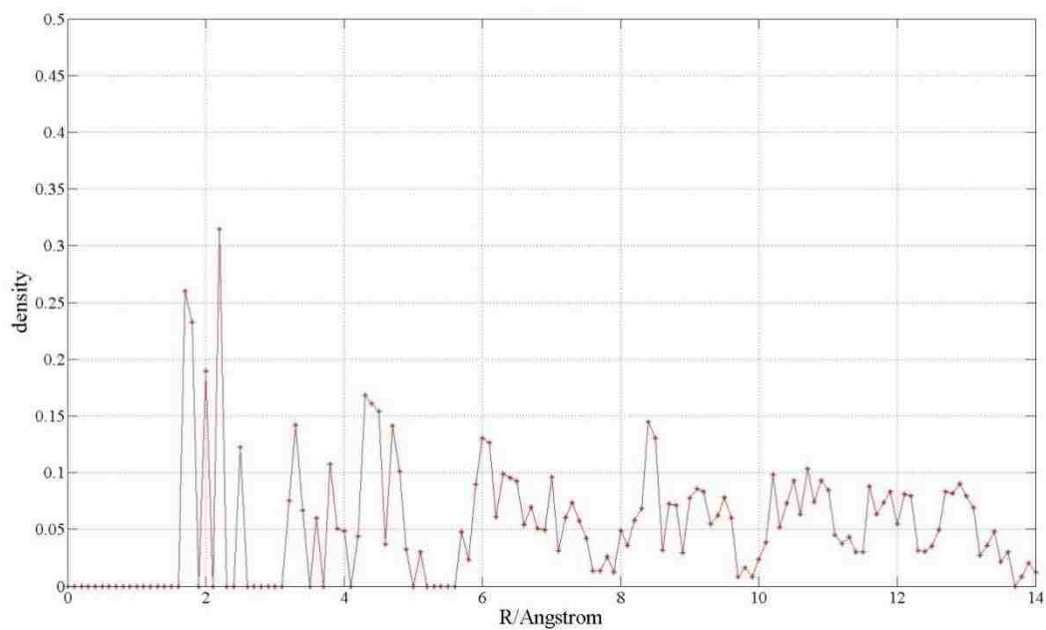


Figure AA.23 Radial Density Profile of N=650 ($R_{NP}=13.6 \text{ \AA}$) Au Nanoparticle

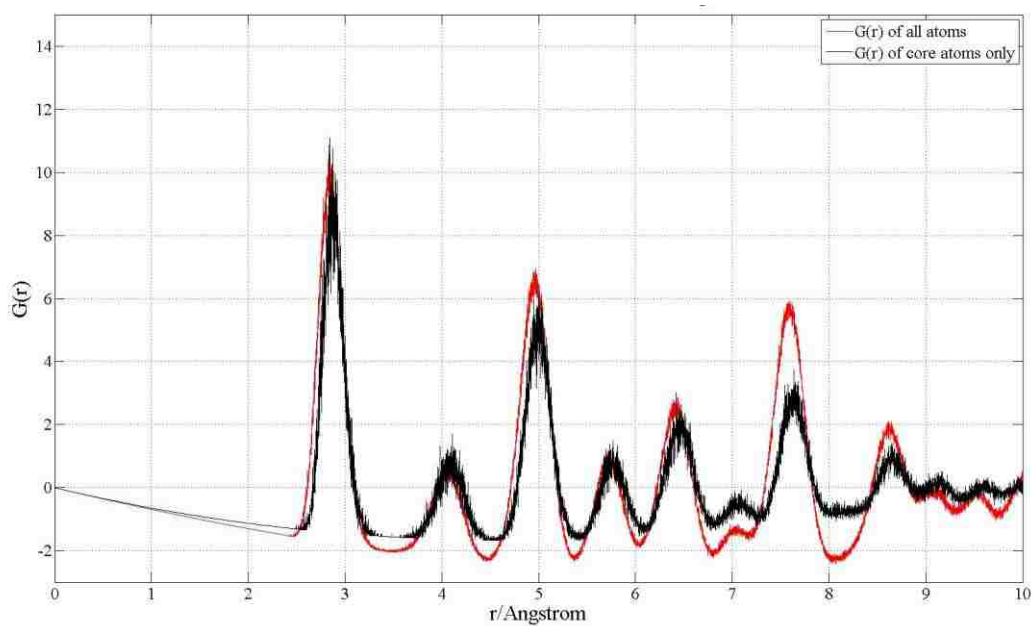


Figure AA.24 Pair Distribution Function of N=650 ($R_{NP}=13.6 \text{ \AA}$) Au Nanoparticle

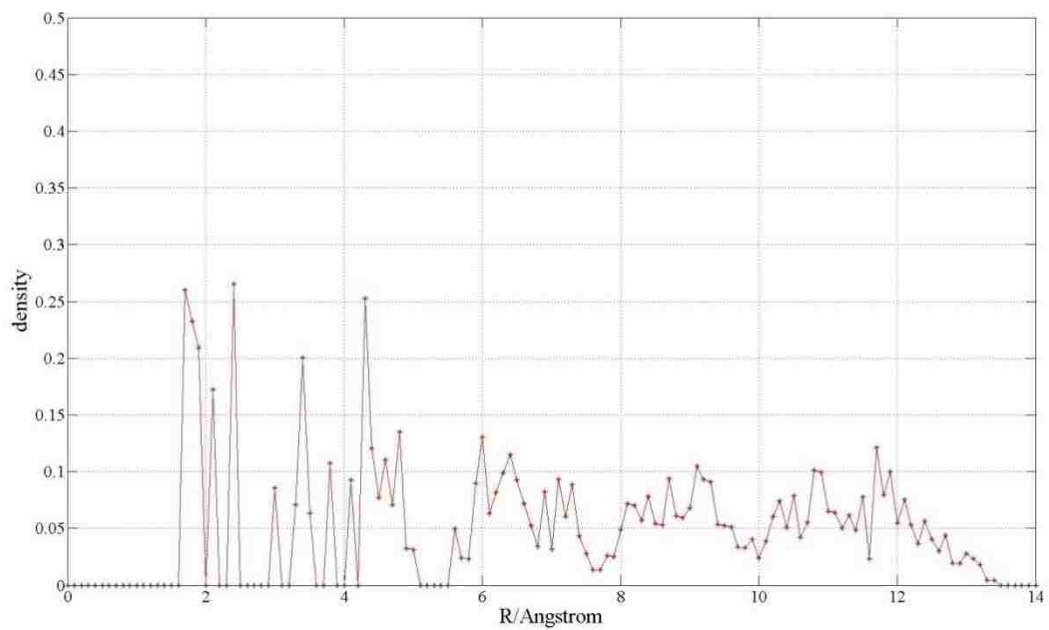


Figure AA.25 Radial Density Profile of N=550 ($R_{NP}=12.8 \text{ \AA}$) Au Nanoparticle

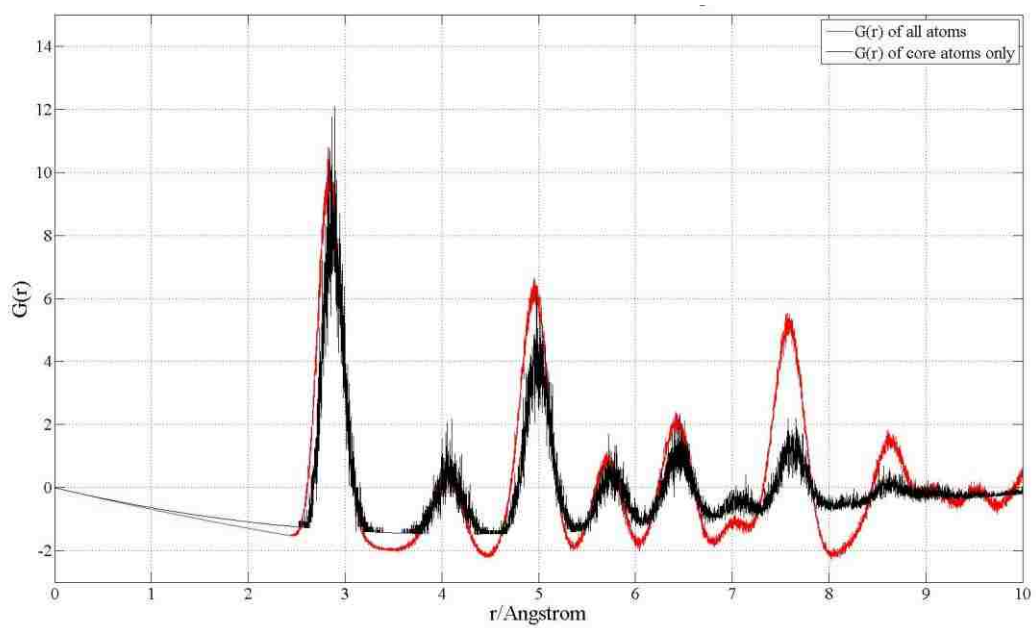


Figure AA.26 Pair Distribution Function of N=550 ($R_{NP}=12.8 \text{ \AA}$) Au Nanoparticle

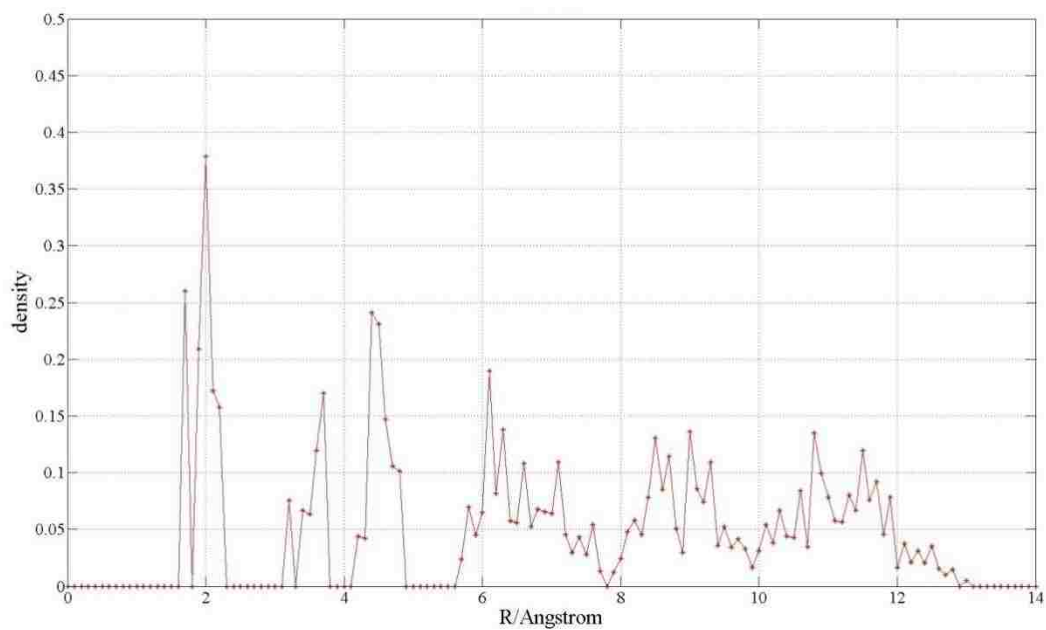


Figure AA.27 Radial Density Profile of N=500 ($R_{NP}=12.5 \text{ \AA}$) Au Nanoparticle

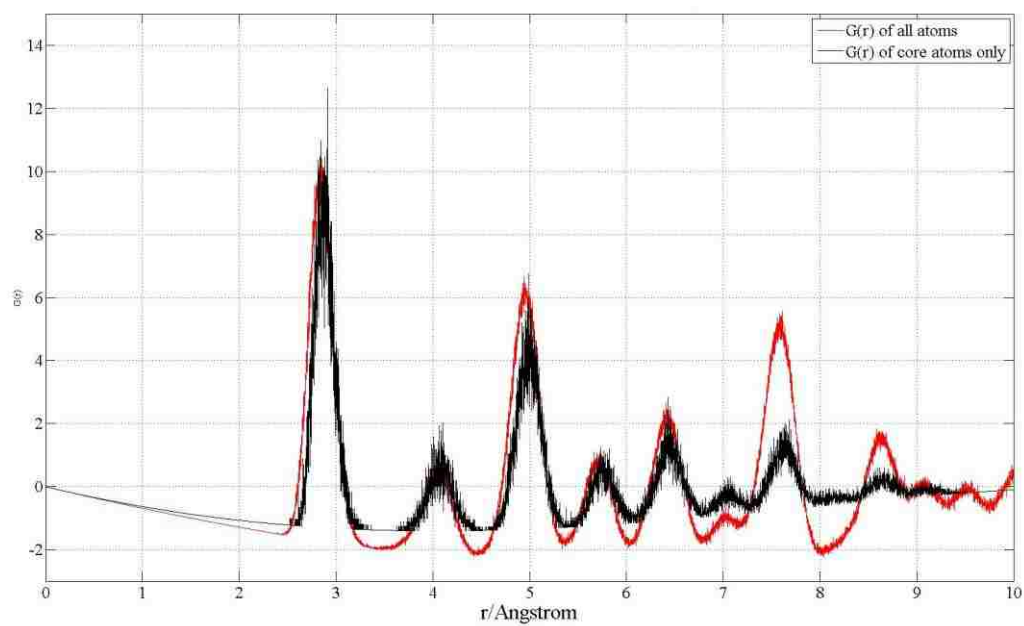


Figure AA.28 Pair Distribution Function of N=500 ($R_{NP}=12.5 \text{ \AA}$) Au Nanoparticle

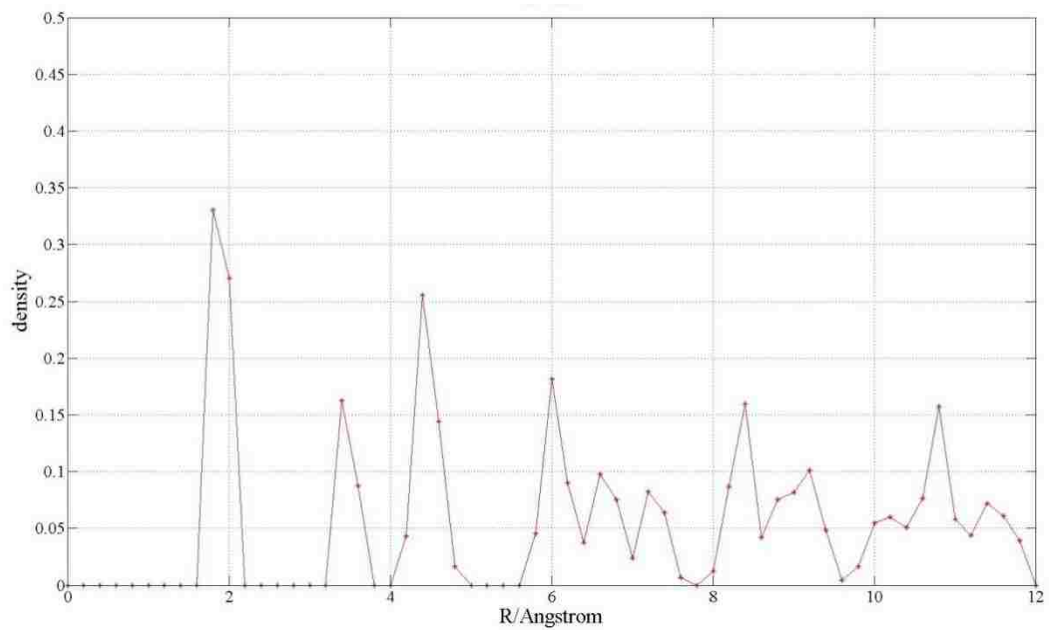


Figure AA.29 Radial Density Profile of N=450 ($R_{NP}=11.8 \text{ \AA}$) Au Nanoparticle

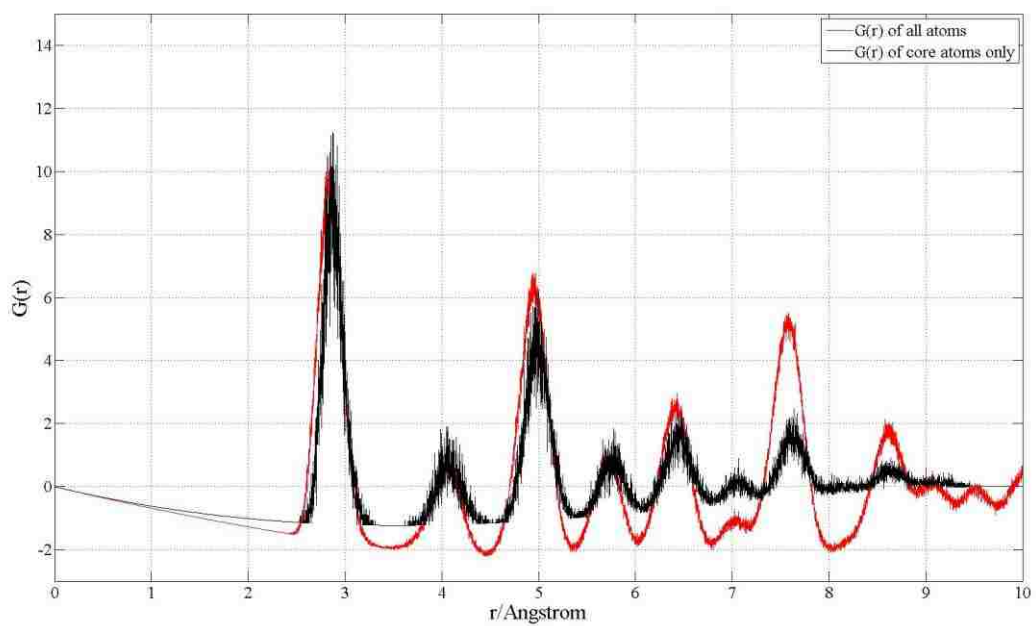


Figure AA.30 Pair Distribution Function of N=450 ($R_{NP}=11.8 \text{ \AA}$) Au Nanoparticle

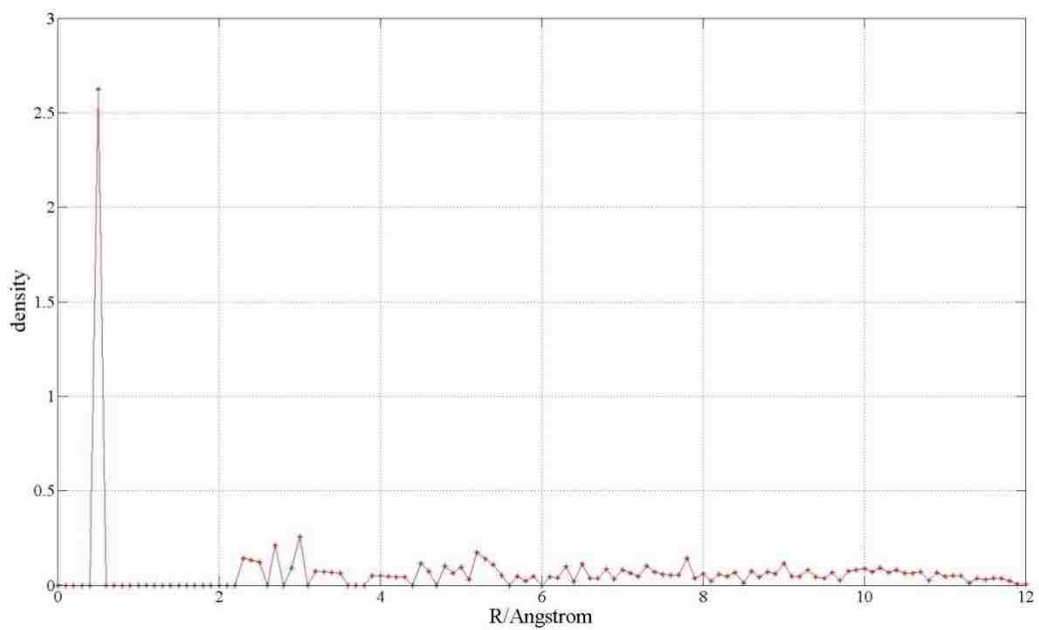


Figure AA.31 Radial Density Profile of N=400 ($R_{NP}=11.7 \text{ \AA}$) Au Nanoparticle

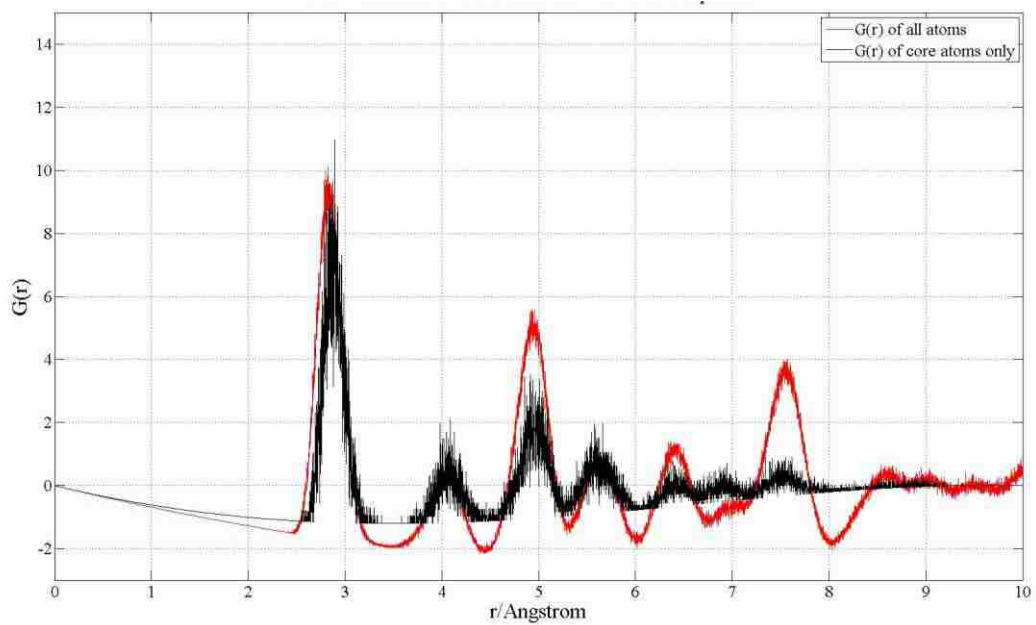


Figure AA.32 Pair Distribution Function of N=400 ($R_{NP}=11.7 \text{ \AA}$) Au Nanoparticle

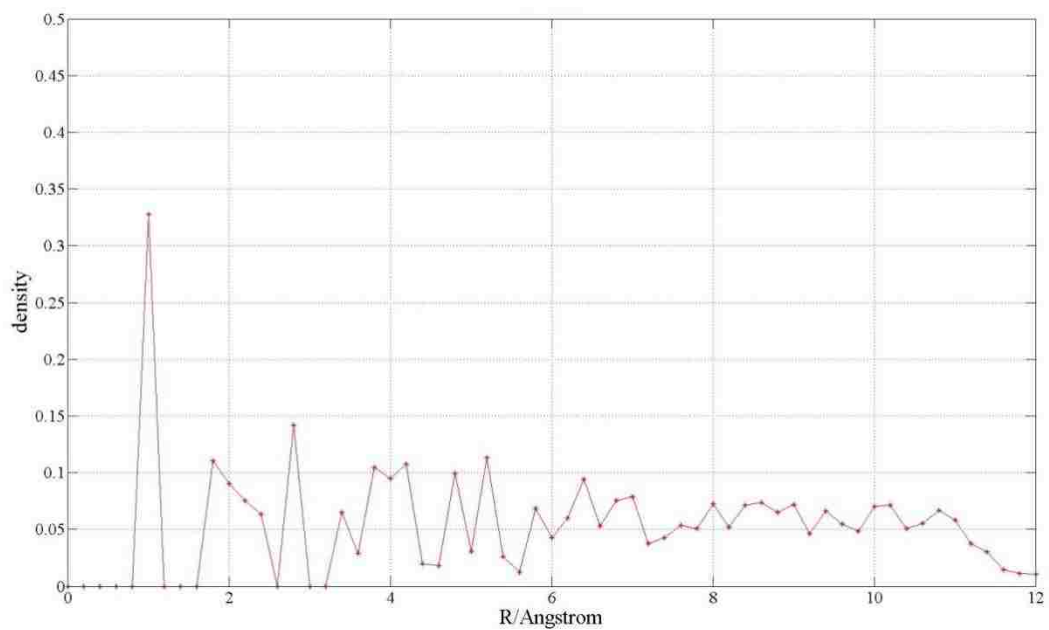


Figure AA.33 Radial Density Profile of N=392 ($R_{NP}=11.4 \text{ \AA}$) Au Nanoparticle

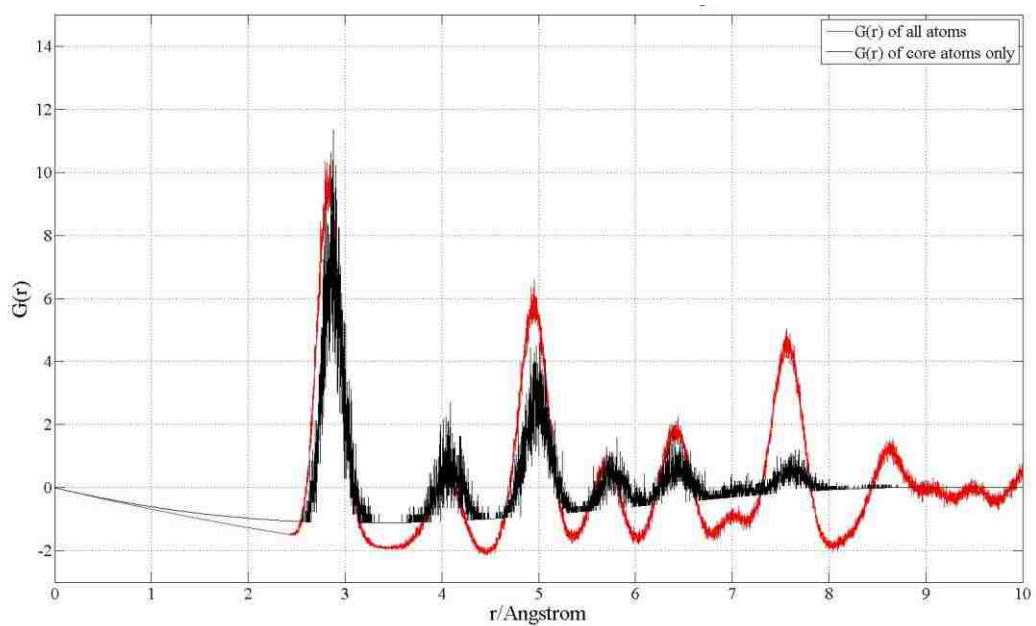


Figure AA.34 Pair Distribution Function of N=392 ($R_{NP}=11.4 \text{ \AA}$) Au Nanoparticle

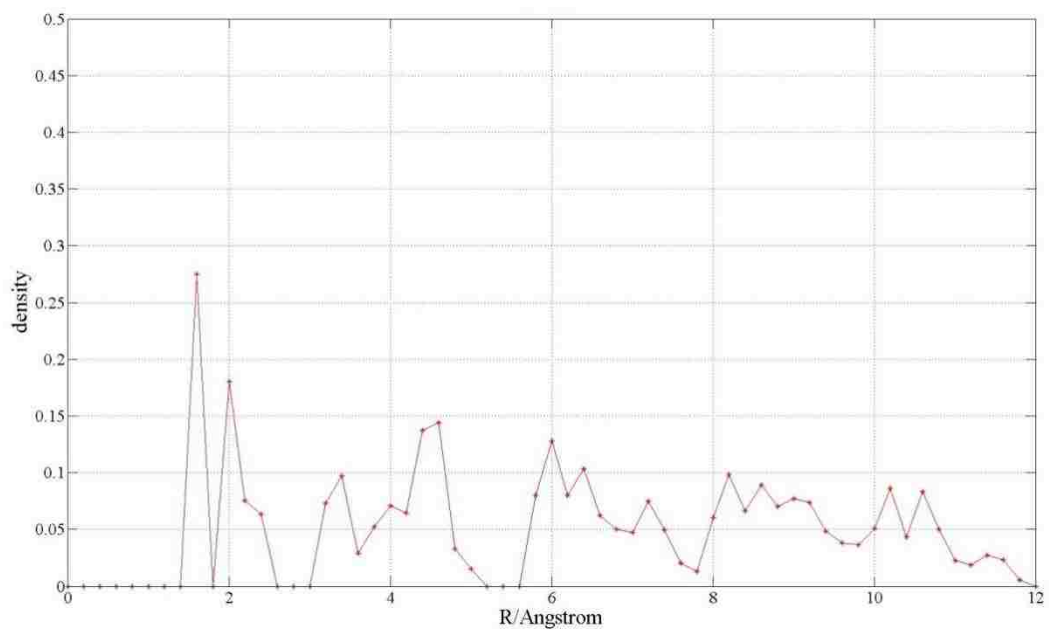


Figure AA.35 Radial Density Profile of N=367 ($R_{NP}=11.0 \text{ \AA}$) Au Nanoparticle

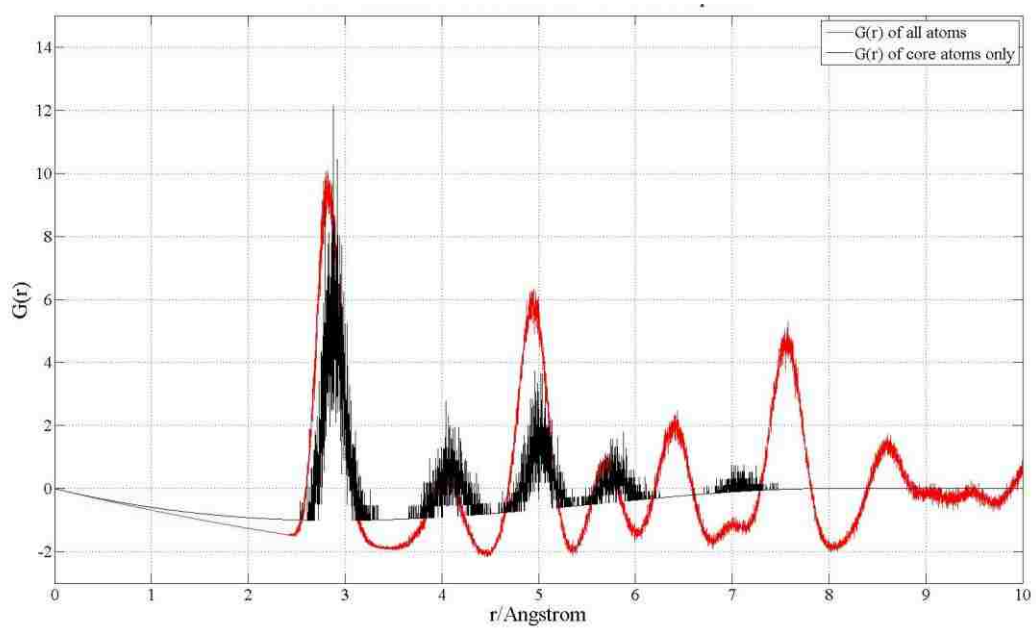


Figure AA.36 Pair Distribution Function of N=367 ($R_{NP}=11.0 \text{ \AA}$) Au Nanoparticle

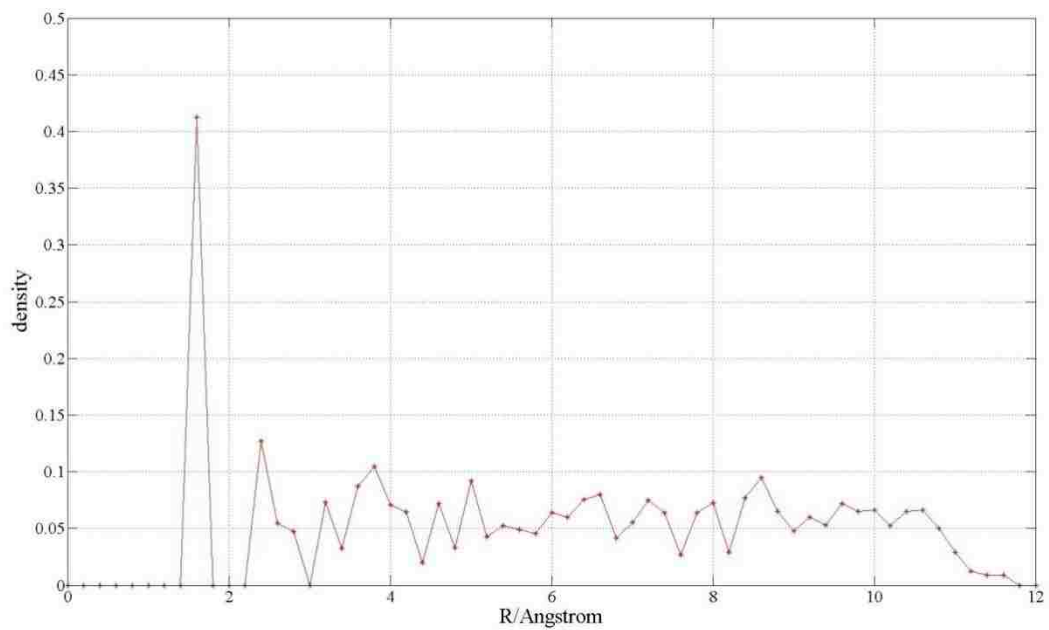


Figure AA.37 Radial Density Profile of $R_{NP}=11.0 \text{ \AA}$ Au Nanoparticle

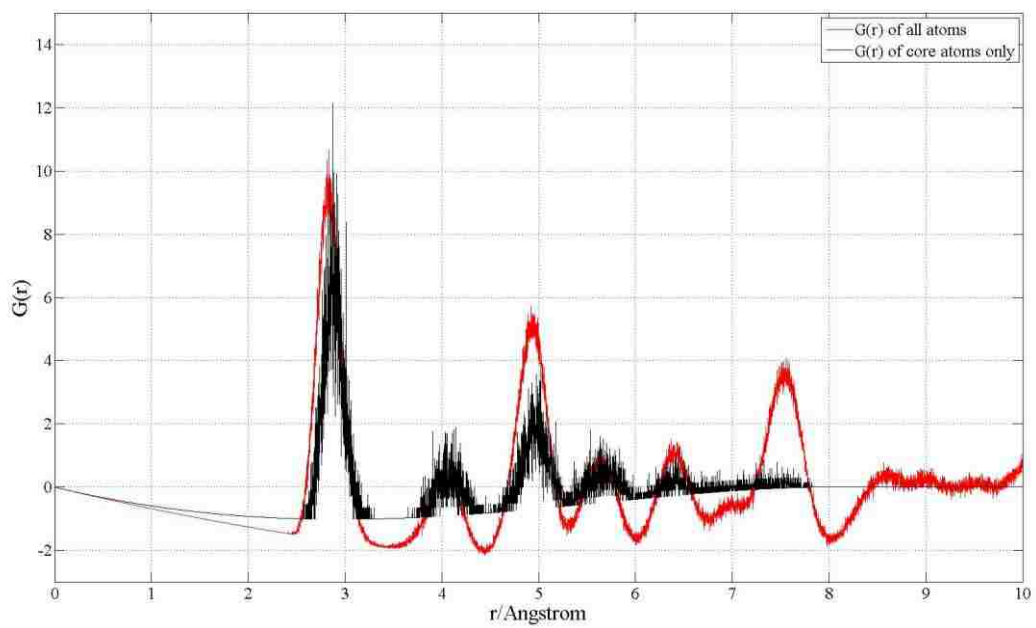


Figure AA.38 Pair Distribution Function of $R_{NP}=11.0 \text{ \AA}$ Au Nanoparticle

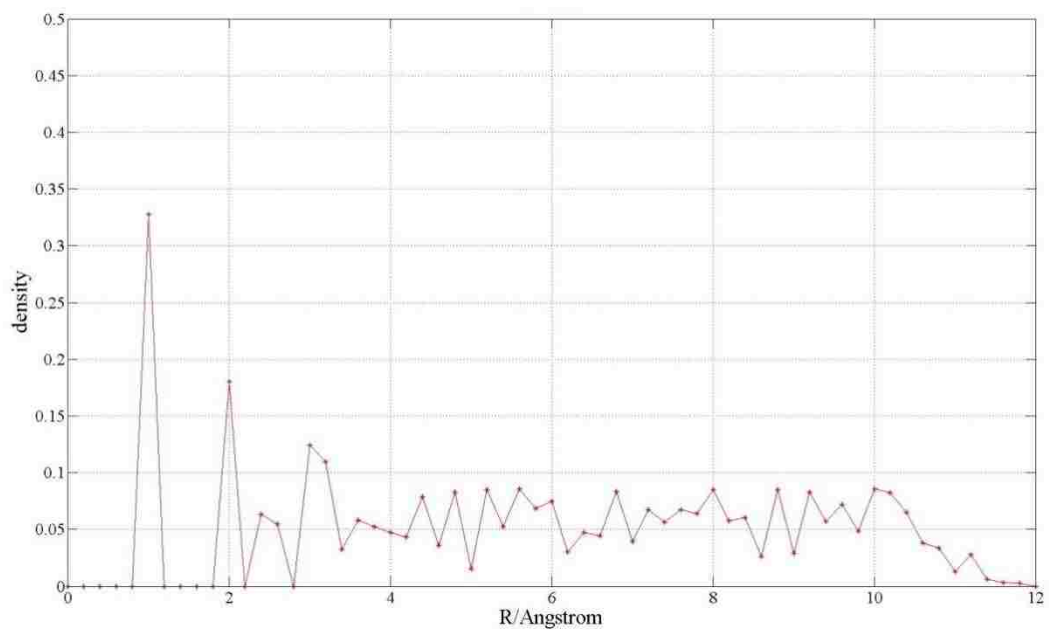


Figure AA.39 Radial Density Profile of N=350 ($R_{NP}=11.0 \text{ \AA}$) Au Nanoparticle

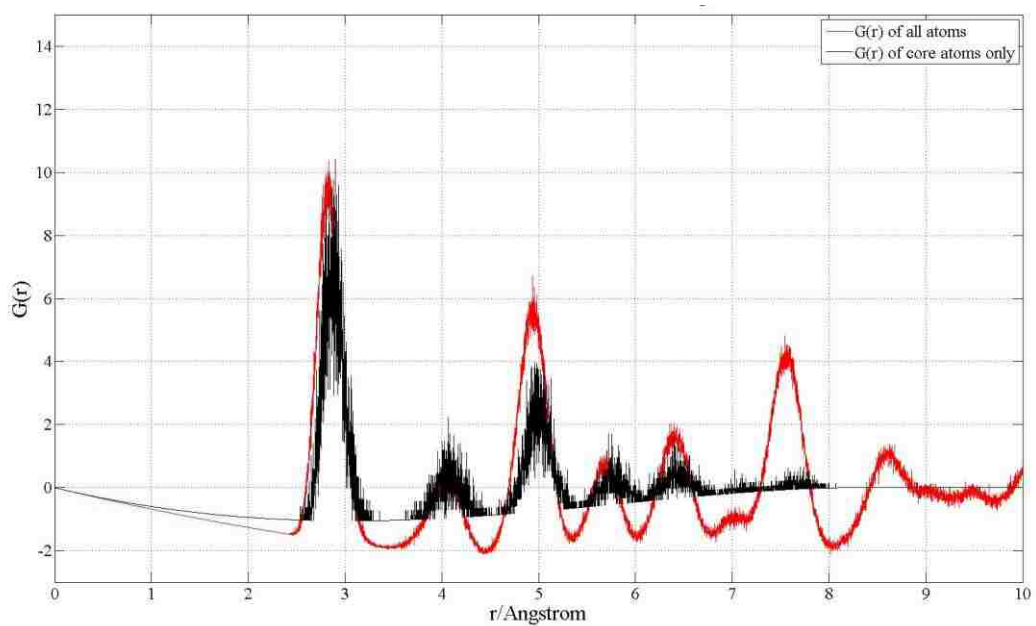


Figure AA.40 Pair Distribution Function of N=350 ($R_{NP}=11.0 \text{ \AA}$) Au Nanoparticle

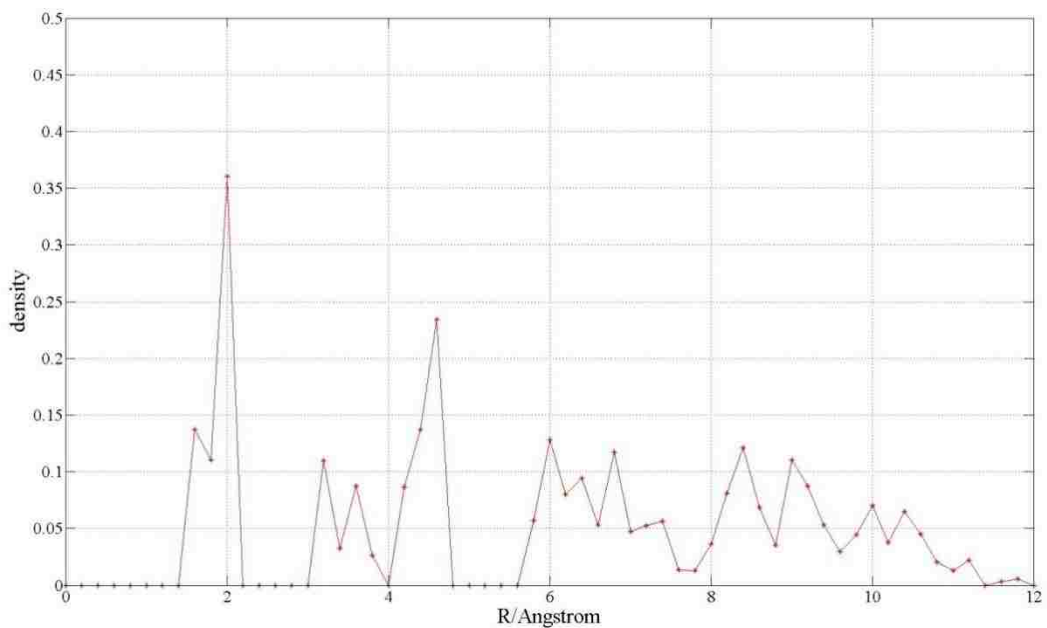


Figure AA.41 Radial Density Profile of N=331 ($R_{NP}=10.8 \text{ \AA}$)Au Nanoparticle

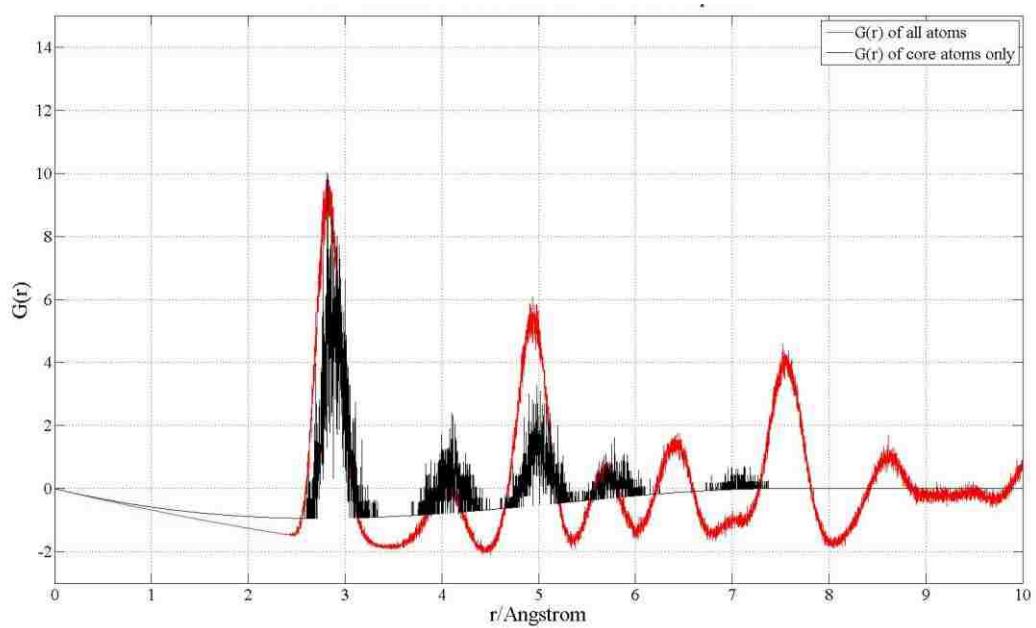


Figure AA.42 Pair Distribution Function of N=331 ($R_{NP}=10.8 \text{ \AA}$)Au Nanoparticle

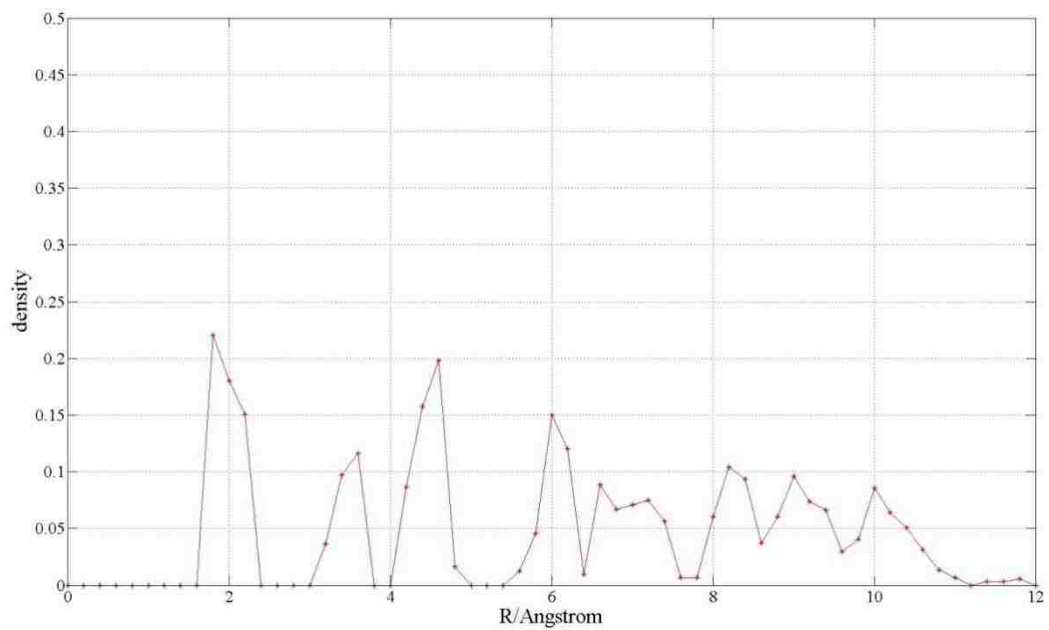


Figure AA.43 Radial Density Profile of N=321 ($R_{NP}=10.7 \text{ \AA}$) Au Nanoparticle

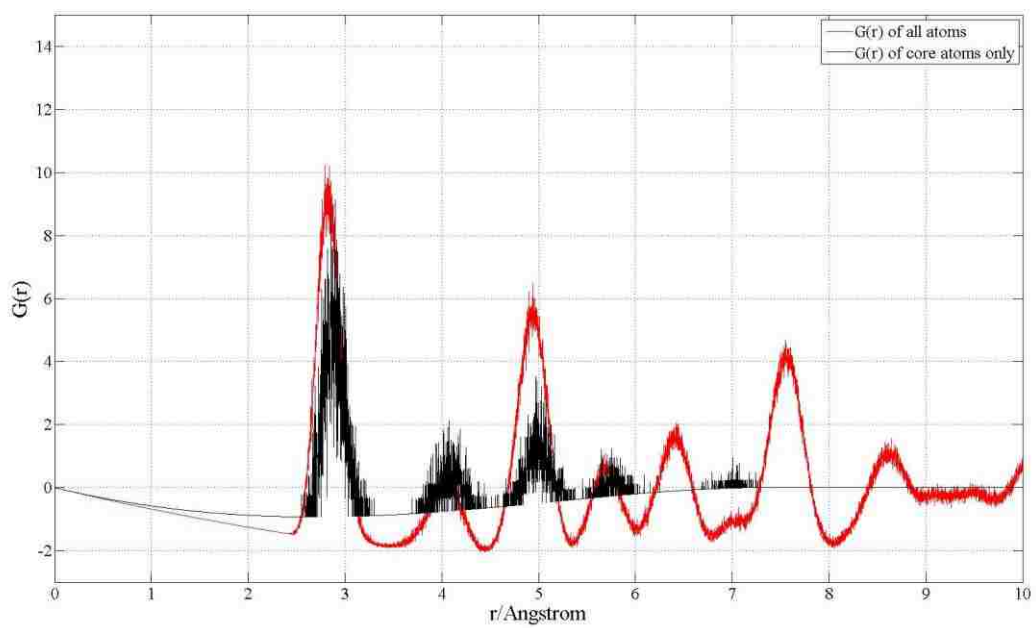


Figure AA.44 Pair Distribution Function of N=321 ($R_{NP}=10.7 \text{ \AA}$) Au Nanoparticle

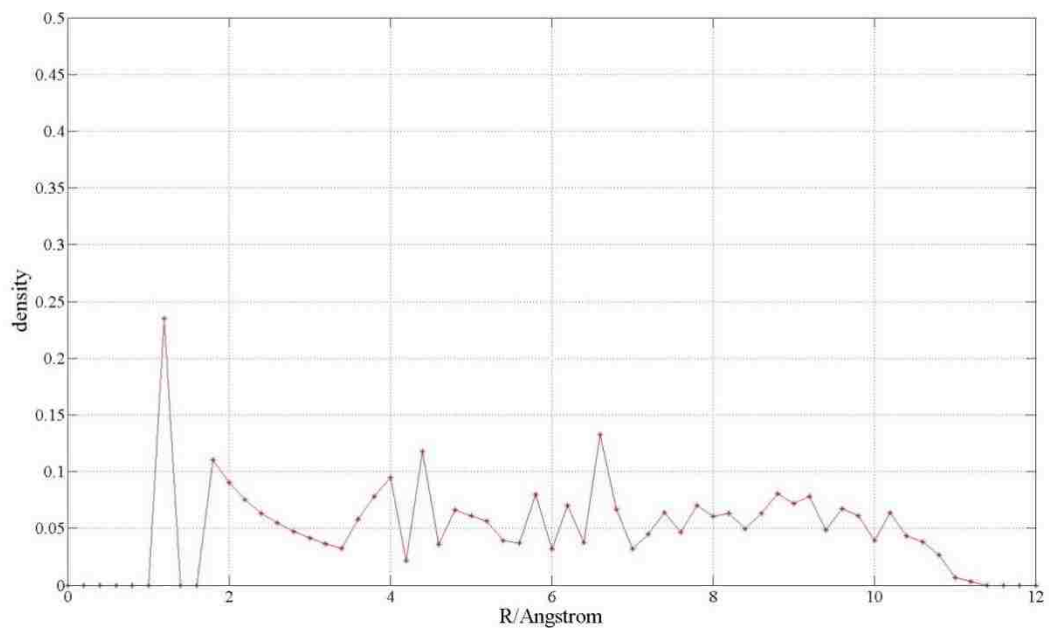


Figure AA.45 Radial Density Profile of $R_{NP}=10.7 \text{ \AA}$ Au Nanoparticle

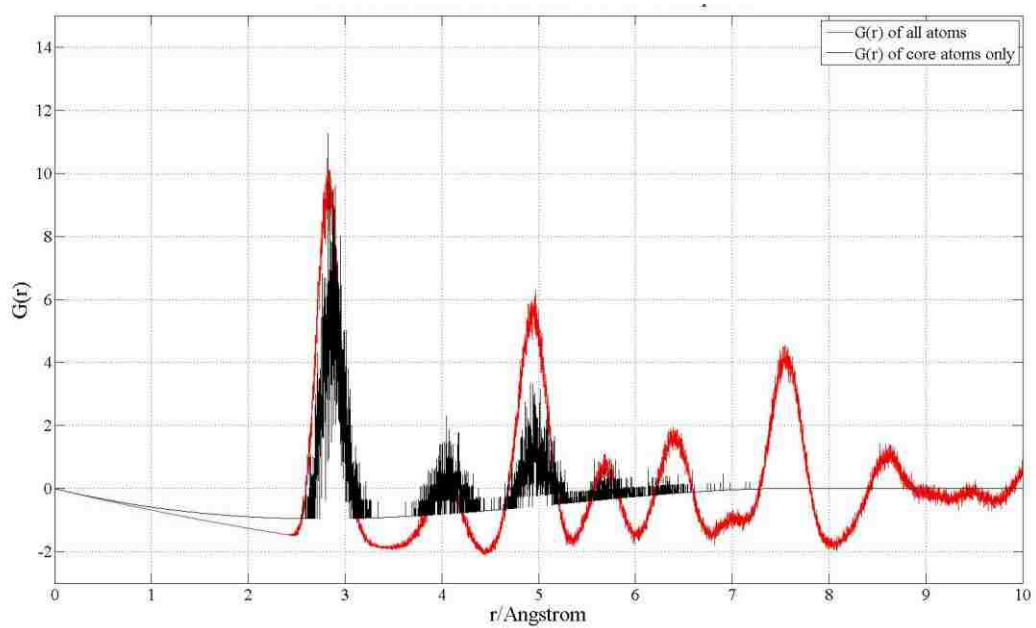


Figure AA.46 Pair Distribution Function of $R_{NP}=10.7 \text{ \AA}$ Au Nanoparticle

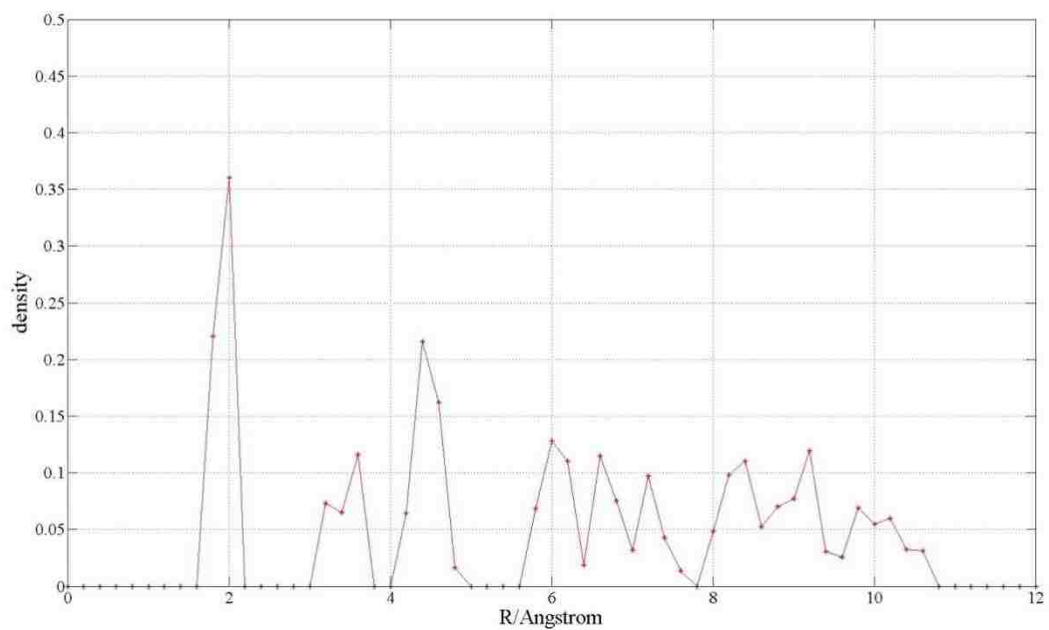


Figure AA.47 Radial Density Profile of N=305 ($R_{NP}=10.6 \text{ \AA}$) Au Nanoparticle

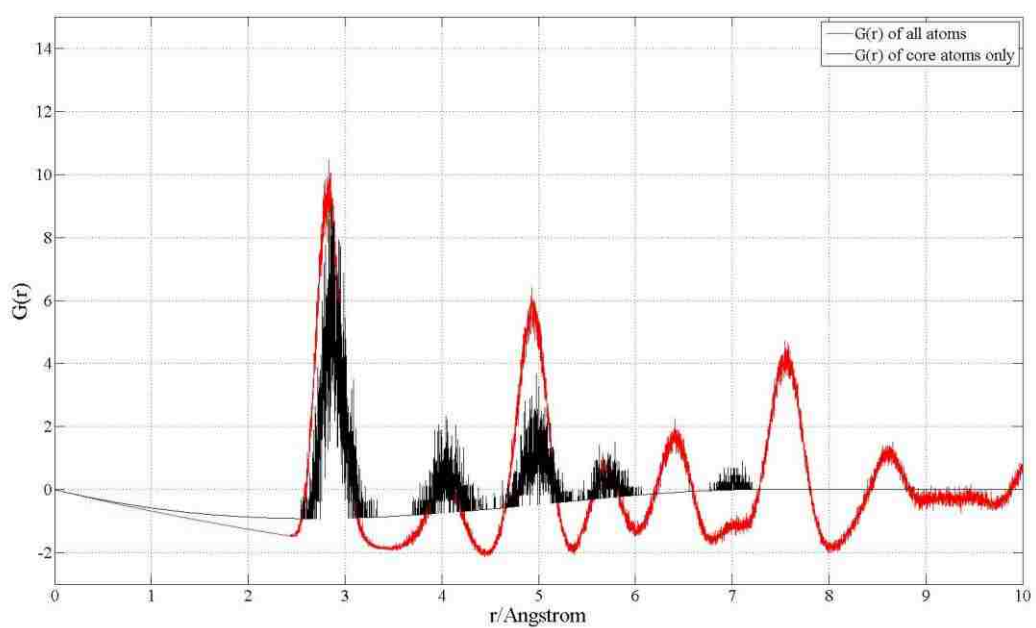


Figure AA.48 Pair Distribution Function of N=305 ($R_{NP}=10.6 \text{ \AA}$) Au Nanoparticle

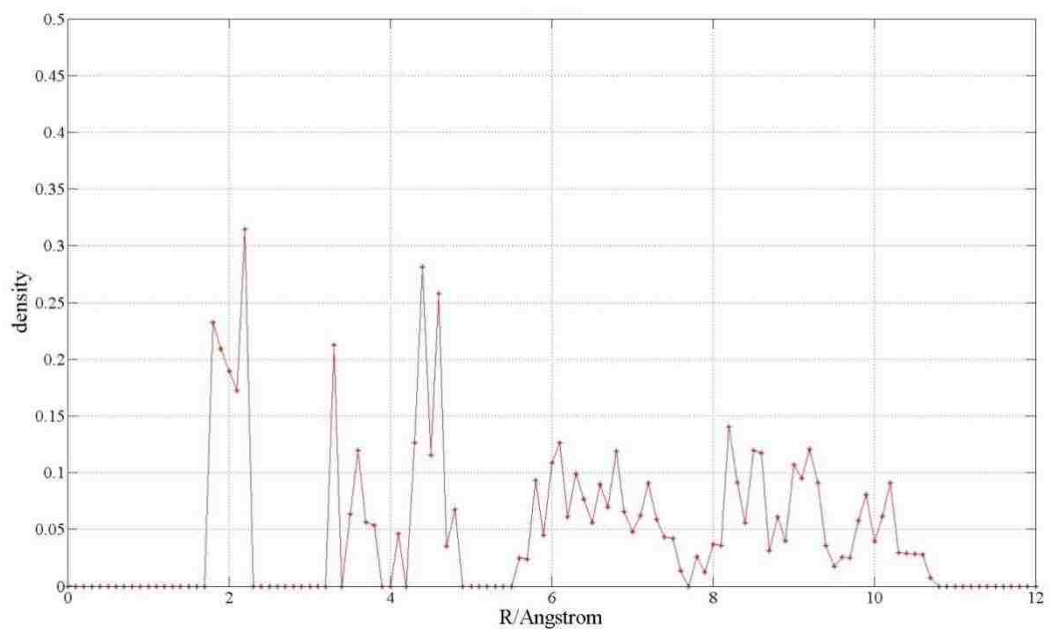


Figure AA.49 Radial Density Profile of N=300 ($R_{NP}=10.4 \text{ \AA}$) Au Nanoparticle

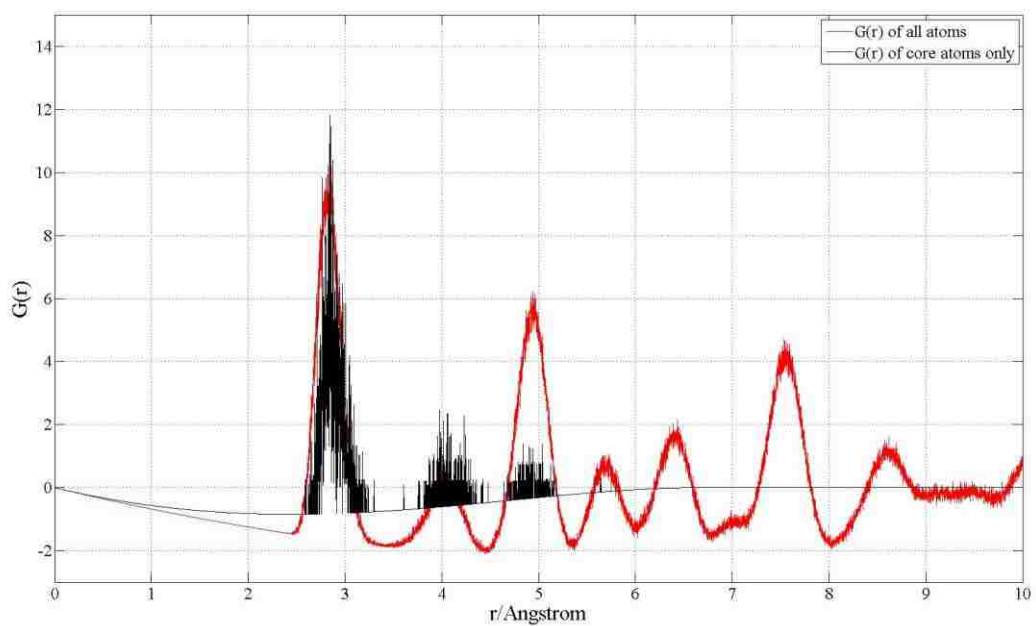


Figure AA.50 Pair Distribution Function of N=300 ($R_{NP}=10.4 \text{ \AA}$) Au Nanoparticle

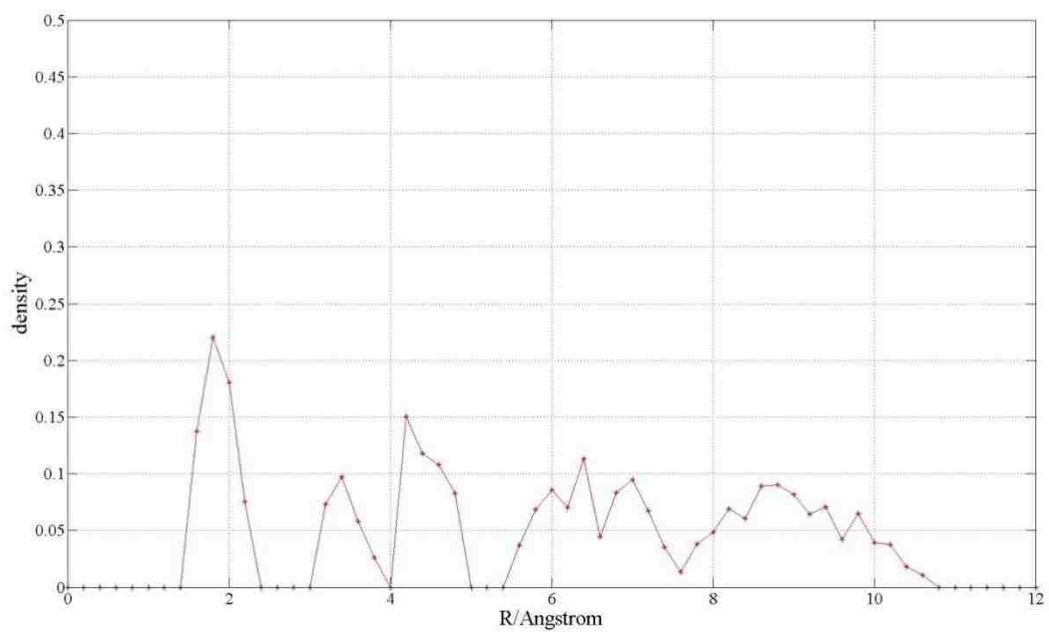


Figure AA.51 Radial Density Profile of $R_{NP}=10.3 \text{ \AA}$ Au Nanoparticle

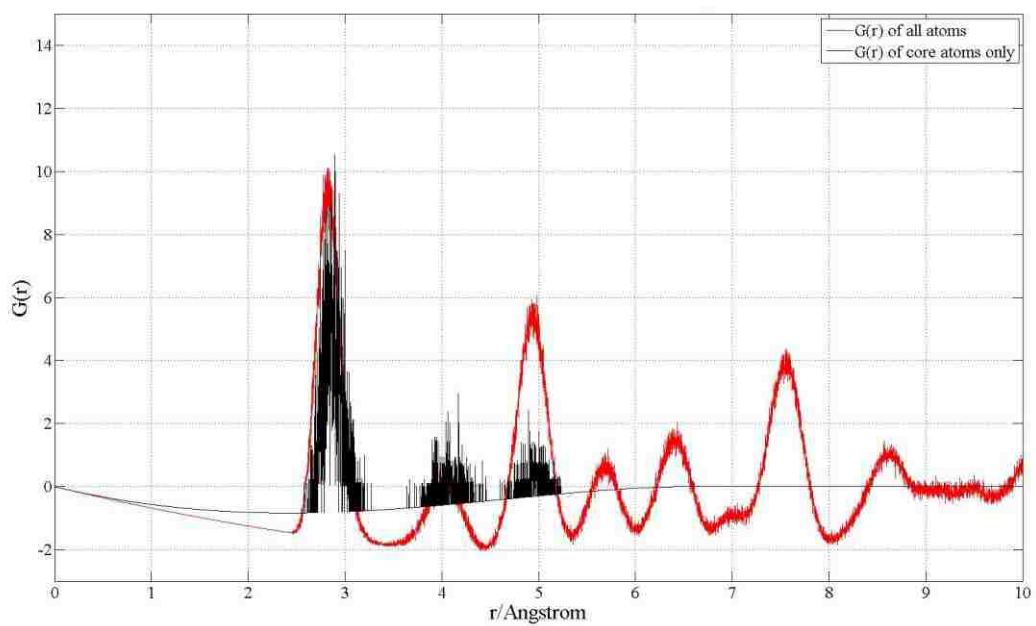


Figure AA.52 Pair Distribution Function of $R_{NP}=10.3 \text{ \AA}$ Au Nanoparticle

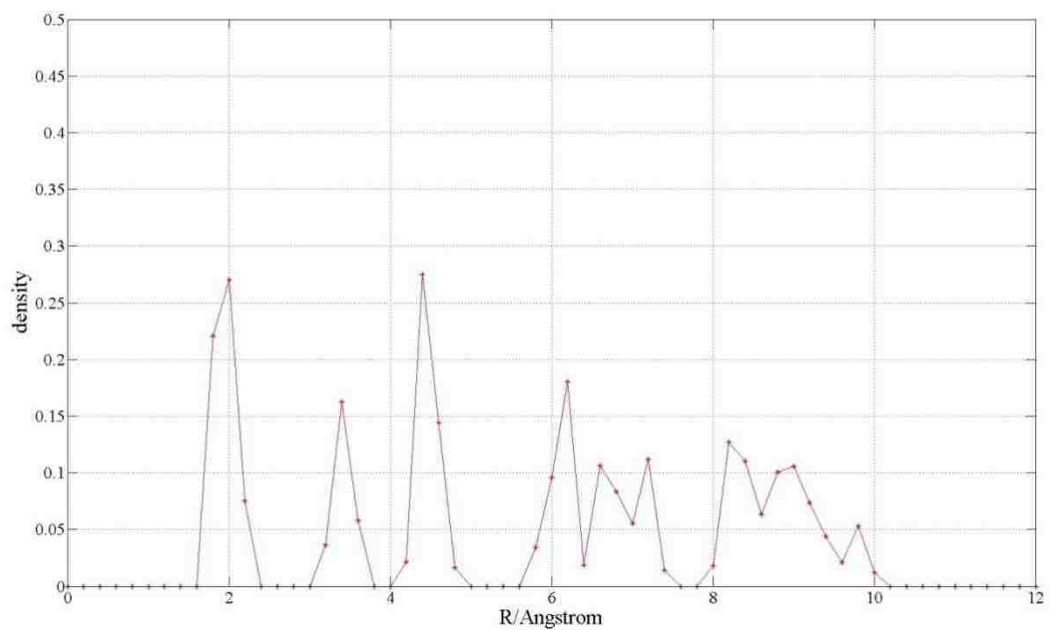


Figure AA.53 Radial Density Profile of $R_{NP}=9.9 \text{ \AA}$ Au Nanoparticle

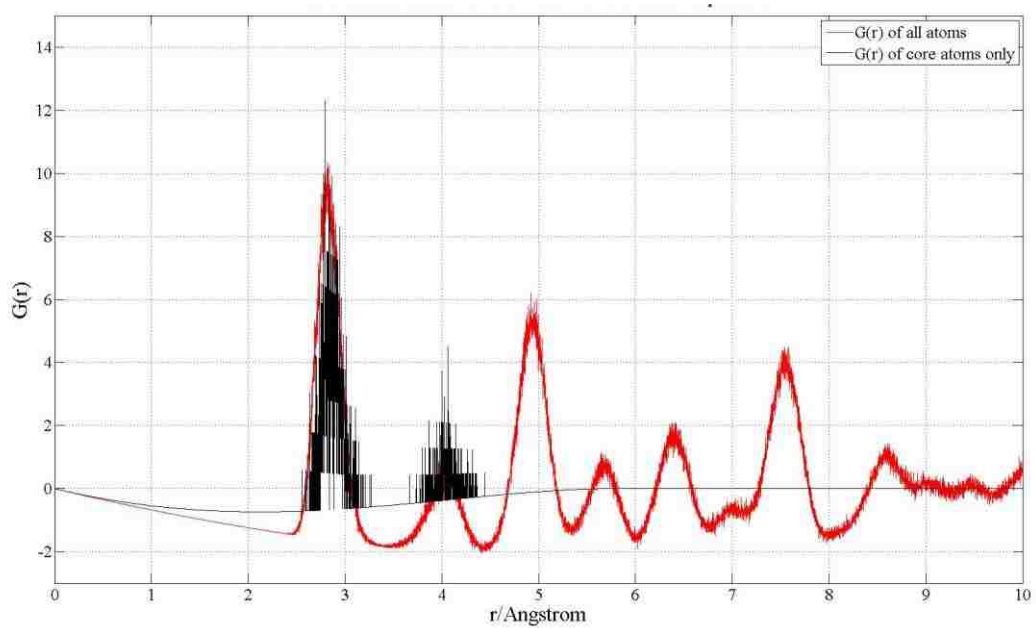


Figure AA.54 Pair Distribution Function of $R_{NP}=9.9 \text{ \AA}$ Au Nanoparticle

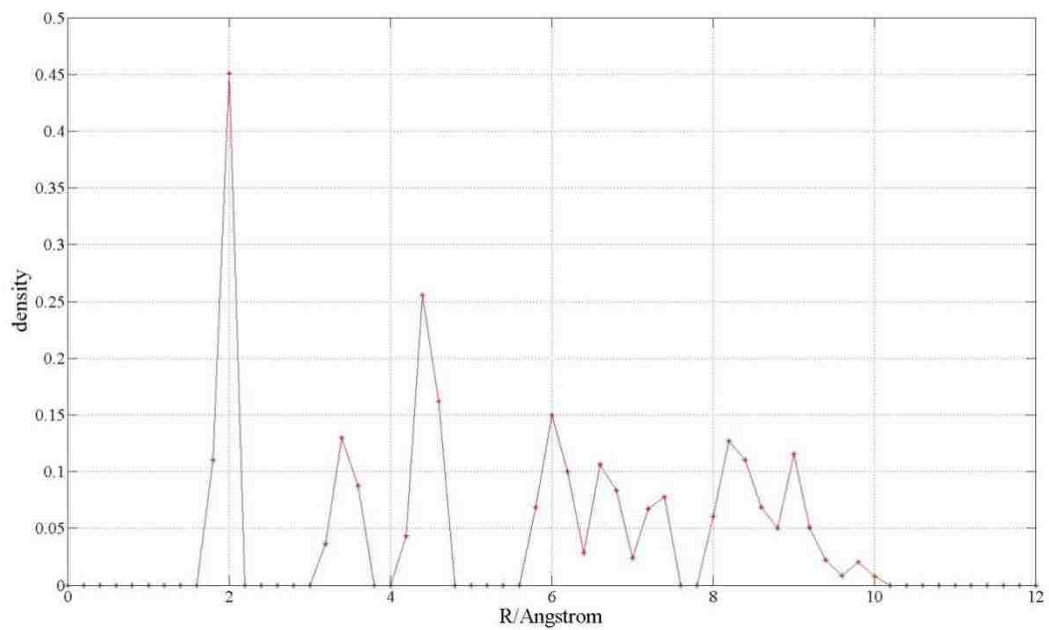


Figure AA.55 Radial Density Profile of $R_{NP}=9.4 \text{ \AA}$ Au Nanoparticle

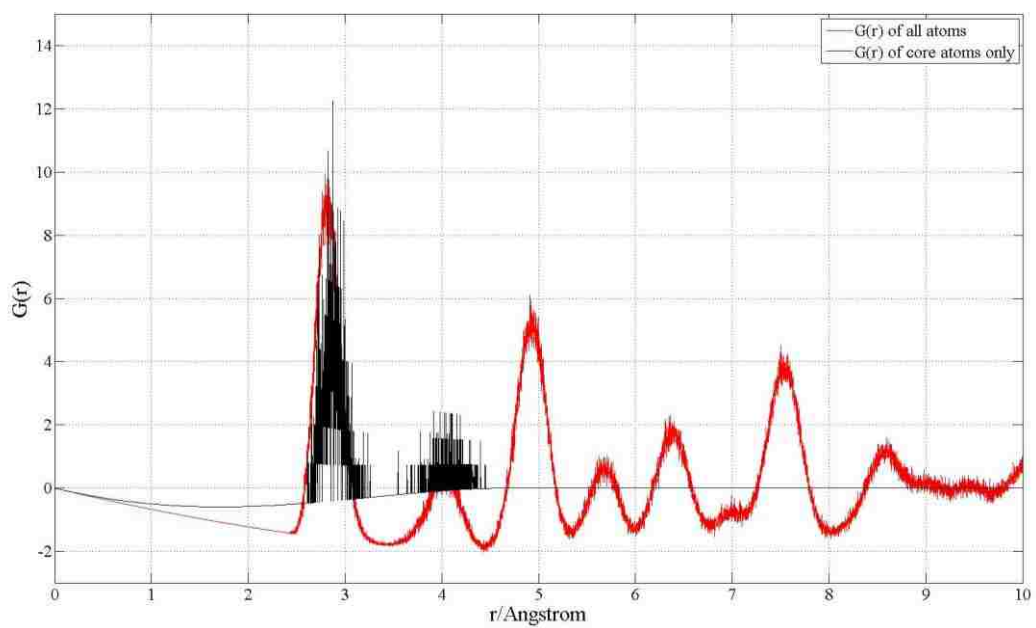


Figure AA.56 Pair Distribution Function of $R_{NP}=9.4 \text{ \AA}$ Au Nanoparticle

Reference

- [1]. R. Nagarajan, T. Alan Hatton, *Nanoparticles: Synthesis, Stabilization, Passvation and Functionalization*, Oxford University Press, Washington, DC, 2008
- [2]. R. Singh et al, *J. AM. CHEM. SOC.* 2005, 127, 4388-4396
- [3]. B. Chertok et al, *Biomaterials.* 2008 February; 29(4): 487–496.
doi:10.1016/j.biomaterials.2007.08.050.
- [4]. F. Baletto and R. Ferrando, *Rev. Mod. Phys.* 77, 371–423, 2005
- [5]. MC Daniel and D. Astruc, *Chem. Rev.* 2004, 104, 293-346
- [6]. B. Corain et al. *Metal Nanoclusters in Catalysis and Materials Science: The Issue of Size Control.* Elsevier, Amsterdam, 2008.
- [7]. R. Jin et al. *Science*, 294:1901, 2001
- [8]. A. P. Alivisatos et al, *Nature*, 382:609, 1996.
- [9]. W. Huang et al, *ACS Nano*, 2008, 2 (5), pp 897–904 DOI: 10.1021/nm800074b
- [10]. K. G. Thomas and P. V. Kamat. *Acc. Chem. Res.*, 36:888, 2003
- [11]. G. Schmid, editor. *Nanoparticles.* Wiley-VCH, Weinheim, 2004.
- [12]. C. L. Cleveland et al, *Phys. Rev. Lett.*, 79:1873, 1997.
- [13]. Turkevitch, J.; Stevenson, P. C.; Hillier, J. *Nucleation and Growth Process in the Synthesis of Colloidal Gold.* *Discuss. Faraday Soc.* 1951, 11, 55-75.
- [14]. H. G. Silva-Pereyra et al, *Journal of Nanoparticle Research*, Volume 12, Number 5, 1787-1795, DOI: 10.1007/s11051-009-9735-6
- [15]. Hiroshi Yao et al, *FORMATEx* 2007

- [16]. N.P. Young et al, Ultramicroscopy Volume 110, Issue 5, April 2010, Pages 506-516
- [17]. Xian-Ning Xie et al, J. Phys. Chem. C2009, 113, 3683-3690
- [18]. Alessandro Longo et al, Journal of Applied Crystallography (2008). 41, 446-455, ISSN 0021-8898
- [19]. Michael McGuigan, arXiv:0912.5316v1 [cond-mat.mes-hall] 29 Dec 2009
- [20]. A.S. Barnard et al, J. Phys. Chem. B, 2005, 109 (51), pp 24465–24472 DOI: 10.1021/jp054279n
- [21]. Dong Hwa Seo et al, J. Phys. Chem. C 2009, 113, 10416–10421
- [22]. Gregory Grochola et al, Journal of Chemical Physics 127, 224704 _2007_
- [23]. K. P. McKenna, J. Chem. Phys. 126, 154704 (2007); doi:10.1063/1.2722751
- [24]. R. Cammarata et al, Annu. Rev. Mater. Sci. 1994 24:215
- [25]. Keith P. McKenna, Physical Chemistry Chemical Physics, 2009, 11, 4145-4151 DOI: 10.1039/B821408P
- [26]. H. Ibach, Surface Science Reports, Volume 29, Issues 5-6, 1997, Pages 195-263
- [27]. R. Plass et al, Nature 412, 875 (30 August 2001) | doi:10.1038/35091143
- [28]. W. Lu et al, PHYSICAL REVIEW B, VOLUME 65, 085401, DOI: 10.1103/PhysRevB.65.085401
- [29]. R. Cammarata, Solid State Physics, Volume 61, 2009, Pages 1-75
- [30]. M.P. Allen, Introduction of Molecular Dynamics in: Computational Soft Matter—From Synthetic Polymers to Proteins, NIC Series, vol. 23, John von Neumann Institute for Computing, 2004, pp. 1–28,

- [31]. G. Sutman, G. Quantum Simulations of Complex Many-Body Systems: From Theory to Algorithms, Grotendorst J., Marx D., A. Muramatzu (Eds.), John von Neumann Institute for Computing, Jülich, NIC Series, vol. 10, 211, 2002.
- [32]. M. P. Allen and D.J. Tildesley. , Computer Simulation of Liquids, Oxford University Press, 1989
- [33]. J.M. Haile, Molecular Dynamics Simulation: Elementary Methods, Wiley & Sons, 1992
- [34]. Cheney et al, Numerical Mathematics & Computing (6th edition), Thomson Learning, 2007
- [35]. S. J. Plimpton, J. Comput. Phys. 117, 1 _1995;
- [36]. M.S. Daw and M.I. Baskes, Physical Review B 29, 6443 (1984)
- [37]. X. W. Zhou, R. A. Johnson, H. N. Wadley, Phys. Rev. B, 69, 144113(2004)
- [38]. Rafael C. Howell et al., Physical Review B 73, 094107, 2006
- [39]. A.S. Masadeh, Physical Review B 76, 115413, 2007
- [40]. R. Meyer et al., Phys. Rev. B 68, 104303 (2003)

Vita

Personal Information

Siming Zhang

Place of Birth: Shenyang, China Date of Birth: January 17th, 1985
Name of Parents: Hong Zhang (Father), Xiaoyun Zhang (Mother)

Education

Lehigh University, Bethlehem, PA

M.S., Computational and Engineering Mechanics September 2011(expected)
GPA: 4.0/4.0

Honored: Fellowship in recognition of the excellent academic accomplishment, Spring 2010

Tsinghua University, Beijing, China

B.E., Engineering Mechanics July 2008
GPA: 3.3/4.0

Publication

11/2008 “The effective Young’s modulus of composites beyond the Voigt estimation due to the Poisson effect”,
Composites Science and Technology, Volume 69, Issue 13, October 2009, Pages 2198-2204, co-author

Research & Professional Experiences

Lehigh University 09/2010-PRESENT

“The effect of surface stress on the internal pressure, lattice constant, and vibrational density of states for gold (Au) nanoparticles”

- ✧ M.S. Thesis (Supervisor: Prof. Edmund B. Webb III)
- ✧ Explored via classical molecular dynamics simulations employing a semi-empirical potential energy function for describing interactions between Au atoms
- ✧ Expected to conduct the work into a publication

Tsinghua University 08/2004-04/2009

“The effective Young’s modulus of composites beyond the Voigt estimation due to the Poisson effect”, co-author

- ✧ Developed the experiment part of this paper independently, including the work as designing the whole experiment scheme, making the specimen, measuring the related parameters and data analysis
- ✧ Completed the finite element computation works during which I built up related models, verified the points of conclusion, and predicted the applicable condition and range of given formulas

Teaching Experience

Lehigh University

Review Session of the course “Fundamentals of Solid Mechanics”,

09/2010-12/2010

- ✧ Conducted review series of classes for my peers taking the same course: covered some topics on tensor analysis, theory of elasticity, and related solid mechanics concepts.
- ✧ Advance my understanding in Solid Mechanics and develop my leadership skills